Phase Field Modeling of Additively Manufactured Ti-Al-V-Fe alloy

PHASE FIELD MODELING OF ADDITIVELY MANUFACTURED TI-AL-V-FE ALLOY

BY

ZHEN LI, M.Sc.

A THESIS

SUBMITTED TO THE DEPARTMENT OF MATERIALS SCIENCE AND ENGINEERING

AND THE SCHOOL OF GRADUATE STUDIES

OF MCMASTER UNIVERSITY

IN PARTIAL FULFILMENT OF THE REQUIREMENTS

FOR THE DEGREE OF

DOCTOR OF PHILOSOPHY

Doctor of Philosophy (2023) McMaster University

(Materials Science and Engineering) Hamilton, Ontario, Canada

TITLE:	Phase Field Modeling of Additively Manufactured Ti-Al-V-Fe alloy
AUTHOR:	Zhen Li M.Sc. (Materials Engineering), Beihang University, China B.Sc. (Materials Science and Engineering), Beihang University, China
SUPERVISOR:	Prof. Andre B. Phillion
NUMBER OF PAGES:	xxvi, 170

Preface

This Ph.D. thesis is an integrated article thesis, also known as sandwich thesis, which has been composed of six main chapters all dealing phase field modeling of a additively manufactured Ti-Al-V-Fe alloy. The thesis is composed of three journal papers and one conference paper:

Chapter 1: Presents a review on Ti-1Al-8V-5Fe alloy, additive manufacturing, and phase field modeling as well as the motivation, objectives, and research plan of this thesis.

Chapter 2: A version of this chapter is published in Computational Materials Science Journal as a research paper: Li, Z., M. Greenwood, and A. B. Phillion. "Fast prediction of phase equilibrium at varying temperatures for use in multi-component phase field models." Computational Materials Science 206 (2022): 111251.

Chapter 3: A version of this chapter is published in Computational Materials Science Journal as a research paper: Li, Z., M. Greenwood, and A. B. Phillion. "A quantitative comparison between pseudo-binary and multi-component phase field models." Computational Materials Science 222 (2023): 112101.

Chapter 4: A version of this chapter is published in IOP Conference Series: Materials Science and Engineering (MCWASP XVI, Banff, Canada): Li, Z., M. Greenwood, and A. Phillion. "A phase field methodology for simulating the microstructure

evolution during laser powder bed fusion in-situ alloying process." IOP Conference Series: Materials Science and Engineering.Vol. 1281. No. 1. IOP Publishing, 2023.

Chapter 5: A version of this chapter is to be submitted to Acta Materialia: Li, Z., M. Greenwood, J. Miranda, and A. Phillion. "Solidification process map of a Ti-Al-V-Fe alloy and its application to a wire arc additive manufacturing process: A phase field study".

Chapter 6: Summarizes the main conclusions of the thesis, outlines the strength and limitations the outcomes, and highlights some future work suggestions. Moreover, it presents the contribution of this research to the literature.

Abstract

Over the past three decades, Additive Manufacturing (AM) has emerged as a widely utilized method for fabricating titanium components, offering notable advantages such as reduced materials waste and enhanced flexibility in geometry design. However, the widespread adoption of AM is hindered by the challenge of ensuring consistent product quality, necessitating a comprehensive understanding of the process-structure-property relationship. Modeling approaches serve as invaluable tools in bridging this gap, providing insights into the AM process while significantly reducing time and experimental costs. Among these modeling techniques, Phase Field (PF) modeling has garnered significant attention as an effective approach for simulating microstructure evolution during AM processing. Within this thesis, I present a comprehensive study utilizing a multi-component phase-field method to investigate the AM process, with a specific focus on Ti-1Al-8V-5Fe (wt%), a cost-effective Beta-Ti alloy. This thesis encompasses the development, verification, applications and validations of the multi-component PF model, advancing our understanding of AM and its application to Beta-Ti alloys.

First, a multi-component phase equilibrium prediction method was developed for use in the multi-component phase field models. The prediction of phase equilibrium is

a main time-consuming section of a multi-component PF model. To improve the computational efficiency, a new convex-based method for temperature dependent phase equilibrium prediction was proposed in this study. To show the accuracy of the convex hull method, 1-D phase field simulations utilizing the Convex-hull method were performed under isothermal and continuous cooling conditions. The 1-D simulation results were compared against Thermo-Calc calculations, which shows that a high accuracy of equilibrium prediction is achieved at a single and multiple temperatures.

Second, the implementation of the multi-component PF model was further verified via performing a benchmark analysis on different 2-dimensional models of solidification in multi-component alloys. Specifically, the multi-component PF model and two pseudo-binary PF models were applied on the isothermal and directional solidification of the Ti-185 alloys. The results showed that a very good similarity in microstructure was achieved between the three phase field models during both isothermal and directional solidification. The results demonstrate the usefulness of different PF modelling approaches and highlight cases where a full multi-component model is needed.

Third, the multi-component PF model was applied on the Laser Powder Bed Fusion (LPBF) process. In this study, two large-scale PF simulations were performed to simulate the microstructure evolution during LPBF process using pre-alloyed powder and blended elemental powder. This work aims to provide a clear picture of the in situ alloying process and improve our fundamental understanding of the competitive growth phenomenon. The results show that evenly distributed finer columnar grains formed while using pre-alloyed powder. For the case of using elemental powders, the results indicate that full alloying is difficult to achieve during the LPBF printing process; this incomplete alloying greatly influences the dendrite morphology and solute

distribution.

Finally, the multi-component PF model was applied to the Wire Arc Additive Manufacturing (WAAM) process and to construct the solidification process map of the Ti-185 alloy. The solidification process map was compared with experimental results for the model validation. The process map of the Ti-185 alloy was constructed via performing a series of simulations with constant temperature gradient and solidification rate. The process map shows that a CET transition occurs at the top of the sample, this trend shows an excellent agreement with experimentally characterization.

Keywords: Phase field model, Additive manufacturing, Beta-Ti alloy, Solidification, Multi-component phase equilibrium, Solidification process map, In situ alloying,Laser powder bed fusion, Wire arc additive manufacturing

To my beloved parents

Acknowledgements

I would like to express my heartfelt gratitude to my supervisor, Dr. Andre Phillion, for his unwavering support, invaluable guidance, and immense patience throughout the course of this research. His extensive knowledge in the field of solidification and insightful foresight have been instrumental in shaping the foundation of this thesis. I am also deeply grateful to my co-supervisor, Dr. Michael Greenwood, for his invaluable guidance and support. His step-by-step assistance in delving into the intricacies of phase field modeling and his unwavering commitment to helping me overcome various challenges during my Ph.D. journey have been immensely valuable. I extend my sincere thanks to Dr. Oleg Rubel for serving as a member of my annual committee meetings and providing me with invaluable suggestions and feedback throughout my Ph.D. studies. Your expertise and constructive input have been highly appreciated.

I would also like to express my heartfelt appreciation to my parents, my older sisters, and my partner for their unconditional love, unwavering support, and understanding throughout this journey. Their presence, encouragement, and belief in my abilities have been a constant source of motivation and inspiration.

I am truly grateful to all individuals who have contributed to my academic and personal growth, directly or indirectly. Your support has been invaluable, and I am privileged to have had the opportunity to work alongside such remarkable individuals.

Contents

Preface iii

Abstract v

Acknowledgements ix

List of Figures xv

List of Tables xx

Notation, Definitions, and Abbreviations xxii

1 Introduction 1

1.1 Background 1

1.1.1 Ti-1Al-8V-5Fe alloy 1

1.1.2 Additive Manufacturing 3

1.1.3 Phase field modeling 6

1.2 Motivation 11

1.3 Research Objectives 12

1.4 Thesis Outline 13

References 15

2 Fast prediction of phase equilibrium at varying temperatures for use in multi-component phase field models 21

2.1 Introduction 23

2.2 Governing equations for the multi-component PF model 28

2.3 Prediction of Phase equilibrium in multi-component alloy systems . . 31

2.3.1 Comparison of phase equilibrium prediction between binary and multi-component alloy systems 31

2.3.2 Predicting phase equilibrium at one temperature 33

2.3.3 Predicting phase equilibrium at multiple temperatures 35

2.3.4 Process flow for coupling the Phase Equilibrium Calculator with PF Simulations 37

2.4 Results and Discussion 38

2.4.1 CHT calculator verification 39

2.4.1.1 Prediction accuracy at a single temperature 39

2.4.1.2 Prediction accuracy at multiple temperatures 41

2.4.2 Use of the CHT calculator within a PF model 42

2.4.2.1 Isothermal 1-D PF simulation 43

2.4.2.2 Continuous Cooling 1-D PF simulation 45

2.5 Conclusions 52

References 53

3 A Quantitative Comparison between Pseudo-Binary and Multi-Component Phase Field Models 57

3.1 Introduction 59
3.2 Description of the Phase Field models 63
3.2.1 Pseudo-Binary Phase Field Model 1 63
3.2.2 Pseudo-Binary Phase-Field Model 2 and Multi-Component Model 65
3.3 Numerical Implementation 70
3.4 Results and Discussions 73
3.4.1 Isothermal solidification of a multi-component alloy 74
3.4.2 Directional solidification of a multi-component alloy 81
3.4.2.1 Comparison between the three models under the same thermal conditions 81
3.4.2.2 Influence of thermal conditions on microstructure . . 86
3.5 Conclusion 90
References 91

4 A phase field methodology for simulating the microstructure evolution during laser powder bed fusion in-situ alloying process 96

4.1 Introduction 99
4.2 Numerical Methods 103
4.2.1 Phase Field Simulations 103
4.2.2 Finite Element Thermal Analysis 107
4.2.3 Numerical Implementation of the PF, FEA, and Nucleation Modules 108
4.3 Results and discussions 111
4.3.1 Finite Element Analysis 111
4.3.2 Initial condition for the Phase field models 111

4.3.3 Phase field simulation during LPBF using pre-alloyed powders 113
4.3.4 Phase field simulation during LPBF using elemental powders . 115
4.4 Conclusions 117
4.5 Acknowledgement 118
References 118

5 Solidification process map of a Ti-Al-V-Fe alloy and its application to a wire arc additive manufacturing process: A phase field study 123
5.1 Introduction 126
5.2 Methods 130
5.2.1 Phase Field Simulations 130
5.2.2 Thermal FEA Simulations 134
5.2.3 Numerical Implementation 136
5.2.3.1 Phase Field Simulations 136
5.2.3.2 Thermal FEA Simulations 137
5.3 Experimental Methods 140
5.4 Results and discussions 140
5.4.1 Phase Field Simulations and Creation of the Solidification Process Map 140
5.4.2 Thermal FEA Simulations 144
5.4.3 Assessing the Influence of WAAM process parameters on the Columnar to Equiaxed Transition 145
5.4.4 Model Validation 150
5.5 Conclusions 152
5.6 Acknowledgement 155

References 157

6 Conclusions and Summary **162**

6.1 Summary and Conclusive remarks 162

6.2 Limitations and future work 166

6.3 Contribution 167

References 170

List of Figures

2.1 Free energy curve for (a) a binary alloy and (b) a ternary alloy at constant pressure and temperature in the two phase region. The common tangent line and plane are indicated to identify the equilibrium $\vec{\mu}_{eq}$, $\vec{c}^{L}_{eq}$, and $\vec{c}^{S}_{eq}$. 33

2.2 Flow chart of phase equilibrium data calculation and transferring process between a CALPHAD database, the CHT calculator and the PF model. 38

2.3 Mean relative error in the equilibrium solute concentrations for Al, V, and Fe predicted by the CHT calculator as compared to TC calculations as a function of temperature in the (a) liquid and (b) solid phases. 42

2.4 Snapshot at $f_s = 0.81$ of the Isothermal PF simulation results for the Ti-185 at 1750 K; (a) Order parameter profile and (b) Normalized Concentration Profile. 43

2.5 (a)Comparison in Ti-185 equilibrium solute concentrations between the PF simulation, the CHT calculator, and the TC single equilibrium calculation, (b)absolute deviation and relative error between the CHT calculator and the TC single equilibrium calculation, and (c) variation of average c^S_{Fe} as a function of simulation time in the PF simulation . 44

2.6 Snapshot at 1710 K of the continuous cooling PF simulation results for the Ti-185 at a cooling rate of 100 K/s; (a) Order parameter profile and (b) Normalized Concentration Profile. 46

2.7 Evolution of solute in solid side of solid/liquid interface for (a) Al, (b) V and (c) Fe 47

2.8 Variation of equilibrium solute concentration as a function of temperature for (a) Al, (b) V and (c) Fe predicted by Thermo-calc single equilibrium calculation, the phase equilibrium calculator and the phase field model 50

2.9 Variation of relative deviation between CHT calculator and Thermo-calc, and relative deviation between PF model and Thermo-Calc as a function of temperature for (a) Al, (b) V and (c) Fe 51

3.1 A comparison of grain morphology of isothermal solidification of Ti-185 alloy at $T = 1805$ K from three different phase field models at the same time $t = 0.15$ ms. Where, MC means Multi-component model, BM I represents a pseudo-binary model based on the model by Karma et al, BM II is the binary model based on the model by Provatas et al 75

3.2 Variation of tip traveling distance with time from three phase field models for the isothermal solidification of Ti-185 alloy 76

3.3 Distribution of solute components (b) Al, (c) V and (d) Fe across the solid/liquid interface along lines L1 and L2 indicated in (a), during isothermal solidification of Ti185 alloy at 1805 K, where *position* = 0 is the solid/liquid interface 79
3.4 The ratio of computational CPU time between the multi-component model and the pseudo-binary models as a function of iterations . . . 80
3.5 A comparison of concentration profiles of Fe during directional solidification of Ti-185 alloy from (a) BM I, (b) BM II and (c) MC, at the same time t =1.56 ms 82
3.6 Variations of dendritic tip velocity as a function of time from three PF models 83
3.7 A comparison of solid fraction simulated by the three PF models and Scheil simulation as a function of height, or temperature (Considering the fixed temperature gradient in height direction) 85
3.8 Columnar grain structure simulated from the BM I for pulling velocity is (a) 25 mm/s, (b) 50 mm/s,(c) 75 mm/s and (d) 100 mm/s (Same temperature profile) 86
3.9 Variation of dendrite tip temperature at steady state with pulling velocity 88
3.10 Variation of Secondary Dendrite Arming Spacing with cooling rate from the three PF models 89

4.1 Flowchart showing the numerical implementation of the PF, FEA, and Nucleation Modules to simulate the LPBF process. 109
4.2 Contour plot and XoY and XoZ views of the temperature profile and molten pool geometry from the heat transfer finite element analysis . 111

4.3 The initial condition for the phase field simulations, including (a) a snapshot of the temperature profile and domain geometries, (b) the uniform concentration map with initial microstructure, and (c) the spatially varying concentration map with a background of Ti-185. . . 112
4.4 A snapshot at t = 0.65 ms of the concentration profile of Al, V and Fe during using pre-alloyed powder in laser powder bed fusion process . 114
4.5 A snapshot at t = 0.45 ms of the concentration profile of Al, V and Fe during LPBF using pre-alloyed powders. 116

5.1 Mesh and boundary conditions for the thermal FEA simulation of the WAAM process. Please note that the convection and radiation boundary conditions are defined for all the four side surfaces of the printed layers, and the zero flux boundary conditions are defined for all the four side surfaces of the substrate 139
5.2 Solute distribution of (a) Al and (b) Fe, and the resulting grain morphology as predicted by the PF model for Case 1. 141
5.3 Solute distribution of (a) Al and (b) Fe, and the resulting grain morphology as predicted by the PF model for Case 16. 142
5.4 Solidification process map for the 19 PF simulation results, showing the Columnar to Equiaxed Transition. Hunt's analytical model for the CET is also plotted for a Ni-based superalloy [7, 8] 144
5.5 A snapshot of the temperature distribution when printing the 10^{th} layer of the thin wall during WAAM process 146

5.6 Simulated thermal history of all ten layers during deposition and cooling of Layer 10 of the Ti-185 thin wall. Figures (a,b) shows an over-all view and mushy zone inset view, respectively. The data for these curves was taken from the front of the built, as shown by the red dots in Fig. 5.1. 146

5.7 Solidification process map to show PF simulation results, and the position of the WAAM thermal conditions in the solidification process map 149

5.8 LHS: A cross-section view of the temperature distribution predicted by the thermal FEA model when printing Layer 10. RHS: A low-resolution side-view micrograph of the experimentally-built, via WAAM, thin wall sample 153

5.9 (a) A low-resolution micrograph shring the overall grain structure of the WAAM fabricated Ti-185 sample, (b,c) higher-resolution micrographs showing the top and bottom zones within the melt pool. Please note that the arc travel direction is into the page 154

List of Tables

2.1 Simulation parameters and thermo-physical properties of Ti-185 alloy [6][24] 38

2.2 Comparison of relative error ($|c_{\mathrm{CHT}} - c_{\mathrm{TC}}|/c_{\mathrm{TC}}$ [%]) between the CHT calculator and TC single element calculation in predicting the Ti-185 equilibrium solute concentrations in the solid and liquid phases at 1750 K for the five solute concentration ranges given in Table 2.3. 40

2.3 Solute concentration ranges (wt.%) used to extract free energy from TC TCTI2 database at 1750 K for the Ti-185 alloy 41

3.1 Simulation parameters and thermo-physical properties of Ti-185 alloy [7][13] 73

4.1 Simulation parameters used in the phase field simulations [8][10] . . . 110

4.2 Process parameters of LPBF-Ti185 alloy used in the finite element analysis [3] 110

5.1 Simulation parameters used in the PF simulations [25][26] 137

5.2 G, V, and the corresponding interface witdh W_0 for each of the nineteen simulations used to generate the solidification process map 137

5.3 Process parameters of WAAM-Ti185 alloy used in the finite element analysis 140
5.4 Thermal conditions and CET transition in different WAAM process . 150

Notation, Definitions, and Abbreviations

Abbreviations

AMR	Adaptive Mesh Refinement
AM	Additive Manufacturing
BM I	Karma's binary-alloy PF model
BM II	Provatas' binary-alloy PF model
CET	Columnar to Equiaxed Transition
CHT	Convex Hull with Temperature (CHT) calculator
CA	Cellular Automata
CALPHAD	CALculation of PHAse Diagrams
CAD	Computer Aided Design
FEA	Finite Element Analysis

FE-PF	integrated Finite Element Phase Field model
LPBF	Laser Powder Bed Fusion
MC	Multi Component model
WAAM	Wire Arc Additive Manufacturing
DED	Direct Energy Deposition
OM	Optical Microscope
PDAS	Primary Dendrite Arm Spacing
PDEs	Partial Differential equations
PF	Phase Field
PSP	Process-Structure-Property
SDAS	Secondary Dendrite Arm Spacing
SEM	Scanning Electron Microscope
SLM	Selective Laser Melting
SPM	Solidification Process Map
Ti-185	Ti-1wt.%Al-8wt.%V-5wt.%Fe
TC	Thermo-Calc

Notation

ϕ	Order parameter
V	Growth velocity
V_n	Interface velocity
T	Temperature
T_L	Liquidus
T_S	Solidus
T_0	Initial temperature
V_P, v_p	Solidification rate
G	Thermal gradient
d_0	chemical capillary length
κ	Interface curvature
C_0	Alloy Composition
β	kinetic coefficient
T_m	Melting point of pure metal
m_l	Liquidus slope
m_s	Solidus slope
F_θ	Helmholtz free energy of one phase θ

A_{ij}^{θ}, $\bar{c}_i^{\theta}$, B_j^{θ} **and** D^{θ}	Fitting parameters
k	Partition coefficient
I	the Identity Matrix
$f'_{DW}(\phi)$	Double well potential function
μ	chemical potential
W	Interface width
f_s	solid fraction
τ	Relaxation time
θ	Angle between interface normal and pulling velocity
P_n	Nucleation probability
μ_N	Nucleation possibility parameter
θ_0	Misorientation angle
$\vec{\mu}$	a vector constituting of μ_i
$\vec{n}$	Normal direction to the interface
$a_s(\vec{n})$	2D four-fold anisotropy
ϵ_4	Anisotropy strength
$\hat{\lambda}$	Dimensionless coupling coefficient

σ_{SL}	Solid-liquid interface energy
a_0	Interatomic spacing
D	Solute diffusion coefficient
μ_{eq}	Equilibrium Chemical potential
$\vec{\mu}_{eq}$	a vector constituting of μ_{eq}
$c^{\theta}_{eq,i}$	Equilibrium concentration of the ith solute in phase θ
$\vec{c}^{\theta}_{eq}$	a vector constituting of $c^{\theta}_{eq,i}$
Γ	Gibbs-Thomson coefficient
ΔT_f	Freezing range
ΔT	Local undercooling
ΔT_n	Nucleation undercooling for equiaxed grains
λ	Absorpitivity
P	Power of the heat source
r_0	Radius of the heat source
σ	Stefan-Boltzmann constant
ϵ	Emissivity
h	Heat convection coefficient

Chapter 1

Introduction

1.1 Background

1.1.1 Ti-1Al-8V-5Fe alloy

Titanium alloys are critical materials for the aerospace industry. To achieve the goals of reducing energy consumption and carbon dioxide emission in the aircraft industry, it is necessary to reduce aircraft weight by using materials that offer structural weight savings. Ti alloys are a good choice in this regard because of their superior specific strength compared to other structural alloys [1, 2]. To give an example, replacing conventional steel with Ti alloys can achieve a 64% reduction in weight [2]–however at significantly increased cost. Ti alloys also present good corrosion resistance up to 500 °C. So, they can largely improve aircraft performance because of their excellent combination of high specific strength and good corrosion performance [1, 2, 3]. Because of these advantages, the mass fraction of Ti alloys in airplanes has increased significantly in recent years; the Boeing 787 contains 20% by weight of Ti alloys in

parts like landing gear and nacelle brackets [1].

The Ti element shows an allotropic phase transformation whereby the Hexagonal Closed Packed (HCP) α phase at room temperature will completely transform to Body Centered Cubic (BCC) β phase when it is heated over 882 °C. Most titanium alloys are composed of both the α phase and the β phase [4]. Further, solute alloying elements in the Ti-alloys are classified as α stabilizers, β stabilizers and neutral elements according to their ability to enlarge the corresponding phase region [4]. Based on the combination of phases and alloying elements, Ti alloys are classified as: α, $\alpha + \beta$, and β. The α alloys contain mainly α stabilizers and neutral elements which serve as solid solution strengtheners. In these alloys, the β stabilizers are absent or only present in a small amount usually less than 1%. α alloys have excellent formability, low modulus of elasticity, and good weldability, and thus are widely used in applications ranging from aircraft frames and engine components, to biomedical implants [3]. The $\alpha + \beta$ alloys contain both α and β stabilizers, with the amount of β stabilizers being about 4% to 6%. These alloys offer a good combination of high strength, toughness, and ductility, which makes them suitable for aircraft structural components such as airframes, wings, and landing gear [3]. Finally, the β alloys contain mainly β stabilizing elements, over 10 wt%, to help retain the β phase upon quenching. β-Ti alloys present highly attractive mechanical properties: high mechanical strength (over 1400 MPa), acceptable toughness, good formability, and deep hardenability [3, 5, 6, 7].

Although β-Ti alloys present these excellent mechanical properties, their usage remains a small segment in the titanium industry [3, 5]. The main reason for their limited application is very high cost, which partly comes from conventional expensive

β stabilizers Mo, Cr and V [7]. Another source of the high cost is its high buy-to-fly ratio, which means that a large proportion of material is lost in the manufacturing process (mostly machining). Some β alloys, such as Ti-15V-3Cr-3Al-3Sn, exhibit nearly no work hardening and thus the machining costs are even higher [5].

Ti-1Al-8V-5Fe (wt%) is a β Ti-alloy that has gained attention in the aerospace industry recently for its potential to reduce aircraft weight and lower cost. Using Fe as a β stabilizer greatly reduces the cost of the Ti-185 alloy when compared with other common commercial β titanium alloys, such as Ti-10V-2Fe-3Al(Ti-1023) and Ti-5Al-5V-5Mo-3Cr (Ti-5553) [7]. However, the application of Ti-185 is limited by the strong micro-segregation of Fe and subsequent precipitation of brittle phases during casting [7]. To overcome these shortcomings, additive manufacturing was proposed to fabricate Ti-185 components [7, 8].

1.1.2 Additive Manufacturing

Additive Manufacturing (AM), also known as 3D printing, is an innovative manufacturing approach that enables the fabrication of components layer by layer using digital models [1, 2, 9, 10, 11]. One of the main advantages of the AM technique is its ability to produce highly complex geometries with a high degree of precision, using automated systems and computer-aided design (CAD) models [9, 12].

AM has gained significant attention since 1990s due to its potential to reduce lead times, lower material waste, and improve customization [1, 2, 9]. Currently, some aerospace companies have begun to use additively manufactured parts in their commercial aircraft. Boeing, Inc. uses 32 different AM-fabricated components in its 787 Dreamliner planes [2]. General Electric also reports that 50% of parts in their

aircraft engines and energy turbines will made by AM within 10 years [2]. Powder Bed Fusion (PBF) and Direct Energy Deposition (DED) are the two most common approaches for Metal additive manufacturing.

PBF is the most used AM technique for the fabrication of metal components, occupying 54% of the whole industrial Metal AM market [13]. The PBF process entails the creation of a three-dimensional computer-aided design (CAD) model of the component, which is subsequently sliced into multiple layers. A layer of metal powder, of uniform thickness, is evenly distributed over the substrate to serve as the powder bed, upon which a high-energy heat source scans over the powders along a pre-defined route. In a localized melting and solidification process, the powder particles are fused together to form the desired solid slices in this layer. After the completion of the first layer, the build plate is lowered, and a new layer of powder is spread over the previous layer. The heat source then scans over the new layer, melting and solidifying the powder particles to create the second layer. This layering and melting process is repeated until the desired component is fully formed, with its precise shape and dimensions as dictated by the original CAD model. [2, 10]. Generally, pre-alloyed powders are used in the PBF process, but when researching new alloys it becomes complicate and costly to fabricate alloys with no commercially available powder stock, such as Ti-185 [7, 8]. The emerging blended elemental powders, which uses pure elemental powders as a substitute for prealloyed powders, makes it possible to fabricate AM components with arbitrary alloy systems [7, 8]. PBF is a highly precise technique for producing complex geometries with high accuracy and resolution, while the disadvantages are high cost and lower efficiency [3].

DED is a complementary technique to PBF that enables AM of large metallic

components [3, 14, 15]. During the DED process, a wire or powder feeder is used to continuously feed the materials, which are then directly melted by a high energy heat source (plasma arcs, laser, and electron beam) and then deposited on a substrate or previous deposited layers. Additionally, DED can be used to repair or add materials to existing parts, making it a valuable technique for maintenance applications [14]. Wire and arc additive Manufacturing (WAAM) is one of the most effective and valuable DED techniques. This processes uses electric arc as the heat source, enabling a high deposition rate, short production lead time and high material utilization [3]. Although DED has some strong benefits, the process typically results in lower resolution and accuracy as compared to PBF, and the parts may require post-processing to achieve the desired surface finish and mechanical properties [14].

The AM process is characterized by unique thermal conditions, which presents both opportunities and challenges. During the AM process, a fast-moving high energy density heat source is used, resulting in high solidification rates and temperature gradients along the building direction [9, 16]. On one hand, such rapid solidification conditions enable the fabrication of alloys that cannot be made by casting, such as Ti-185 alloy [7, 8]. On the other hand, they also give rise to challenges such as the formation of coarse columnar grains with strong [001] texture, leading to high microsegregation and anisotropic mechanical properties [15, 16]. So, morphological control and including the Columnar to Equiaxed Transition (CET) are main subject areas of the AM research.

Furthermore, the Process-Structure-Property (PSP) relationship in AM is difficult to establish. Given the variation in materials feeding approach and energy source, as well as differences in scanning route design and process parameters, which result in

large changes in the melt pool geometry and thermal history, the microstructure and properties of final parts will be influenced and differing [9]. For example, melt pool size alone can change from hundreds of micrometers in PBF to several millimeters in DED, while the the cooling rate can changes from 10^5 K/s in PBF to 10^3 K/s in DED [9]. The using of blended elemental powders, which results an in-homogeneous concentration distribution [7, 8], makes it even more complicated to build a PSP relationship. However, the large-scale commercial application of additive manufacturing technology requires good control of product quality, and the PSP relationship is a key point [9, 10]. So, an urgent task is to establish a comprehensive understanding of the impact of different AM parameters on the microstructure and mechanical properties of materials.

While numerous experimental study has been made to study PSP linkage in AM processes, experimental approaches and the related conventional trial-and-error cycle can be costly. The development of modeling techniques provide another options to develop PSP relationships. The Phase Field model is one of the most popular method to study the microstructure evolution during AM processing.

1.1.3 Phase field modeling

Phase Field (PF) modeling is a powerful computational method for simulating and analyzing the evolution of microstructures in materials [17, 18, 19]. It is based on the concept of a phase field, which is a continuous variable that describes the order parameter of a material. The phase field can be used to represent different domains within a material, such as solid, liquid, gas, or different crystallographic orientations.

The basic idea behind PF modeling is to represent the microstructure of a material

as a continuous field that varies smoothly over space and time. The evolution of the microstructure can then be described by the dynamics of the phase field, which is governed by a set of partial differential equations (PDEs) derived from the free energy of the system [17, 20, 21]. The PDEs describe the local changes in the phase field due to thermodynamic driving forces, as well as diffusion, surface energy, and interfacial tension. PF modeling has several advantages over other computational methods for simulating microstructure. One of the key advantages is its ability to capture the complex and dynamic behavior of interfaces and boundaries between different phases. This is particularly important for studying phase transformations, such as solidification, solid-state phase transformation, and phase separation, where the interfaces play a crucial role in determining the final microstructure.

PF models have been utilized to investigate solidification behavior and have undergone multiple iterations to replicate real-world processes, such as the AM process. The first PF model was developed in 1985 [22], capable of simulating the solidification of pure substances where heat diffusion controlled the process. In their simplest form where the surface energy is assumed to be isotropic, the solidification of pure materials can be expressed as [19]

$$\tau \partial_t \phi = W^2 \nabla^2 \phi - \frac{\partial F(\phi, \lambda u)}{\partial \phi} \tag{1.1}$$

$$\partial_t u = D \nabla^2 u + \partial_t h(\phi)/2 \tag{1.2}$$

where ϕ is the order parameter that represents solid($\phi = 1$), liquid($\phi = -1$) or solid-liquid interface ($-1 < \phi < 1$), $F(\phi, \lambda u) = f(\phi) + \lambda g(\phi) u$ is a double-well potential

function that has two minima at $\phi = 1$ and $\phi = -1$, $u = (T - T_M)/(L/c_p)$ represents the dimensionless temperature field, W is the interface thickness, $h(\phi)$ is a function that describes the generation of latent heat, τ is the characteristic time of attachment of atoms at the interface, λ is a coupling coefficient, D is the thermal diffusivity, T_M is the melting temperature, L is the latent heat of melting, c_p is the specific heat at constant pressure. Subsequently, these models were shown to agree quantitatively with the well-established Stefan or Sharp-Interface model [17, 19].

PF models were then further utilized to study binary alloy solidification by coupling the phase field with a concentration field [21]. Binary PF models were developed by augmenting the free energy density with the contribution of solute B molecules and accounting for solute diffusion. While the construction of binary alloy PF models marked a significant milestone in the field of computational materials science, utilizing these models for quantitative predictions on experimentally relevant length and time scales presented a formidable challenge. The primary challenge emerged from the inherent differences in length scales between the actual solid-liquid interface width and the diffusive transport of solute within bulk phases. Bridging this disparity became essential for accurate modeling. One effective solution was the adoption of a mesoscopic interface thickness, which allowed for more realistic predictions of phase transformations. However, this adoption introduced certain numerical artefacts of non-equilibrium effects, among which the solute trapping effect was particularly notable. This effect arises from the asymmetric solute diffusion rates in solid and liquid phases, leading to the solute trapping at the solid side of the solid-liquid interface. To address this issue, a pivotal advancement in binary alloy PF models was the introduction of an anti-trapping flux mechanism. This innovation played a critical

role in correcting spurious solute trapping phenomena, especially when utilizing thin interfaces within the models. The incorporation of the anti-trapping flux not only improved the predictive capabilities of binary PF models but also enhanced their fidelity in simulating real-world solidification processes. [18, 23].

Considering that commercial alloys are predominantly comprised of multiple alloying elements, developing multi-component PF models became a vital task. Around 2000, various approaches were undertaken to develop multi-component PF models, the two main approaches being the multi-order parameter approach and multi-phase field models [17]. In the multi-order parameter models, the phase fields are treated as physical order parameters that distinguish between ordered and disordered phases [24, 25]. In contrast, multi-phase field models utilize a phase-fraction field to describe all phases [26, 27]. Recently, a multi-component and multi-order parameter grand potential PF model was developed by Provatas et al.[28, 29, 30], which offers a numerical efficiency advantage in large scale simulations. One of the primary constraints traditionally encountered with PF models on the scale of real-world experiments is associated with the upper limit of the interface width W. This parameter plays a pivotal role in shaping the distribution of solute species around the solid-liquid interface, exerting a significant influence on critical calculations such as interfacial energy and dendrite growth kinetics. These limitations have historically hindered the accurate representation of microstructural phenomena at experimental scales. However, the grand potential PF model offers an innovative solution to this challenge. In contrast to traditional PF models that evolve the concentration field, the grand potential model dynamically evolves the chemical potential. This key distinction allows for the precise specification of the interface width to match the

actual microstructural scale observed in experiments. By introducing this level of flexibility, the grand potential model empowers researchers to bridge the gap between computational simulations and real-world observations, facilitating a deeper and more accurate understanding of complex materials phenomena.

While numerous multi-component PF models have been developed, only a few of them have been actually applied to solidification problems at the scale of the process. One challenge for the multi-component PF models is high computational cost. To improve the computational efficiency, a series of novel dynamic adaptive mesh refinement (AMR) algorithms for PF models were developed [28, 31, 32]. The AMR algorithm was developed based on the fact that the majority of the solidification kinetics occur at the solid/liquid interface, thus it would be reasonable to use a coarser grid in the region away from the solid/liquid interface. [28]. The AMR can greatly improve the computational efficiency of the PF simulations. A recently developed AMR methodology could realize 1-2 orders of magnitude speed up compared to the uniform mesh [28]. While high computational cost of all PF models can be partly alleviated using the AMR algorithm, the calculation of multi-component phase equilibrium further increase the computational cost of a multi-component PF model. The calculation of phase equilibrium plays a crucial role in developing a PF model. While determining phase equilibrium is straightforward in pure materials and binary alloys, relying on parameters like the melting temperature (T_M) and partition coefficient (k) to represent equilibrium states, the complexity escalates significantly in the context of multi-component alloys. In these scenarios, achieving local equilibrium becomes contingent upon local composition and temperature, introducing formidable challenges to the calculation process. So, the calculation of multi-component phase equilibrium

is still an open question for the PF community. A high-accuracy phase equilibrium prediction approach requires the calculation of phase equilibrium at every node each time step using a mathematical approach such as Least Squares or Newton-Raphson, but this is computational expensive [33]. The alternative approach is to simplify the Multi-component system to a pseudo-binary approach [34, 35], whose accuracy has not been validated. In summary, an accurate and efficient multi-component phase equilibrium prediction method is lacking. This makes it difficult to perform large scale simulations of a molten pool during AM process utilizing multi-component PF models.

1.2 Motivation

AM has experienced a booming development over the past 30 years. At present, there are many relatively mature applications of AM in the aircraft, re-manufacturing and bio-medical industries. The global metal AM market expects to continue grow annually by about USD $8b over the next 10 years [13]. Titanium alloys share an important segment in the metal AM market, because of their superior specific strength, and their high buy-to-fly ratio in conventional machining process [1]. However, much experimental research has found that coarser columnar grains tend to form in the additively manufactured titanium components [9]. Moreover, some manufacturing experts are not optimistic about the future of the AM market. The control of the product quality is a critical challenge for the AM techniques, and the construction of process-structure-property relationship during AM process plays a crucial role.

Modeling approaches are ideal tools to fill the gap and provide comprehensive insight about the AM process, while saving time and experimental cost. The Phase

Field model is one of the most popular model to simulate solidification during AM process [28]. However, at present, only a few multi-component PF models have been applied to simulate the microstructural evolution during AM process, and the high computational cost is a main challenge. So, it is urgent to develop a highly efficient multi-component PF model, which can be used to perform large-scale simulations on the scale of a molten pool for both PBF and DED. Additionally, the linkage between the process parameters, thermal conditions, microstructure and properties during different AM process is needed to be constructed using the multi-component PF model.

1.3 Research Objectives

This thesis aims to develop a highly efficient multi-component phase field model for cubic alloys. Then, the linkage between processing parameters, thermal history and microstructure during two different AM process need to be explored using the multi-component PF model. Ti-185, a low cost Fe-containing β Ti-alloy, is the main focus of this thesis. The specific objective of this research can be divided into four areas:

1. To develop an efficient and accurate multi-component phase field model for the solidification of cubic alloys. Specifically, to develop an efficient phase equilibrium calculation method, which can predict the multi-component phase equilibrium at varying temperatures for use in the multi-component PF model;

2. To verify the multi-component PF model by performing a benchmark analysis against other well-accepted PF models for multi-component alloy solidification;

3. To apply the multi-component PF model on the LPBF process of a Ti-185

alloy. Then, to compare the influence of using pre-alloyed powder and elemental powder on the dendrite morphology and microsegregation; and

4. To apply the multi-component PF model on the WAAM process of the Ti-185 alloy, and to validate the multi-component PF model against the experimentally characterized solidification microstructure. Then, to establish a solidification process map, which can predict the columnar to equiaxed transition at varying thermal conditions.

1.4 Thesis Outline

The main findings of this thesis have been written in three journal papers and a conference paper. Thus, this thesis including the following chapters:

Chapter 1 briefly introduces the background of titanium alloys, the AM process and PF modeling, as well as the motivation behind this research and the thesis objectives.

Chapter 2 is the first published journal paper that fulfills objective 1. In this study, a new method for temperature-dependent phase equilibrium calculation for use in multi-component PF models is proposed. The PF model is then applied to the 1-dimensional solidification of a Ti-185 alloy, with the accuracy of the proposed phase equilibrium prediction methodology being verified against the commercial software Thermo-Calc.

Chapter 3 is the second published journal paper that addresses objective 2. The multi-component PF model is further verified via performing a benchmark analysis on different 2-dimensional models of solidification in multi-component alloys. Specifically, the multi-component phase field model is compared with two pseudo binary model on the solidification of the Ti-185 alloy. In this study, the isothermal solidification and directional solidification of the Ti-185 alloy are simulated by the three models, where the solute distribution, dendrite growth kinetics and the microstructure snapshot are compared.

Chapter 4 is a published conference paper that satisfies objective 3. In this chapter, the multi-component PF model is applied to simulate the LPBF process of the Ti-185 alloy. A finite element model is developed to simulate the thermal history during the LPBF process. Additionally, two large-scale PF simulations are performed to simulate the microstructure evolution during LPBF process using pre-alloyed powder and blended elemental powder. This work aims to provide a clear picture of the in situ alloying process and improve our fundamental understanding of the competitive growth phenomenon.

Chapter 5 is the third journal paper that investigates the WAAM process in order to address objective 4. This study aims to construct the solidification process map of the Ti-185 alloy, and to utilize the developed solidification process map on WAAM processing. The solidification process map is constructed in this chapter by performing a series of directional solidification simulations under different temperature gradient and pulling velocity, then the influence of WAAM process parameters on the CET was explored using the solidification process map. The

WAAM simulation results are validated via comparing with experimental characterized microstructure.

Chapter 6 summarizes the overall conclusions of this thesis, introduces the highlight and limitations of this study, and presents suggestions for future work.

References

[1] D. Bhaskar and H. Francis, "Additive manufacturing of titanium alloys: State of the art, challenges, and opportunities," 2016.

[2] A. Agapovichev, A. Sotov, V. Kokareva, and V. Smelov, "Possibilities and limitations of titanium alloy additive manufacturing," in *MATEC Web of Conferences*, vol. 224, p. 01064, EDP Sciences, 2018.

[3] Z. Lin, K. Song, and X. Yu, "A review on wire and arc additive manufacturing of titanium alloy," *Journal of Manufacturing Processes*, vol. 70, pp. 24–45, 2021.

[4] P. Barriobero Vila, "Phase transformation kinetics during continuous heating of $\alpha+\ \beta$ and metastable β titanium alloys," tech. rep., DOOR-User, 2015.

[5] P. J. Bania, "Beta titanium alloys and their role in the titanium industry," *Jom*, vol. 46, pp. 16–19, 1994.

[6] S. Ankem and C. Greene, "Recent developments in microstructure/property relationships of beta titanium alloys," *Materials Science and Engineering: A*, vol. 263, no. 2, pp. 127–131, 1999.

[7] H. Azizi, H. Zurob, B. Bose, S. R. Ghiaasiaan, X. Wang, S. Coulson, V. Duz, and A. Phillion, "Additive manufacturing of a novel ti-al-v-fe alloy using selective laser melting," *Additive Manufacturing*, vol. 21, pp. 529–535, 2018.

[8] F. F. Ahmed, S. J. Clark, C. L. A. Leung, L. Stanger, J. Willmott, S. Marussi, V. Honkimaki, N. Haynes, H. S. Zurob, P. D. Lee, *et al.*, "Achieving homogeneity in a high-fe β-ti alloy laser-printed from blended elemental powders," *Materials & Design*, vol. 210, p. 110072, 2021.

[9] J. Li, X. Zhou, M. Brochu, N. Provatas, and Y. F. Zhao, "Solidification microstructure simulation of ti-6al-4v in metal additive manufacturing: A review," *Additive Manufacturing*, vol. 31, p. 100989, 2020.

[10] P. Mohammadpour, *Computational and Experimental Study of the Microstructure Evolution of Inconel 625 Processed by Laser Powder Bed Fusion*. PhD thesis, 2023.

[11] W. E. Frazier, "Metal additive manufacturing: a review," *Journal of Materials Engineering and performance*, vol. 23, pp. 1917–1928, 2014.

[12] J. Shah, B. Snider, T. Clarke, S. Kozutsky, M. Lacki, and A. Hosseini, "Large-scale 3d printers for additive manufacturing: design considerations and challenges," *The International Journal of Advanced Manufacturing Technology*, vol. 104, no. 9-12, pp. 3679–3693, 2019.

[13] A. Vafadar, F. Guzzomi, A. Rassau, and K. Hayward, "Advances in metal additive manufacturing: a review of common processes, industrial applications, and current challenges," *Applied Sciences*, vol. 11, no. 3, p. 1213, 2021.

[14] B. Mueller, "Additive manufacturing technologies–rapid prototyping to direct digital manufacturing," *Assembly Automation*, vol. 32, no. 2, 2012.

[15] X. Shi, S. Ma, C. Liu, Q. Wu, J. Lu, Y. Liu, and W. Shi, "Selective laser melting-wire arc additive manufacturing hybrid fabrication of ti-6al-4v alloy: Microstructure and mechanical properties," *Materials Science and Engineering: A*, vol. 684, pp. 196–204, 2017.

[16] J. Wang, X. Lin, J. Wang, H. Yang, Y. Zhou, C. Wang, Q. Li, and W. Huang, "Grain morphology evolution and texture characterization of wire and arc additive manufactured ti-6al-4v," *Journal of Alloys and Compounds*, vol. 768, pp. 97–113, 2018.

[17] N. Provatas and K. Elder, *Phase-field methods in materials science and engineering*. John Wiley & Sons, 2011.

[18] B. Echebarria, R. Folch, A. Karma, and M. Plapp, "Quantitative phase-field model of alloy solidification," *Physical review E*, vol. 70, no. 6, p. 061604, 2004.

[19] A. Karma and W.-J. Rappel, "Quantitative phase-field modeling of dendritic growth in two and three dimensions," *Physical review E*, vol. 57, no. 4, p. 4323, 1998.

[20] J. Kundin, L. Mushongera, and H. Emmerich, "Phase-field modeling of microstructure formation during rapid solidification in inconel 718 superalloy," *Acta Materialia*, vol. 95, pp. 343–356, 2015.

[21] J. A. Warren and W. J. Boettinger, "Prediction of dendritic growth and microsegregation patterns in a binary alloy using the phase-field method," *Acta Metallurgica et Materialia*, vol. 43, no. 2, pp. 689–703, 1995.

[22] J. B. Collins and H. Levine, "Diffuse interface model of diffusion-limited crystal growth," *Physical Review B*, vol. 31, no. 9, p. 6119, 1985.

[23] A. Karma, "Phase-field formulation for quantitative modeling of alloy solidification," *Physical review letters*, vol. 87, no. 11, p. 115701, 2001.

[24] J. Zhu, T. Wang, A. Ardell, S. Zhou, Z. Liu, and L. Chen, "Three-dimensional phase-field simulations of coarsening kinetics of γ particles in binary ni–al alloys," *Acta materialia*, vol. 52, no. 9, pp. 2837–2845, 2004.

[25] J. Zhu, T. Wang, S. Zhou, Z. Liu, and L. Chen, "Quantitative interface models for simulating microstructure evolution," *Acta materialia*, vol. 52, no. 4, pp. 833–840, 2004.

[26] B. Böttger, J. Eiken, and I. Steinbach, "Phase field simulation of equiaxed solidification in technical alloys," *Acta materialia*, vol. 54, no. 10, pp. 2697–2704, 2006.

[27] I. Steinbach and M. Apel, "Multi phase field model for solid state transformation with elastic strain," *Physica D: Nonlinear Phenomena*, vol. 217, no. 2, pp. 153–160, 2006.

[28] M. Greenwood, K. Shampur, N. Ofori-Opoku, T. Pinomaa, L. Wang, S. Gurevich, and N. Provatas, "Quantitative 3d phase field modelling of solidification

using next-generation adaptive mesh refinement," *Computational Materials Science*, vol. 142, pp. 153–171, 2018.

[29] Z. Li, M. Greenwood, and A. Phillion, "Fast prediction of phase equilibrium at varying temperatures for use in multi-component phase field models," *Computational Materials Science*, vol. 206, p. 111251, 2022.

[30] H. Azizi, A. Ebrahimi, N. Ofori-Opoku, M. Greenwood, N. Provatas, and M. Mohammadi, "Characterizing the microstructural effect of build direction during solidification of laser-powder bed fusion of al-si alloys in the dilute limit: a phase-field study," *Acta Materialia*, vol. 214, p. 116983, 2021.

[31] N. Provatas, N. Goldenfeld, and J. Dantzig, "Efficient computation of dendritic microstructures using adaptive mesh refinement," *Physical Review Letters*, vol. 80, no. 15, p. 3308, 1998.

[32] N. Provatas, N. Goldenfeld, and J. Dantzig, "Adaptive mesh refinement computation of solidification microstructures using dynamic data structures," *Journal of computational physics*, vol. 148, no. 1, pp. 265–290, 1999.

[33] J. Eiken, B. Böttger, and I. Steinbach, "Multiphase-field approach for multicomponent alloys with extrapolation scheme for numerical application," *Physical review E*, vol. 73, no. 6, p. 066122, 2006.

[34] S. Sahoo and K. Chou, "Phase-field simulation of microstructure evolution of ti–6al–4v in electron beam additive manufacturing process," *Additive manufacturing*, vol. 9, pp. 14–24, 2016.

[35] L. Nastac, "Solute redistribution, liquid/solid interface instability, and initial transient regions during the unidirectional solidification of ti-6-4 and ti-17 alloys," *CFD Modeling and Simulation in Materials Processing*, pp. 123–130, 2012.

Chapter 2

Fast prediction of phase equilibrium at varying temperatures for use in multi-component phase field models

Complete Citation:

Li, Z., M. Greenwood, and A. B. Phillion. "Fast prediction of phase equilibrium at varying temperatures for use in multi-component phase field models." Computational Materials Science 206 (2022): 111251.

Fast prediction of phase equilibrium at varying temperatures for use in multi-component phase field models

Z. Li[1], M. Greenwood[1,2], A.B. Phillion[1]

[1]*Department of Materials Science and Engineering, McMaster University, Hamilton, Canada*

[2]*Canmet MATERIALS, Natural Resources Canada, 183 Longwood Road south, Hamilton, ON, Canada*

Abstract: A new method for temperature-dependent phase equilibrium prediction for use in multi-component phase field models of solidification is proposed. The method consists of two parts. First, the convex hull method is applied to predict the phase equilibrium at a single temperature. Second, a set of linear equations is developed to extend the equilibrium calculation over a range of temperatures. These linear equations are derived as an extension of the equation used for solidification of binary alloys in approximating the equilibrium state of multi-component systems. Phase field simulations of solidification of a Ti-Al-V-Fe alloy are performed to demonstrate the effectiveness of the present approach under isothermal and continuous cooling conditions. The results are compared against Thermo-Calc calculations, and indicate that a high accuracy of equilibrium prediction is achieved at a single and multiple temperatures, thus demonstrating that this approach can be successfully applied to the multi-component phase field models.

Keywords: Phase field model, Multi-component alloys, Phase equilibrium, Solidification

2.1 Introduction

Over the last 30 years, the Phase Field (PF) model has become a popular method for solving free boundary problems in materials science and engineering [1, 2]. By introducing an order parameter, direct interface tracking is avoided while still allowing for simulation of the evolution of topologically complex dendrites. The PF model has been applied to study solidification and solid-state phase transformations in many different metallic alloy systems (e.g. [3, 4]).

With respect to the problem of solidification, while binary alloy PF models are computationally efficient, simulating multi-component alloy systems significantly increases the complexity and thus computational cost. Over the years, various strategies have been employed to improve this computational efficiency. These strategies can be classified into two major categories: pseudo-binary model and direct multi-component model with simplified thermodynamic description.

The pseudo-binary PF model is a popular approach (e.g. [5, 6]) in which a hypothetical solute is created that represents a combination of all solute elements within the alloy. Thus, the multi-component system is simplified to a binary one and the corresponding PF model contains only one concentration field. In the pseudo-binary model, the partition coefficient k, liquidus slope m_l and solidus slope m_s of the hypothetical alloy are given by the weighted-average-sum of all k, m_l and m_s values from the individual alloying elements. The advantage of the pseudo-binary model is greatly reduced computational time. However, it is impossible to track the spatial variation of any one specific element.

In order to track the distribution of a specific element, a fully multi-component PF model is needed. The literature contains many different multi-component PF models,

such as the models by Nestler et al. [3] and by Kim [4], but their computational cost is quite high due to the need for a thin interface. Recently, Provatas et al. [7, 8] developed a multi-component PF model based on the grand potential ensemble whereby the difference in the grand potential between solid and liquid phases are used as a driving force for solidification, and rather than traditional solute concentration [9], the evolution of chemical potential is tracked. Thus, complete decoupling of the solute concentration field and the order parameter field is achieved, which allows one to set interfacial energy independent of the solute distribution across the interface. As a result, the interface width can be scaled larger than the physical interface width within the limits of the length scales of the problem, which is essential for large scale PF simulations [10].

Modern thermodynamic databases of alloys have become common by utilizing the CALPHAD approach [11]. However, it remains an open question of how to best couple such databases to a multi-component PF model. The most basic approach has been a direct coupling between the thermodynamic database and PF. Unfortunately, this means that the phase equilibrium must be calculated every time step for each node utilizing a mathematical approach such as Least Squares or Newton–Raphson [12, 13]. For large domains, these time-consuming mathematical techniques make multi-component PF simulation even more computationally expensive. While local equilibrium is utilized in many well-accepted binary PF models [14, 15], some studies have adopted a quasi-equilibrium simplification to overcome the challenge of high computational cost (e.g. [12, 16]). The model of Böttger et al., for example, calculated the equilibrium state via parallel tangents instead of the common tangents [16]. While computationally efficient, the accuracy of this approach

has not yet been validated against experimental or other CALPHAD results. A detailed comparison between the quasi-equilibrium approach and the local equilibrium approach is given in the Section 2.3.1. Another alternative, proposed by Kobayashi et al. [17], is to calculate the phase diagram before the simulation and express it as a look-up table. Although a high accuracy in the phase equilibrium is obtained with this approach, the computation time remains too high as an additional subroutine needs to be recalled for each node at every time step. A second alternative, proposed by Jiang et al. [12], is to use a neural network model to predict the phase equilibrium. However, the accuracy of this approach is highly dependent on the amount of training data thus necessitating large initial computational overhead every time the alloy system changes.

To reduce the time-intensive thermodynamic equilibrium calculations needed for multi-component PF solidification models, simplified thermodynamic descriptions need to be developed. Given that the equilibrium free energy surface is built based on a global energy minimization process, there is an inherent convexity to its shape and thus it can be approximated via a convex hull. The convex hull method has been applied to solve phase equilibrium since nearly 30 years ago [18], but it was not widespread due to the limited computational resources available in the 1990s [13]. Recently [19], the convex hull method has been used to reconstruct binary, ternary and even quaternary phase diagrams at a single temperature, but their performance was poor owing to the need to achieve a balance between accuracy and computation time while using a fixed-grid spacing. For example, when using the convex hull method, Perevoshchikova et al. [20] found that a finer grid size could be used to achieve a higher accuracy in phase equilibrium prediction. However, this would inevitably lead

to a longer computational time. What's more, the common super-saturation equations within modern PF models need not only the equilibrium concentration, but also the compositional dependent equilibrium chemical potential. At present, these values have not been calculated by the aforementioned approaches.

The influence of temperature on phase equilibrium adds additional complexity to microstructure prediction via PF models. A number of different interpolation and extrapolation methods have been developed to include temperature-dependence while also keeping calculation time to a minimum [16, 21]. Böttger et al. simulated via PF the solidification process of a multi-component alloy under a constant cooling rate. In their study, phase equilibrium was calculated by an iterative Newton–Raphson scheme at several selected temperatures, while linear interpolation was applied for intermediate temperatures [16]. However, numerous time-consuming phase equilibrium calculations were required in order to obtain high accuracy. Echebarria et al. utilized a concise method based on linear extrapolation that included physical properties and process parameters to express the temperature dependence of phase equilibrium for simulating the directional solidification of a binary alloy [22]. This last method, presented in detail in Section 2.3.3, is now commonly used in binary PF models(e.g. [6, 15, 23, 24]) but has not yet been extended to multi-component systems.

It is well known that high computational cost is a main challenge for PF simulations, particularly for multi-component alloys. A complete solution for quickly predicting phase equilibrium in multi-component systems, over a range of temperatures, is still lacking. In the present study, a new and efficient method for calculating the local pairwise phase equilibrium at varying temperatures is proposed. This method

utilizes an efficient algorithm incorporating convex hulls to calculate the equilibrium chemical potentials as a function of composition. These equilibrium chemical potentials are then coupled to a temperature interpolation that utilizes Echebarria's approach [22] to produce temperature dependence. The present method is designed for the prediction of two-phase equilibrium in pairwise combinations. This allows for the integration into phase field models which work on the basis of local pairwise free energy interactions. In general the equilibrium surface constructions with the convex hull approach can be extended to multiple phases, but is not validated in this work.

High computational efficiency is achieved by using the present method because the time-consuming phase equilibrium calculation is completed before the start of the PF simulation. This method additionally has the advantage of maintaining the local equilibrium state.

The manuscript is organized as follows. First, Section 2.2 briefly introduces the multi-component phase field model used in the manuscript, which motivates the calculation of the phase equilibrium in multi-component alloys. Then, Section 2.3 describes the methods of the phase equilibrium calculation. Finally, Section 2.4 reports an error estimation process where a comparison of the results between the new method and the underlying CALPHAD (Thermo-Calc) calculations is carried out for model verification, and a 1D PF simulation of the solidification of a Ti-Al-V-Fe quaternary alloy is performed to explore the ability of this new method to support PF simulations of multi-component alloy solidification.

2.2 Governing equations for the multi-component PF model

The multi-component phase field model used in this study was developed by Provatas et al. [7, 8] with the aim of quantitatively simulating large-scale alloy solidification problems having a free energy function that can be described by a quadratic equation. This approach begins by expressing the free energy surface as

$$F^{\theta}\left(c_1, c_2, ...c_n - 1\right) = \frac{1}{2}\sum_{i=1}^{n-1}\sum_{j=1}^{n-1} A_{ij}^{\theta}\left(c_i - \bar{c}_i^{\theta}\right)\left(c_j - \bar{c}_j^{\theta}\right) + \sum_{j=1}^{n-1} B_j^{\theta}\left(c_j - \bar{c}_j^{\theta}\right) + D^{\theta}, \quad (2.1)$$

where the free energy of bulk phase θ, F^{θ}, is calculated based on the local concentrations of component i and j, i.e. c_i and c_j and fitting parameters A_{ij}^{θ}, $\bar{c}_i^{\theta}$, B_j^{θ} and D^{θ}. More specifically, first F^{θ} is extracted from a thermodynamic database for a given set of c_i, and second the least squares method is used to identify the values of the fitting parameters that fit the free energy surface to Eq. 2.1 for use in PF simulations. This is a well-accepted form to describe the free energy of massive solid alloy phases [25, 26].

For a given free energy surface, the dynamic equations to obtain the evolution in the order parameter and chemical potential are then derived based on the free energy relaxation principle [7, 8],

$$\tau\frac{\partial\phi}{\partial t}=W^2\nabla^2\phi-f'_{DW}\left(\phi\right)-\left(\frac{\left(I-[K]\right)^T}{2}\vec{U}+\hat{n}_c\right)^T[\lambda]\,\vec{U}g'\left(\phi\right), \tag{2.2}$$

and

$$[\chi]\,\frac{\partial\vec{\mu}}{\partial t}=\nabla\left[[M]\,\nabla\vec{\mu}+Wa\left(\phi\right)|\Delta\vec{c}_{eq}|\{\hat{n}_c+\left(I-[K]\right)^T\vec{U}\}\frac{\partial\phi}{\partial t}\frac{\nabla\phi}{|\nabla\phi|}\right] + \frac{1}{2}|\Delta\vec{c}_{eq}|\{\hat{n}_c+\left(I-[K]\right)^T\vec{U}\}\frac{\partial\phi}{\partial t}, \tag{2.3}$$

where ϕ is the order parameter, $\vec{\mu}$ is a vector constituting of the chemical potential of each solute components μ_i(vector $\vec{\mu}_{eq}$, $\vec{c}^{L}_{eq}$ and $\vec{c}^{S}_{eq}$ are also used later to better represent multiple components of multi-component alloys), τ is the relaxation time, W is the interface width scale, I represents the identify matrix, $f'_{DW}\left(\phi\right)$ is a classic double well potential function, $a\left(\phi\right)=\sqrt{2}/2$, [7, 8] and where

$$\left[\chi^{\theta}\right]^{-1}_{ij}=A^{\theta}_{ij}, \tag{2.4}$$

$$\vec{U}=\frac{\left[\chi^{L}\right]}{|\Delta\vec{c}_{eq}|}\left(\vec{\mu}-\vec{\mu}_{eq}\right), \tag{2.5}$$

$$\Delta\vec{c}_{eq}=\vec{c}^{L}_{eq}-\vec{c}^{S}_{eq}, \tag{2.6}$$

$$\hat{n}_c=\frac{\Delta\vec{c}_{eq}}{|\Delta\vec{c}_{eq}|}, \tag{2.7}$$

$$[K] = \left[\chi^L\right]^{-1} \left[\chi^S\right], \tag{2.8}$$

$$[\lambda] = \hat{\lambda} |\Delta \vec{c}_{eq}|^2 \left[\chi^L\right]^{-1}, \tag{2.9}$$

$$[\chi] = \left[\chi^L\right] \{I - (I - [K])\, h(\phi)\}, \tag{2.10}$$

and

$$[M] = q(\phi) \left[D^S\right] \left[\chi^S\right] + (1 - q(\phi)) \left[D^L\right] \left[\chi^L\right]. \tag{2.11}$$

In this set of equations, $\hat{\lambda}$ is the dimensionless coupling coefficient , $h(\phi)$ and $q(\phi)$ are interpolation equations commonly used in PF models, $\left[D^\theta\right]$ is the diffusion coefficient matrix that is related to the physical properties of the alloy system, and matrices $[K]$ and $\left[\chi^\theta\right]$ are related to the free energy surface given in Eq. 2.1 [7, 8].

Altogether, Eqs. 2.2-2.11 provide a complete description of the PF model, however the equilibrium chemical potentials for each component $\vec{\mu}_{eq}$ and the equilibrium solute concentrations for each component in each phase $\vec{c}^{\,L}_{eq}$ and $\vec{c}^{\,S}_{eq}$, remain as unknown parameters. These are related to the equilibrium state of the system and need to be calculated before initiating the simulation. The subject of the present research is to provide a complete solution, via the Convex Hull with Temperature (CHT) calculator, for these equilibrium state calculations.

2.3 Prediction of Phase equilibrium in multi-component alloy systems

2.3.1 Comparison of phase equilibrium prediction between binary and multi-component alloy systems

Most PF models of solidification processes assume that local equilibrium is maintained at the solid/liquid interface, i.e. the temperature, pressure and chemical potential at the interface are identical in both phases. Numerically, this can be calculated by finding the common tangent line (binary system) or common tangent hyper surface (multi-component system) from the free energy data for both phases. The construction of common tangents can be expressed as

$$\frac{\partial F^S\left(c_1^S, c_2^S, ..., c_{n-1}^S\right)}{\partial c_i^S} = \frac{\partial F^L\left(c_1^L, c_2^L, ..., c_{n-1}^L\right)}{\partial c_i^L} \tag{2.12}$$

$$\sum_{i=1}^{n-1}\left(\left(c_i^S - c_i^L\right)\frac{\partial F^S\left(c_1^S, c_2^S, ..., c_{n-1}^S\right)}{\partial c_i^S}\right) = F^S\left(c_1^S, c_2^S, ..., c_{n-1}^S\right) - F^L\left(c_1^L, c_2^L, ..., c_{n-1}^L\right) \tag{2.13}$$

$$\frac{c_i^S - c_i^L}{c_j^S - c_j^L} = \frac{c_{i,local} - c_i^L}{c_{j,local} - c_j^L} \tag{2.14}$$

where c_i^S and c_i^L are the equilibrium concentration of the i th component in the solid and liquid phase, F^S and F^L are the Helmholtz free energy of solid and liquid phase,

and $c_{i,local}$ is the actual local composition of the ith component.

The finding of the common tangent line is trivial for binary alloys. However, the complexity in finding the common tangent hyper surface in multi-component alloys increases significantly when increasing the number of alloying elements. Fig. 2.1 shows schematically the free energy surface for a binary and a ternary alloy at an arbitrary temperature in a two phase region. As can be seen for the binary case, Fig. 2.1(a), the thermodynamic equilibrium is obtained by constructing a common tangent line to both free energy curves. Since with fixed temperature and pressure there is only one tie line, it is not complicated to determine $\vec{\mu}_{eq}$, $\vec{c}^{L}_{eq}$, and $\vec{c}^{S}_{eq}$. Thus, the partition coefficient (assuming it is constant) is sufficient to represent the equilibrium state of the binary alloy. The calculation of thermodynamic equilibrium is much more complex for the case of multi-component alloy systems since multiple tangent planes can be created between two free energy surfaces. Fig. 2.1 (b) shows one such tangent plane, and correspondingly, one tie line (solid line) between the solid and liquid phases. However, other tie lines (examples given as dashed lines) can also be drawn for the other tangent planes. Thus, the representation of the overall phase equilibrium in multi-component systems becomes a n-dimensional hyper surface of equilibrium tie lines.

Returning now to the concept of quasi-equilibrium, Böttger et al.'s [16] study proposed to calculate only Eq. 2.12 when determining the common tangent and not Eqs. 2.13- 2.14. This enables parallel tangents to be constructed thus simplifying the calculations. Local equilibrium is a much stricter condition since common tangents must be constructed via Eq. 2.12- 2.14, thus achieving free energy minimization. It is not simple to solve these equations in a multi-component system.

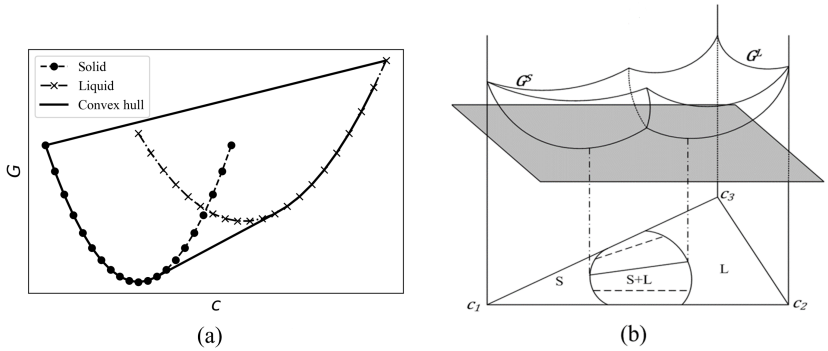

Figure 2.1: Free energy curve for (a) a binary alloy and (b) a ternary alloy at constant pressure and temperature in the two phase region. The common tangent line and plane are indicated to identify the equilibrium $\vec{\mu}_{eq}$, $\vec{c}^{L}_{eq}$, and $\vec{c}^{S}_{eq}$.

2.3.2 Predicting phase equilibrium at one temperature

The new CHT calculator utilizes the convex hull method to calculate local phase equilibrium at a single temperature. Specifically the free energy data at selected concentration points, extracted from a CALPHAD database, are fit to the quadratic free energy form utilized by the phase field model. This free energy data is then utilized as input to a bespoke code which outputs a set of simplex equations that represents the local equilibrium chemical potential/concentration relation via a n-dimensional polynomial surface, i.e. a convex hull. These simplices are then used to generate tie lines for the overall equilibrium calculations.

In addition to showing the free enerugy surface for a binary system, Fig. 2.1(a) schematically shows the process of creating the convex hull. The solid circle and cross represent data extracted from a thermodynamic database. The dotted lines represent the quadratic free energy form utilized by our PF model. The solid lines represent the simplex equations/convex hull. Note that the solid lines fall on top of the dotted lines in the single phase region of the free energy curves. It is clear from the figure that the common tangent line of the two energy curves is drawn by the convex hull method

by the connected points from one energy curve to the other. This is generalized to n-dimensions creating not a line, but a hyper surface of connected points forming the collection of all tielines. From this hyper-surface we get a relationship for the equilibrium chemical potential as a function of composition. Please note that while the PF model is presently limited to quadratic free energies, the CHT calculator can be utilized for arbitrary free energy descriptions.

The accuracy of the convex hull method for calculating phase equilibria is greatly influenced by the number of free energy points among the concentration space used in the convex hull calculation, especially within the concentration region near the tie line boundaries [20]. The main feature of the CHT calculator is an ability to use arbitrary spacing between the concentration points, thus additional values near the boundaries can easily be added. The convex hull calculation is initialized at concentration points near the intersection of two energy curves. A set of iterations is carried out, with new points added near the tie line boundaries, until convergence is achieved. The resulting equations are of the form $\vec{\mu}_{eq}$, $\vec{c}^{L}_{eq}$, and $\vec{c}^{S}_{eq} = f(c_i, c_j ...)$ and thus efficiently designed for PF calculations where the local solute concentrations are a known quantity from the previous time-step.

The present CHT calculator offer a number of advantages when compared with former convex hull approaches. Firstly, the Gibbs free energies are not discretized on a fixed grid, but on many irregular distributed points. These points are generated iteratively to focus on the boundaries of the tie lines. This removes the systematic shifts in the free energy boundaries that one might observe due to fixed grid resolutions. This also provides orders of magnitude improvement in computational efficiency by eliminating unnecessary calculations at the interior of single phase regions. Additionally,

this convex hull hyper-surface allows for the generation of an equilibrium chemical potential $\vec{\mu}_{eq}$ as a function of the local composition. This $\vec{\mu}_{eq}(\vec{c})$ hyper-surface make it easier and efficient to integrate with the multi-component phase field model.

2.3.3 Predicting phase equilibrium at multiple temperatures

The methodology described above provides a concise description of phase equilibrium predictions at a single temperature. However, practical use for PF simulation of solidification requires non-isothermal processing conditions. Although a number of convex hull calculations at multiple single temperatures could theoretically be used to fit and approximate the temperature dependence, this would significantly increase simulation complexity and computational effort.

Echebarria et al. [22] proposed a concise approach to calculate the influence of temperature on the equilibrium concentration in a binary system that is based on a solution to the problem of concentration variation given a steady-state planar solid/liquid interface,

$$\frac{c_T^{L^*}}{c_{T^{ref}}^{L^*}} = 1 - (1-k)\, d_0\kappa - (1-k)\, \beta V_n - (1-k)\, \frac{T - T^{ref}}{\Delta T_f} \tag{2.15}$$

where $c_T^{L^*}$ is the concentration of solute on the liquid side of the interface at temperature T, $c_{T^{ref}}^{L^*}$ is the solute concentration in the liquid at a reference temperature T^{ref}, k is the partition coefficient, d_0 is the chemical capillary length, κ is the interface curvature, β is the kinetic coefficient, V_n is the interface velocity, ΔT_f is the freezing range.

Eq. 2.15 describes the influence of temperature on equilibrium concentrations in binary alloy. The present study extends this approach to multi-component systems assuming a linear dependence between temperature and phase equilibrium,

$$c^L_{i,eq,T} = c^L_{i,eq,T^{ref}} - \frac{T - T^{ref}}{\Delta T_f}\left(c^L_{i,eq,T^{ref}} - c^S_{i,eq,T^{ref}}\right) \tag{2.16}$$

$$c^S_{i,eq,T} = c^S_{i,eq,T^{ref}} - \frac{T - T^{ref}}{\Delta T_f}\left(1 - \frac{c^S_{i,eq,T^{ref}}}{c^L_{i,eq,T^{ref}}}\right) c^S_{i,eq,T^{ref}} \tag{2.17}$$

$$\vec{\mu}_{eq,T} = \frac{\left(\vec{\mu}^L_{eq}\left(\vec{c}^L_{eq,T}\right) + \vec{\mu}^S_{eq}\left(\vec{c}^S_{eq,T}\right)\right)}{2} \tag{2.18}$$

where T^{ref} is the temperature at which the CHT calculator is run to give the thermodynamic equilibrium predictions, T is the local temperature for the unknown equilibrium state, $\vec{c}^L_{eq,T^{ref}}$ and $\vec{c}^S_{eq,T^{ref}}$ represent vectors consisting of the equilibrium solute concentration of the ith component $c^L_{i,eq,T^{ref}}$ and $c^S_{i,eq,T^{ref}}$ in the multi-component system at T^{ref} as calculated from the CHT calculator, $\vec{c}^L_{eq,T}$ and $\vec{c}^S_{eq,T}$ represent vectors consisting of the equilibrium solute concentration of the ith component $c^L_{i,eq,T}$ and $c^S_{i,eq,T}$ at T, $\vec{\mu}_{eq,T}$ are the equilibrium chemical potentials at T, and $\vec{\mu}^L_{eq}$ and $\vec{\mu}^S_{eq}$ are the equilibrium chemical potentials calculated from $\vec{c}^L_{eq,T}$, and $\vec{c}^S_{eq,T}$. Please note that there are a number of inherent assumptions with this approach that must be acknowledged. Specifically, these assumptions include: (1) Only two stable phases exist throughout the simulation temperature range; (2) The slopes of the solidus and liquidus with respect to temperature are constant and equal; and (3) The influence of temperature on the free energy curves is negligible when compared with concentration.

2.3.4 Process flow for coupling the Phase Equilibrium Calculator with PF Simulations

The process flow for applying the CHT calculator described in Sections 2.3.2 and 2.3.3 with the PF model from Section 2.2 is depicted in Fig. 2.2. This approach results in a simulation that provides higher computational accuracy and greater computational efficiency that previous methods. First, the local equilibrium is calculated by the bespoke convex hull calculator, which provides higher computational accuracy when compared with other approaches such as [12, 16] because the full local equilibrium is determined and not simply quasi equilibrium. Second, greater computational efficiency is achieved than prior multi-component phase field simulations because the time-consuming phase equilibrium calculation that traditionally is performed at every node via a Least-Squares method is completed in our new approach by using the CHT calculator before the PF simulations are carried out.

In the present study, the Thermo-Calc^{TM} TCTI 2 database is used to provide the free energy data for a quaternary Ti-1Al-8V-5Fe (wt%) alloy in the Ti-Al-V-Fe system. The least squares fit of the free energy data to Eq. 2.1 is made via a bespoke Python code, while the Qhull external library is used to construct the n-dimensional convex hull [27]. The 1-D PF simulation is also carried out using a bespoke Python code. Eq. 2.2 and Eq. 2.3 are discretized using standard finite difference formulas, while the ϕ and the $\vec{\mu}$ fields are time stepped using a first order Euler scheme.

The relevant PF simulation parameters and thermo-physical properties are listed in Table 2.1.

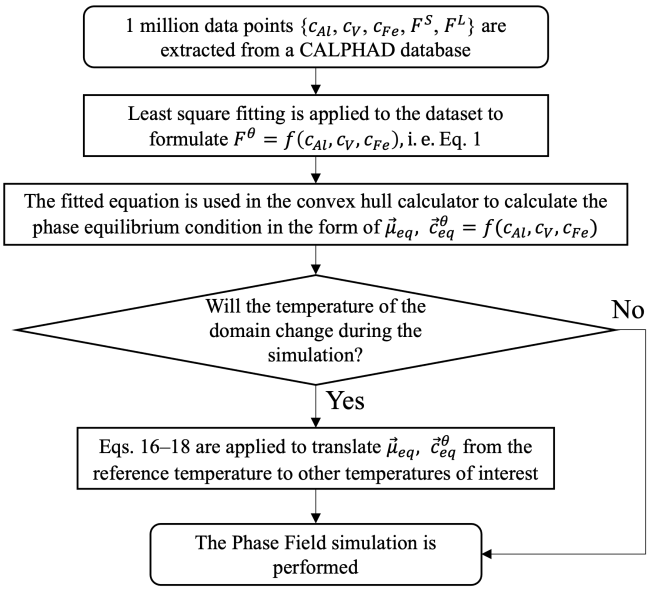

Figure 2.2: Flow chart of phase equilibrium data calculation and transferring process between a CALPHAD database, the CHT calculator and the PF model.

Table 2.1: Simulation parameters and thermo-physical properties of Ti-185 alloy [6][24]

Simulation parameter	Value
λ	6.0
W (m)	9.4E-9
PF mesh spacing (dx)	0.4
Thermo-physical properties	**Value**
Liquidus temperature (K)	1848
Solidus temperature (K)	1705
Gibbs-Thomson Coefficient (K·m)	2.0E-7
$D_L = D_S$ (m^2s^{-1})(Section 4.2.1)	9.5E-9
D_L (m^2s^{-1}) (Section 4.2.2)	9.5E-9
D_S (m^2s^{-1}) (Section 4.2.2)	5.0E-13

2.4 Results and Discussion

The results and discussion are presented in two parts. First, a comprehensive analysis is carried out to compare the phase equilibrium predictions made by the CHT

calculator against those made via Thermo-Calc (TC) single equilibrium calculation using a global Gibbs energy minimization approach. Second, this calculator is applied to the PF simulation of a solidifying Ti-185 alloy under isothermal and continuous cooling conditions.

2.4.1 CHT calculator verification

2.4.1.1 Prediction accuracy at a single temperature

The manner in which free energy data is extracted from a CALPHAD database at T^{ref} is the first and most critical stage for ensuring prediction accuracy by the CHT calculator since this data is then fit to Eq. 2.1 and used as the input to the convex hull library. To demonstrate this importance, consider a dataset in the Ti-Al-V-Fe system consisting of one million data points $\{c_{Al}, c_V, c_{Fe}, F^S, F^L\}$, where F^S and F^L are the Helmholtz free energy of the solid and liquid phases, at 1750 K. Over which solute concentration range should the data be extracted?

Table 2.2 compares the relative error in equilibrium solute concentration for the Ti-185 alloy at 1750 K predicted by the CHT calculator and by TC single equilibrium calculation for five different solute concentration ranges, known as Datasets and given in Table 2.3. As can be seen, for Dataset 1, a very high relative error at 30% is seen to occur in the prediction of the equilibrium Fe concentration in the solid phase c^S_{Fe}, whereas the errors for the other five terms are relatively low ($< 5\%$). Datasets 2-4 were then investigated as a simple optimization to reduce the error in c^S_{Fe}, with the aim to better describe the free energy surface near the tie line boundaries for an alloy with 5 wt.% Fe. During the optimization process, the concentration range of Fe was decreased from 0-20 wt% in Dataset 1 to 2-13 wt% in Dataset 4. Correspondingly,

the relative error of c^S_{Fe} is seen to reach a minimum of 1% in Dataset 3 with $\Delta c_{Fe} = 0-13$ wt% however this resulted in the relative error in c^L_{Fe} to rise to 8%. Interestingly, a further decrease in Δc_{Fe} to 2-13wt% resulted in an increse in the error in c^S_{Fe} to approx. 20% whereas the error in c^L_{Fe} returned to a low value. This is because the solute concentration ranges used for data extraction need to be large enough to depict the overall free energy surface outline as well as the details near the boundaries; $\Delta c_{Fe} = 2 - 13$ wt% is evidently not able to depict the full free energy surface for the solid phase. Finally, Dataset 5 is identified, in which the free energy approximation for the solid phase is calculated from one solute concentration range (Dataset 3), while the free energy approximation for the liquid phase is calculated from a different range (Dataset 4). In this case, the error for all solute concentrations becomes quite low. Although not carried out in this study, given a user-defined maximum allowable relative error, an automated computer code could be developed to determine the optimal solute concentration ranges for data extraction from a CALPHAD database.

Table 2.2: Comparison of relative error ($|c_{\mathrm{CHT}} - c_{\mathrm{TC}}|/c_{\mathrm{TC}}$ [%]) between the CHT calculator and TC single element calculation in predicting the Ti-185 equilibrium solute concentrations in the solid and liquid phases at 1750 K for the five solute concentration ranges given in Table 2.3.

Dataset	c^L_{Al}	c^S_{Al}	c^L_V	c^S_V	c^L_{Fe}	c^S_{Fe}
1	2.11	5.16	2.08	1.48	3.10	29.93
2	3.75	2.11	0.40	1.73	4.10	8.07
3	5.07	7.03	2.28	1.57	7.51	1.08
4	1.82	3.63	0.44	1.54	0.20	18.48
5	1.66	0.06	2.90	0.97	3.11	2.87

Table 2.3: Solute concentration ranges (wt.%) used to extract free energy from TC TCTI2 database at 1750 K for the Ti-185 alloy

Dataset	Δc_{Al}	Δc_V	Δc_{Fe}
1	0-20	0-20	0-20
2	0-2	0-20	0-15
3	0-2	0-20	0-13
4	0-2	0-20	2-13
5	0-2	0-20	0-13 (F^S)
			2-13 (F^L)

2.4.1.2 Prediction accuracy at multiple temperatures

Once the phase equilibrium at a single temperature has been calculated, the equilibrium state at other temperatures can be evaluated via Eqs.(14)-(16). The error inherent in this process can again be determined by comparing the CHT and TC calculator. However, there is additional complexity since a range of interfacial solute concentrations may result during a PF simulation.

Fig. 2.3 compares the mean relative error in the equilibrium solute concentrations predicted by the CHT calculator as compared to TC calculations for 1000 different compositions in the Ti-Al-V-Fe system for 10 temperatures between 1710 and 1800 K assuming that $T^{ref} = 1750$ for the (a) liquid phase and (b) solid phase. The accuracy is quantified by the mean relative error [12]:

$$Y = \frac{1}{N}\sum_{j=1}^{N} |c_{\mathrm{CHT}} - c_{\mathrm{TC}}|/c_{\mathrm{TC}} \tag{2.19}$$

where Y is the mean relative error, N is number of examined alloy compositions at a single temperature, and $c_{i,\mathrm{CHT}}$ and $c_{i,\mathrm{TC}}$ are the equilibrium concentrations for element i =Al, V, and Fe as calculated by the CHT and TC methods [12].

As can be seen in the figure, the mean relative error is below 10% over the entire 90 K temperature range in both the liquid and solid phases. There is a clear trend in Fig. 2.3 that the mean relative errors increase with increasing ΔT. This is not surprising, since the inherent assumption in Eqs. 2.16 and 2.17 is of linear solidus and liquidus lines that remain parallel to each other. While this assumption is not necessarily realistic, it has been used with much success in many prior alloy solidification models. Fig. 2.3 also shows that the prediction of V is more accurate than Al and Fe, likely because the solute redistribution of V between the liquid and solid phases is not so significant as in the other two elements.

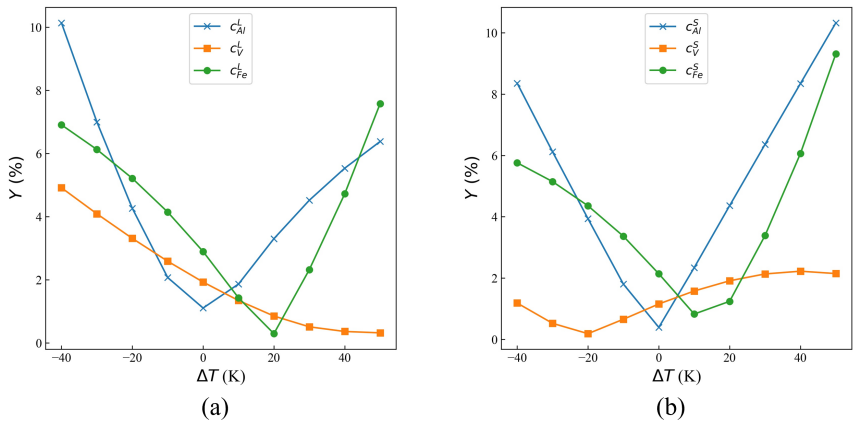

Figure 2.3: Mean relative error in the equilibrium solute concentrations for Al, V, and Fe predicted by the CHT calculator as compared to TC calculations as a function of temperature in the (a) liquid and (b) solid phases.

2.4.2 Use of the CHT calculator within a PF model

With the accuracy of the CHT calculator having been determined in Table 2.2, this tool can now be applied to PF simulations.

2.4.2.1 Isothermal 1-D PF simulation

Fig. 2.4 shows a snapshot of a 1-D PF simulation of Ti-185 alloy isothermal solidification at 1750K and at a fraction solid of 0.81, with the order parameter representing the solid and liquid phases given in (a) and the corresponding spatial variation in solute concentrations shown in (b). At the beginning of the simulation, a nuclei was placed on the left side of the domain, thus solidification proceeds towards the right. It is clear that the occurrence of significant alloy segregation is predicted by this simulation; V, Fe in liquid phase and Al in solid phase. Note that D_S and D_L are assumed to be equal in order to interpret the bulk composition as the equilibrium state.

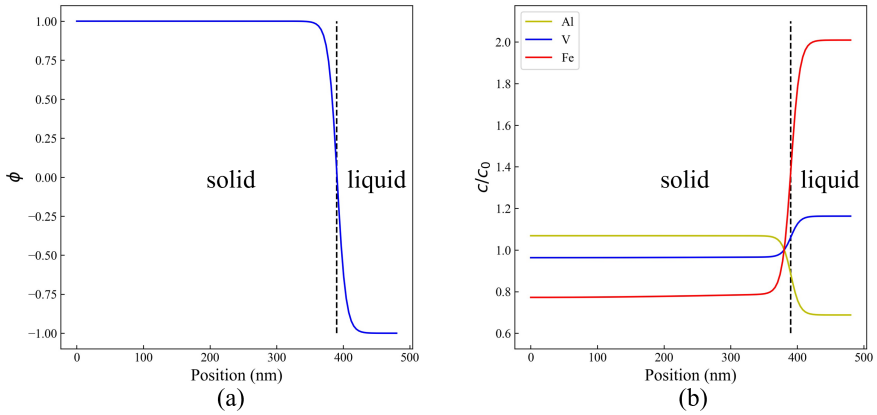

Figure 2.4: Snapshot at $f_s = 0.81$ of the Isothermal PF simulation results for the Ti-185 at 1750 K; (a) Order parameter profile and (b) Normalized Concentration Profile.

Fig. 2.5 compares the equilibrium solute concentrations in the solid and liquid phases for all three solute elements (Al, V, and Fe) as calculated by the PF simulation (blue bar), the CHT calculator (red bar), and the TC single equilibrium calculation (yellow bar). As can be seen, there is a very good agreement between all three

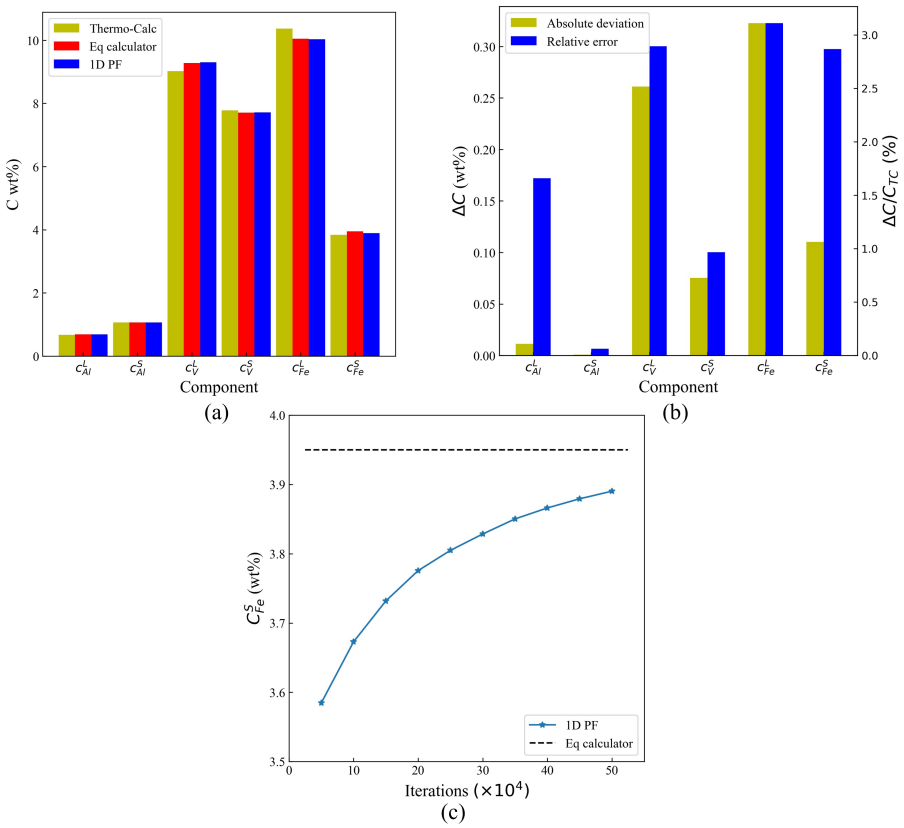

Figure 2.5: (a)Comparison in Ti-185 equilibrium solute concentrations between the PF simulation, the CHT calculator, and the TC single equilibrium calculation, (b)absolute deviation and relative error between the CHT calculator and the TC single equilibrium calculation, and (c) variation of average c^S_{Fe} as a function of simulation time in the PF simulation

approaches. The highest deviation between the CHT and TC calculations occurs for the prediction of $c_{eq,Fe}$ in liquid phase, with a relative error of 3.11 %. The highest converge deviation between the PF simulation and the CHT calculator occurs for the prediction of $c_{eq,Fe}$ in solid phase, with a relative error of 1.51 %, and the PF simulation is terminated here. As shown in Fig. 2.5 (c), the evolution of average concentration of Fe in solid phase during the 1D PF simulation is plotted to show that c^S_{Fe} is converged to the value predicted by current CHT calculator, and the

remaining deviation is due to the fact that equilibrium has not been achieved in this PF simulation. This last point is shown by comparing the PF solid fraction $f_s = 0.81$ with the TC single equilibrium prediction of $f_{eq,s} = 0.82$.

2.4.2.2 Continuous Cooling 1-D PF simulation

Fig. 2.6 shows a snapshot of the 1-D PF simulation during solidification of the Ti-185 alloy, at a temperature of 1710 K, corresponding to a fraction solid of 0.72. In this simulation, the domain was cooled uniformly at a rate of 100 K/s, starting at 1850 K and ending at 1700 K, i.e. temperatures which are slightly above and below the liquidus and solidus values. The order parameter and concentration fields were recorded every 10 K, while the equilibrium solute concentrations needed by the PF simulation were predicted by the CHT calculator. As shown in Table 2.1, $D_S << D_L$.

As can be seen in Fig. 2.6, there is significant alloy segregation. Like Fig. 2.4, there is positive segregation of Fe and V in the liquid, but negative segregation of Al. However, the overall shape of the profile is quite a bit different than in the isothermal case. Due to combination of an imposed cooling rate and having $D_S << D_L$, the variation in segregation in the solid with position is a surrogate for the variation in equilibrium solid composition with temperature. The composition of Al is seen to decrease in the solid, concurrent with the negative segregation seen in the liquid, whereas the opposite is true for the positively segregating Fe (strong) Fe and V (weak).

One of the main benefits of a PF simulation is the ability to investigate the effect of cooling rate on solidification microstructure evolution. Fig. 2.7 plots the evolution in interface concentration on the solid side of the PF simulation with temperature for five different cooling rates for (a) Al, (b) V, and (c) Fe. For these graphs, the solute

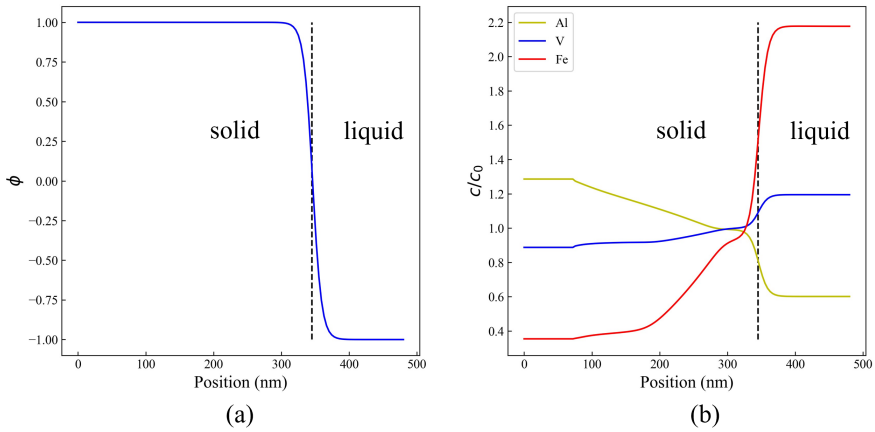

Figure 2.6: Snapshot at 1710 K of the continuous cooling PF simulation results for the Ti-185 at a cooling rate of 100 K/s; (a) Order parameter profile and (b) Normalized Concentration Profile.

concentration is collected from the first node in the 1D PF simulation in which the order parameter $\phi > 0.99$ as that is assumed to identify the solid side of the interface. It should also be noted that we set $D^S = D^L$ in this set of simulations.

As can be seen from Fig. 2.7, all five PF simulations show the same overall solute concentration evolution trend during continuous cooling process from 1850 K to 1700 K, i.e. the concentration of Fe and V gradually increase to the bulk composition (corresponding to their positive segregation ($k < 1$)), while C^S_{Al} gradually decreases to the bulk composition (corresponding to its negative segregation ($k > 1$)). Meanwhile, the relative positions of the plots in the same figure indicates the influence of cooling rate on the predicted solute composition. For Al, the plot with the highest cooling rate is at the highest position, which means that the C^S_{Al} decreases as cooling rate decreases from 4×10^7 K/s to 1×10^6 K/s. For Fe and V, the plot with highest cooling rate is on the lowest position, which indicates that C^S_{Fe} and C^S_V increase as cooling rates decrease from 4×10^7 K/s to 1×10^6 K/s. It also should be noted

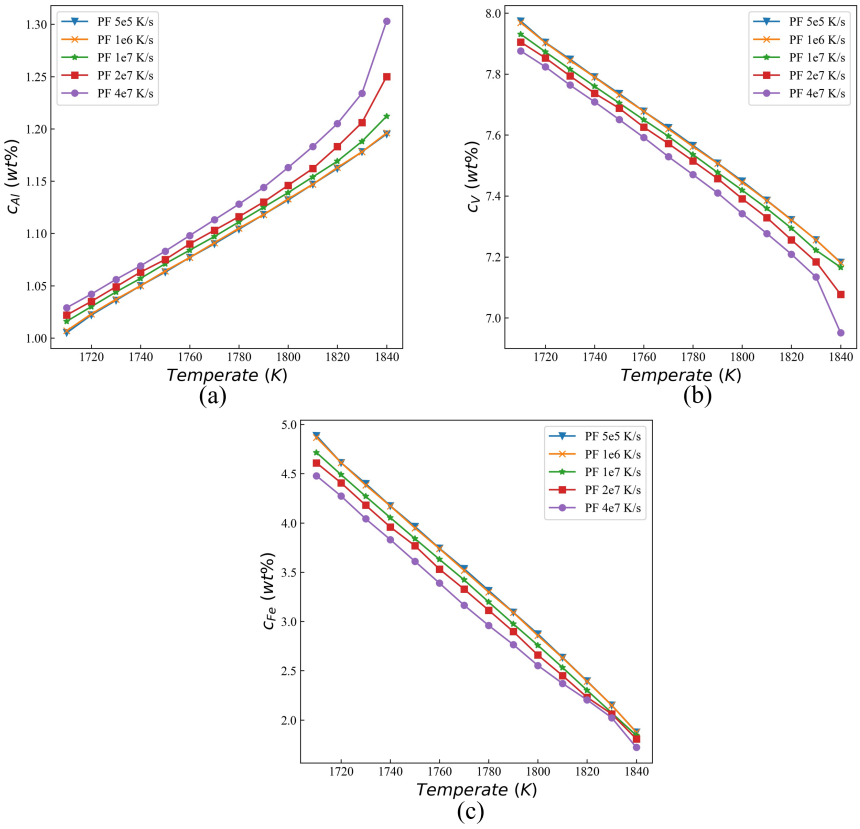

Figure 2.7: Evolution of solute in solid side of solid/liquid interface for (a) Al, (b) V and (c) Fe

that a further decrease of cooling rate from 1×10^6 K/s to 5×10^5 K/s showed only a very small influence on the solute concentration, as the two plots almost overlap. This phenomenon is caused by the only minimal diffusion in both liquid and solid side, the local composition at the solid/liquid interface and the multiple available tie-lines within a multi-component alloy upon which the equilibrium can be made. Initially, the local composition near the solid/liquid interface is largely influenced by the solid composition which contains a high content of Al and low content of V and Fe. This results a local composition that has more than 1% Al, but less than

8% V and 5%Fe. Then, because of this local composition, there is a different local equilibrium tie line at the solid/liquid interface. The solidification would occur at this local equilibrium states if the cooling rate was very large, even there is still a composition gradient in both solid and liquid side. However, when the simulated cooling rated is decreased, the local composition at the interface becomes closer and closer to the bulk composition. This results in a decrease in C^S_{Al} and an increase in C^S_{Fe} and C^S_V. Finally, at a cooling rate of 1×10^6 K/s, diffusion in the liquid and the solid was so fast (relatively) that no composition gradients were observed in the liquid nor in the solid at the solidus temperature. A further decrease to $5 \times 10^5 K/s$ thus could not influence the composition any more. In Fig. 2.5 (c), the same trend was observed for an isothermal solidification scenario, i.e. the C^S_{Fe} gradually increased as solidification occurred and finally converged to the value calculated by the CHT calculator.

The results from Fig. 2.7, showed that the solute concentration converged to the bulk value with decreasing cooling rate. Convergence was achieved at a cooling rate of 1×10^6 K/s and below. Fig. 2.8, compares the PF results at the lowest cooling rate, 5×10^5 K/s, against bot the Thermo-Calc calculations and the CHT calculator results. Fig. 2.9 plots the relative deviation between both Thermo-Calc and the CHT, and Thermo-Calc and PF see in Fig. 2.8.

Overall, a good agreement is achieved between the Thermo-Calc, CHT calculator, and the PF model results. However, there are some important deviations that should be discussed especially in the high temperature region. First, when comparing the results from Thermo-Calc and the CHT calculator, it can be seen that the CHT calculator always predicts a linear dependence of C^S_{eq} with temperature, while

Thermo-Calc predict a curved line for V. This difference caused a larger deviation at high temperature, with a relative deviation at T =1840 K of about 5%. The match is quite good for Fe, whereas the match is seen to be less good for Al. The reason for the poor match in Al is the fact that the three components depend on each other and because the equations are linear the error is reinforced at high tmperatures. Additionally, the scale for y-axis for Al is much smaller than for the y-axis of V or Fe, which accentuates the differences. Second, when comparing the PF results to both the Thermo-Calc and the CHT calculator results, it can be seen that the relative deviations are not all that large. For Al, the PF results are closest to Thermo-Calc, while for V the PF results are closest to the CHT calculator, and for Fe the PF results are closer to Thermo-calc at high temperature regions but closer to the CHT calculator results at low temperatures. This phenomenon is caused by a combined effect of CHT calculator and mass conservation. Ideally, the PF model would have converged to the CHT calculator results as cooling rate decreased. However, mass conservation is not considered when employing the CHT calculator. This causes deviations since it is not possible to maintain both the CHT calculator prediction and mass conservation when there is a large deviation between CHT and Thermo-Calc. For example, as shown in Fig. 2.9, the largest relative deviation between Thermo-Calc and CHT is 14% for Fe at $T = 1840$ K, and then 7% for Al at $T = 1840$ K. For V, whose PF results are closer to the CHT calculator, the relative deviation at T =1840 K is about 5%. As the mass conservation and CHT calculator can not be both satisfied, the mass conservation is still in effect, and the solid/liquid interface may have to seek another available tie line, which cause that the PF results is closer to Thermo-Calc for Al.

Overall, both the isothermal and continuous cooling PF simulations demonstrate

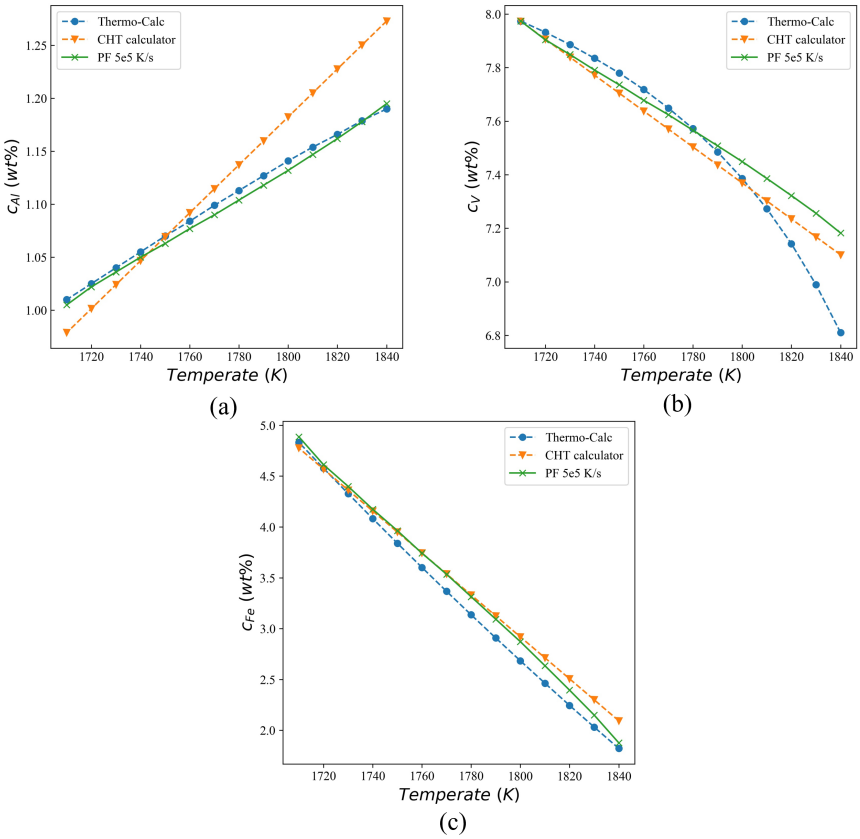

Figure 2.8: Variation of equilibrium solute concentration as a function of temperature for (a) Al, (b) V and (c) Fe predicted by Thermo-calc single equilibrium calculation, the phase equilibrium calculator and the phase field model

that the new CHT calculator is able to predict phase equilibrium with good accuracy via simplified thermodynamics both at a single temperature and over a range of temperatures, thus improving the efficiency of multi-component PF simulations. The deviations observed as compared to the TC calculations are thought to result from three origins. First, the extracted free energy data has been fit to a quadratic form of the free energy surface, Eq. 2.1, and deviations likely emerge during the fitting process. Second, these deviations may become enhanced when the fitted quadratic

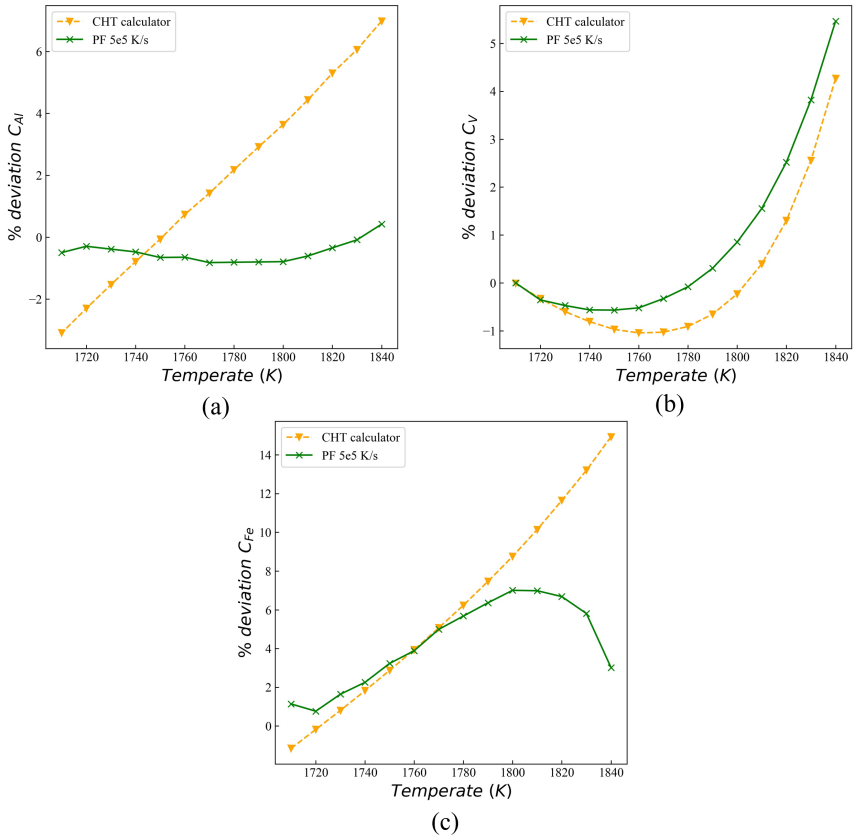

Figure 2.9: Variation of relative deviation between CHT calculator and Thermo-calc, and relative deviation between PF model and Thermo-Calc as a function of temperature for (a) Al, (b) V and (c) Fe

equation are used via convex hull calculations to fit to polynomials. Third, additional deviations may occur as a result of the PF implementation of the solid/liquid boundary evolution. Note that although the overall deviation between the CHT calculator, the TC calculations, and the 1D PF simulations are calculated, the origins of deviation are not distinguished from each other.

2.5 Conclusions

PF simulation of multi-component system is still computationally expensive, and the calculation of thermodynamic equilibrium is a main time-consuming part of the model. To solve this issue, a new method of phase equilibrium calculation for use in multi-component PF model is proposed in this paper. A parabolic representation for the free energy is adopted, and the convex hull method is used to solve the phase equilibrium at single temperatures, while the temperature dependence of the phase equilibrium is calculated via a set of concise linear equations. As compared to previous approached, the CHT method provides higher computational efficiency because the time-consuming phase equilibrium calculation is finished prior to the PF simulation, and concurrently higher computational accuracy, because the full local phase equilibrium is calculated. The solidification of Ti-Al-V-Fe alloy under isothermal and continuous cooling condition is taken as an example to show the feasibility and accuracy of the present approach. The accuracy of the approach is also discussed by comparing calculation results with commercial software Thermo-Calc. It is shown that this approach can achieve a high accuracy of equilibrium prediction at single and multiple temperatures, and this approach can be successfully applied on the multi-component phase field models.

Acknowledgements:ZL and AP acknowledge the funding provided by the Natural Sciences and Engineering Council of Canada, the Ontario Centre for Innovation, and Collins Aerospace in support of this research. MG acknowledges funding provided the Natural Resources Canada's Office of Energy Research and Development (OERD) and for the programming in the adaptive convex hull methodology development done by TJ Robotham at the CanmetMATERIALs laboratory.

References

[1] J. A. Warren and W. J. Boettinger, "Prediction of dendritic growth and microsegregation patterns in a binary alloy using the phase-field method," *Acta Metallurgica et Materialia*, vol. 43, no. 2, pp. 689–703, 1995.

[2] N. Provatas and K. Elder, *Phase-field methods in materials science and engineering*. John Wiley & Sons, 2011.

[3] B. Nestler, H. Garcke, and B. Stinner, "Multicomponent alloy solidification: phase-field modeling and simulations," *Physical Review E*, vol. 71, no. 4, p. 041609, 2005.

[4] S. G. Kim, "A phase-field model with antitrapping current for multicomponent alloys with arbitrary thermodynamic properties," *Acta Materialia*, vol. 55, no. 13, pp. 4391–4399, 2007.

[5] L. Nastac, "Solute redistribution, liquid/solid interface instability, and initial transient regions during the unidirectional solidification of ti-6-4 and ti-17 alloys," *CFD Modeling and Simulation in Materials Processing*, pp. 123–130, 2012.

[6] S. Sahoo and K. Chou, "Phase-field simulation of microstructure evolution of ti–6al–4v in electron beam additive manufacturing process," *Additive manufacturing*, vol. 9, pp. 14–24, 2016.

[7] K. Shampur, "A grand potential based multi-phase field model for alloy solidification," Master's thesis, McGill University, 2017.

[8] M. Greenwood, K. Shampur, N. Ofori-Opoku, T. Pinomaa, L. Wang, S. Gurevich, and N. Provatas, "Quantitative 3d phase field modelling of solidification

using next-generation adaptive mesh refinement," *Computational Materials Science*, vol. 142, pp. 153–171, 2018.

[9] N. Ofori-Opoku and N. Provatas, "A quantitative multi-phase field model of polycrystalline alloy solidification," *Acta Materialia*, vol. 58, no. 6, pp. 2155–2164, 2010.

[10] M. Plapp, "Unified derivation of phase-field models for alloy solidification from a grand-potential functional," *Physical Review E*, vol. 84, no. 3, p. 031601, 2011.

[11] N. Saunders and A. P. Miodownik, *CALPHAD (calculation of phase diagrams): a comprehensive guide*. Elsevier, 1998.

[12] X. Jiang, R. Zhang, C. Zhang, H. Yin, and X. Qu, "Fast prediction of the quasi phase equilibrium in phase field model for multicomponent alloys based on machine learning method," *Calphad*, vol. 66, p. 101644, 2019.

[13] A. L. Voskov, A. V. Dzuban, and A. I. Maksimov, "Ternapi program for the calculation of ternary phase diagrams with isolated miscibility gaps by the convex hull method," *Fluid Phase Equilibria*, vol. 388, pp. 50–58, 2015.

[14] W. J. Boettinger, J. A. Warren, C. Beckermann, and A. Karma, "Phase-field simulation of solidification," *Annual review of materials research*, vol. 32, no. 1, pp. 163–194, 2002.

[15] V. Fallah, M. Amoorezaei, N. Provatas, S. Corbin, and A. Khajepour, "Phase-field simulation of solidification morphology in laser powder deposition of ti–nb alloys," *Acta Materialia*, vol. 60, no. 4, pp. 1633–1646, 2012.

[16] B. Böttger, J. Eiken, and M. Apel, "Multi-ternary extrapolation scheme for efficient coupling of thermodynamic data to a multi-phase-field model," *Computational Materials Science*, vol. 108, pp. 283–292, 2015.

[17] H. Kobayashi, M. Ode, S. G. Kim, W. T. Kim, and T. Suzuki, "Phase-field model for solidification of ternary alloys coupled with thermodynamic database," *Scripta materialia*, vol. 48, no. 6, pp. 689–694, 2003.

[18] D. Lee, J. Choy, and J. Lee, "Computer generation of binary and ternary phase diagrams via a convex hull method," *Journal of phase equilibria*, vol. 13, no. 4, pp. 365–372, 1992.

[19] O. Ryll, S. Blagov, and H. Hasse, "Convex envelope method for the determination of fluid phase diagrams," *Fluid phase equilibria*, vol. 324, pp. 108–116, 2012.

[20] N. Perevoshchikova, B. Appolaire, J. Teixeira, E. Aeby-Gautier, and S. Denis, "A convex hull algorithm for a grid minimization of gibbs energy as initial step in equilibrium calculations in two-phase multicomponent alloys," *Computational materials science*, vol. 61, pp. 54–66, 2012.

[21] J. Eiken, B. Böttger, and I. Steinbach, "Multiphase-field approach for multicomponent alloys with extrapolation scheme for numerical application," *Physical review E*, vol. 73, no. 6, p. 066122, 2006.

[22] B. Echebarria, R. Folch, A. Karma, and M. Plapp, "Quantitative phase-field model of alloy solidification," *Physical review E*, vol. 70, no. 6, p. 061604, 2004.

[23] W. Xiao, S. Li, C. Wang, Y. Shi, J. Mazumder, H. Xing, and L. Song, "Multi-scale simulation of dendrite growth for direct energy deposition of nickel-based superalloys," *Materials & Design*, vol. 164, p. 107553, 2019.

[24] W. Sun, R. Yan, Y. Zhang, H. Dong, and T. Jing, "Gpu-accelerated three-dimensional large-scale simulation of dendrite growth for ti6al4v alloy based on multi-component phase-field model," *Computational Materials Science*, vol. 160, pp. 149–158, 2019.

[25] J. Heulens, B. Blanpain, and N. Moelans, "A phase field model for isothermal crystallization of oxide melts," *Acta Materialia*, vol. 59, no. 5, pp. 2156–2165, 2011.

[26] N. Moelans, "A quantitative and thermodynamically consistent phase-field interpolation function for multi-phase systems," *Acta Materialia*, vol. 59, no. 3, pp. 1077–1086, 2011.

[27] "http://www.qhull.org/,"

Chapter 3

A Quantitative Comparison between Pseudo-Binary and Multi-Component Phase Field Models

Complete Citation:

Li, Z., M. Greenwood, and A. B. Phillion. "A quantitative comparison between pseudo-binary and multi-component phase field models." Computational Materials Science 222 (2023): 112101.

A Quantitative Comparison between Pseudo-Binary and Multi-Component Phase Field Models

Z. Li[1], M. Greenwood[1,2], A.B. Phillion[1]

[1]*Department of Materials Science and Engineering, McMaster University, Hamilton, Canada*

[2]*Canmet MATERIALS, Natural Resources Canada, 183 Longwood Road south, Hamilton, ON, Canada*

Abstract: We present a benchmark analysis to compare three different phase-field models for multi-component alloy solidification. This analysis is carried out between, two pseudo-binary approaches and one multi-component approach, with respect to solidification of a quaternary iron-containing Ti alloy. The first pseudo-binary PF model is a common approach based on the model of Karma et al. [1], while the second pseudo-binary PF model and the multi-component model are implemented based on the grand potential model of Provatas et al. [2]. A very good similarity in microstructure is achieved between the three phase field models during both isothermal and directional solidification. The two grand potential models also show an excellent agreement in solute segregation predictions, and they are able to predict both positively segregating and negatively segregating elements. Finally, the influence of solidification rate on the microstructure is also studied, with the results matching analytical predictions. The results demonstrate the usefulness of different PF modelling approaches, and highlight cases where a full multi-component model is needed.

3.1 Introduction

The Phase Field (PF) method has become a popular approach in the recent decades to solve free-boundary problems [1, 3, 4, 5]. The PF method transcends the computationally complex issue of directly tracking topologically complex interfaces by using a continuous order parameter to represent different phases [6]. The order parameter will evolve automatically during the simulation along the direction that minimizes the free energy functional [6]. Benefiting from this advantage, the PF method has been applied to simulate the solid-state and solidification transformations in many metallic systems(e.g. [6, 7]).

Over the years, a number of well-accepted and quantitative PF models have been developed to simulate the solidification of binary alloys [1, 8]. However, simulating solidification of a multi-component alloy system via PF remains an open question as it requires either the use of a multi-component model or simplification to a binary system following the well-known pseudo-binary approximation [7, 9, 10] . Using a multi-component PF model, the diffusion and distribution of each species can be simulated independently of all others but with additional computational cost. Using the pseudo-binary approximation, an improved computational efficiency due to reduced number of composition fields is achieved, but the thermodynamic description of the alloy system is not so accurate.

In the pseudo-binary approximation, a single hypothetical solute component is created to represent the aggregate of all solute components in a multi-component alloy. To do this, the average solute content ($\bar{c}$, average liquidus and solidus slopes $\bar{m}_l$, $\bar{m}_s$, and average partition coefficient $\bar{k}$ of the hypothetical binary alloy are calculated by the weighted average-sum of all k, m_l and m_s values from the individual alloying

elements [10].

The pseudo-binary approximation has been applied to many different analytical and numerical models of solidification. For example, in 2000, Kermanpur et al. [9] simulated via Cellular Automata the grain structure of a turbine blade during the liquid metal cooling process. They used the pseudo-binary approach to represent a multi-component Ni-base super alloy as a binary system. In 2012, Nastac et al. [10] applied the pseudo-binary approximation within an analytical model to study the stability of the solid/liquid interface for different commercial Ti-alloys. In 2016, Sahoo [7] simulated microstructure evolution of a Ti alloy during additive manufacturing via a binary PF method, utilizing the pseudo-binary simplification to represent the ternary Ti-6Al-4V system as a hypothetical binary alloy.

Although a high computational efficiency can be achieved by utilizing the pseudo-binary approximation to simulate multi-component solidification via the binary PF model by Karma et al. [1, 11], there remains considerable limitations. First, the prediction of the solute redistribution of each component is identical, which makes it impossible to simultaneously predict solute distribution of positively segregating ($k < 1$) and negatively segregating ($k > 1$) components during solidification. Second, the approximation does not enable the simulation of an initially inhomogeneous distribution, such as the use of elemental powders during the Additive Manufacturing process that are being considered as an inexpensive substitute for pre-alloyed powders (e.g. [12]). These powders would create a nonuniform initial concentration field and an in-situ alloying process that requires access to multiple concentration fields.

To overcome these limitations, some multi-component PF models have been developed and applied to simulate the solidification of multi-component alloys. Sun et

al. [13] simulated via a multi-component PF model the dendrite growth of Ti-6Al-4V. However, this model ignored the interaction between the solute components and was simply an extension of Karma's binary model [1] to the multi-component case, as the partition coefficient k of each component was directly used. Eiken et al. [14] developed a multi-component multiphase-field model, and then applied it to study how additions of P and Sr affect the microstructure of hypoeutectic Al–Si alloys. In utilizing the quasi-equlibrium approach, this model achieved high accuracy but also had very high computational cost since the quasi-equilibrium calculation was carried out at every node point and for each time step of the model [15]. Kundin et al. [6] used another multi-component PF model to simulate the microstructure formation of a Nickel-based superalloy during rapid solidification process. In this work, the complicated multi-component phase equilibrium prediction was simplified to a single tie line that passed through the bulk composition. Although this approach significantly improved computational efficiency, it was done so at the cost of phase equilibrium accuracy.

The main challenge in performing multi-component PF simulations is to concurrently obtain high computational efficiency and accurate prediction of phase equilibrium. Recently, a grand potential PF model was developed by Provatas et al.[16, 17, 18], which offers a numerical efficiency advantage in large scale simulations. In this model, the chemical potential fields are tracked instead of the conventional concentration fields, which makes it possible to calculate the interfacial energy independent of the solute distribution across the interface. This allows the interface width to be scaled much larger than the thin interface limit , yet still within the limit of microstructure scales. The wider interface widths provides relatively high computational efficiency

for large-scale simulations. To solve the issue of accurate and efficient prediction of phase equilibrium in multi-component systems, Li et al. [17] proposed an approach based on the convex hull method. In [17], this new phase equilibrium prediction tool was applied to a 1-D grand potential PF model to simulate the solidification of a quaternary Ti-alloy. [16, 17, 18].

Most solidification PF models found in the literature have been compared against analytical models for validation. Karma et al. [4] compared a PF model for pure substances to dimensionless tip velocities calculated via Green functions. Kundin et al. [19] compared the secondary dendrite arms spacing predictions in tool steel made by a multi-component PF model to an analytical model by Rappaz et al. Lenart et al. [20] compared the primary dendrite arming spacing predictions in a Ni-base superalloy made by a binary PF model to analytical calculations. However, at present there has only been limited direct quantitative comparison between different PF approaches. In their recent study, Sun et al. [13] compared a pseudo-binary model PF with its multi-component equivalent but that work was qualitative in nature lacking a detailed quantitative analysis.

Although a number of new PF models have been developed to simulate the solidification of multi-component alloys (e.g. [6, 13, 14]), a benchmark of error analyses and uncertainty quantification is still lacking. Benchmark problems involve the comparison of models, algorithms and implementations; they provide a basis for evaluating different modelling approaches, algorithms, and numerical implementations. As an example, Jokisaari et al. [21] presented a benchmark case of comparing two different time adaptive numerical algorithms to simulate the spinodal decomposition and Ostwald ripening. Later [22], they extend the benchmark problem to dendritic growth,

and examined how different time integrators affect the model predictions of solidification of a single-component system.

In the present study, we present a benchmark analysis to compare three different phase field models for multi-component alloy solidification. This analysis is carried out between two pseudo-binary models and one multi-component model in the context of the solidification of a Ti-1Al-8V-5Fe (wt%) quaternary alloy. The first binary model (BM I) is the common pseudo-binary model based on Karma et al. [1], while the second binary model (BM II) and the multi-component PF model (MC) are two cases of the grand potential PF model by Provatas et al. [2]. The simulations are performed using the three PF models under two different scenarios: isothermal solidification and directional solidification. During the isothermal solidification, the grain morphology, solute redistribution and computational efficiency of the three models are compared. During the directional solidification, the predicted microstructure and the dendrite growth kinetics in the three models are studied. Finally, the predictions of primary and secondary dendrite arm spacing made by the three PF models for different solidification rates are investigated.

3.2 Description of the Phase Field models

3.2.1 Pseudo-Binary Phase Field Model 1

The PF model by Karma et al. [1] is derived for the solidification of dilute binary alloys in the thin interface limit [5]. An order parameter ϕ is defined in this model to represent the solid ($\phi = 1$) and liquid ($\phi = -1$) phases. The evolution of the parameter ϕ is carried out in order to minimize the free energy of the system [23].

Additionally, the evolution of the order parameter is also influenced by the diffusion of solute. This binary PF model, denoted BM I, can be expressed as

$$\tau(\vec{n})\frac{\partial\phi}{\partial t} = \vec{\nabla}\cdot W_\phi(\vec{n})\vec{\nabla}\phi + \phi - \phi^3 - \lambda_o(1-\phi^2)^2(\frac{1}{1-k}(e^u-1) + \frac{T-T_0}{\Delta T_f}), \text{and} \quad (3.1)$$

$$\frac{\partial c}{\partial t} = \nabla\cdot(D_L Q(\phi)c\nabla u) + \nabla\cdot(W_\phi a(\phi)(1-k)c_0^l e^u \frac{\partial\phi}{\partial t}\frac{\nabla\phi}{|\nabla\phi|}), \quad (3.2)$$

where

$$u = \ln\frac{2c}{c_0^l[1+k-(1-k)\phi]}, \quad (3.3)$$

$$Q(\phi) = \frac{1-\phi}{1+k-(1-k)\phi}, \quad (3.4)$$

$$\lambda_o = \frac{a_1 W}{d_0}, \quad (3.5)$$

$$d_0 = \frac{\Gamma}{\Delta T_f}, \quad (3.6)$$

and $\vec{n} \equiv \frac{\vec{\nabla}\phi}{|\vec{\nabla}\phi|}$ is the normal direction to the interface, k(-) is the partition coefficient, T(K) is the local temperature, T_0(K) is the reference temperature, d_0(m) is the capillary length, Γ(K·m) is the Gibbs-Thompson coefficient, ΔT_f(K) is the freezing range [23], λ_o(-) is the coupling coefficient, c(-) is the local solute composition, c_0^l(-) is the equilibrium solute concentration in liquid phase at T_0, D_L($\mathrm{m^2 s^{-1}}$) is the liquid

diffusivity, $\tau(\vec{n})(-) = \tau_0 a_s(\vec{n})^2$ is the relaxation time, $a(\phi) = \sqrt{2}/2$, a_1=0.8839 is a constant [1], and $a_s(\vec{n})$ represents the 2D four-fold anisotropy. This last term is calculated as

$$a_s(\vec{n}) = 1 - 3\epsilon_4 + 4\epsilon_4 \frac{(\partial_x \phi)^4 + (\partial_y \phi)^4}{|\vec{\nabla}\phi|^4}, \tag{3.7}$$

where ϵ_4 is a parameter characterized the anisotropy strength of the material, and $W_\phi(\vec{n}) = W_0 a_s(\vec{n})$ sets the interface width [5].

3.2.2 Pseudo-Binary Phase-Field Model 2 and Multi-Component Model

The multi-order parameter PF model by Provatas et al. [2, 16, 18] is derived based on a grand potential ensemble for the solidification of multi-component and multi-phase alloys. Two special cases are the binary alloy PF model with quadratic free energy and the two-phase multi-component alloy. The quadratic function is a well-accepted form to describe the free energy of massive alloy phases [24, 25, 26].

Provatas' binary-alloy PF model, denoted BM II, begins with a quadratic free energy description of the solid and liquid phases,

$$F^\theta = \frac{A^\theta}{2}(c - c^\theta_{min})^2 + B^\theta, \tag{3.8}$$

where F^θ represents the free energy of phase θ as a function of composition c and fitting parameters A^θ, c^θ_{min}, and B^θ. To determine A^θ, c^θ_{min}, and B^θ, a data set $\{c, F\}$ that contains a massive number of concentration-free energy data points is extracted from a thermodynamic database (e.g. Thermo-Calc), and then fit via a least square

method. The fitting parameters will also be used in the phase field equations.

In this model, the evolution of the order parameter ϕ and chemical potential μ are then expressed based on the free energy relaxation principle as shown below,

$$\tau(\vec{n})\frac{\partial\phi}{\partial t} = \vec{\nabla}\cdot W_\phi(\vec{n})\vec{\nabla}\phi + \phi - \phi^3 - \lambda_o(1-\phi^2)^2 U(1+\frac{1-k^{eff}}{2}U), \text{and} \tag{3.9}$$

$$\chi(\phi)\frac{\partial\mu}{\partial t} = \nabla\cdot[D_L q(\phi)\nabla\mu + W_\phi a(\phi)\Delta c_{eq}\{1 + (1-k^{eff}U)\}\frac{\partial\phi}{\partial t}\frac{\nabla\phi}{|\nabla\phi|})] + \frac{1}{2}\Delta c_{eq}\{1+(1-k^{eff}U)\}\frac{\partial\phi}{\partial t} \tag{3.10}$$

where a new supersaturation field U is defined,

$$U \equiv \frac{\chi^L_{eq}}{\Delta c_{eq}}(\mu - \mu_{eq}), \tag{3.11}$$

μ_{eq} is the equilibrium chemical potential,

$$\mu_{eq} = \frac{\Delta c}{\chi^L_{eq}}(\sqrt{1+2\frac{\chi^L_{eq}(1-k^{eff})}{\Delta c}\frac{\Delta B}{\Delta c}} - 1) \tag{3.12}$$

and where

$$\Delta c \equiv c^L_{min} - c^S_{min}, \tag{3.13}$$

$$\Delta B \equiv B^L - B^S, \tag{3.14}$$

$$\chi^L_{eq} \equiv 1/A^L, \tag{3.15}$$

$$\chi^S_{eq} \equiv 1/A^S, \tag{3.16}$$

$$k^{eff} \equiv \chi^S_{eq}/\chi^L_{eq}, \tag{3.17}$$

$$\Delta c_{eq} = \Delta c + \chi^L_{eq}(1 - k^{eff})\mu_{eq}, \tag{3.18}$$

$$\chi(\phi) = \chi^L_{eq}[1 - (1 - k^{eff})\frac{1+\phi}{2}], \text{and} \tag{3.19}$$

$$q(\phi) = \chi(\phi)\frac{1-\phi}{2}. \tag{3.20}$$

Provatas' multi-component PF model [2, 16, 17, 18], denoted MC, also begins with a quadratic description of the free energy of the solid and liquid phases,

$$F^\theta\left(c_1, c_2, ...c_n - 1\right) = \frac{1}{2}\sum_{i=1}^{n-1}\sum_{j=1}^{n-1} A^\theta_{ij}\left(c_i - \bar{c}^\theta_i\right)\left(c_j - \bar{c}^\theta_j\right) + \sum_{j=1}^{n-1} B^\theta_j\left(c_j - \bar{c}^\theta_j\right) + D^\theta, \tag{3.21}$$

where c_i and c_j are the concentration of component i and j, and the fitting parameters A^θ_{ij}, $\bar{c}^\theta_i$, B^θ_j and D^θ are determined through the aforementioned least square fitting process.

Furthermore, the evolution of the order parameter ϕ and chemical potential μ can be expressed based on the free energy relaxation principle in a similar way to 3.9

and 3.10 but in matrix format,

$$\tau(\vec{n})\frac{\partial\phi}{\partial t} = \vec{\nabla}\cdot W_{\phi}(\vec{n})\vec{\nabla}\phi + \phi - \phi^3 - (1-\phi^2)^2\left(\frac{(I-[K])^T}{2}\vec{U} + \hat{n}_c\right)^T [\lambda]\vec{U}, \quad (3.22)$$

and

$$[\chi]\frac{\partial\vec{\mu}}{\partial t} = \nabla\left[[M]\nabla\vec{\mu} + Wa(\phi)\,|\Delta\vec{c}_{eq}|\{\hat{n}_c + (I-[K])^T\vec{U}\}\frac{\partial\phi}{\partial t}\frac{\nabla\phi}{|\nabla\phi|}\right] + \frac{1}{2}|\Delta\vec{c}_{eq}|\{\hat{n}_c + (I-[K])^T\vec{U}\}\frac{\partial\phi}{\partial t}, \quad (3.23)$$

where $\vec{\mu}$ is a vector representing the chemical potentials of each solute component μ_i, I is the identity matrix, and $[\chi^{\theta}]$ is the inverse matrix of $[A^{\theta}]$, $[A^{\theta}]$ is a matrix that composed of parameters A^{θ}_{ij}. Please note that vector and matrix notation are used in the present paper to represent within the numerical algorithm a vertical column and multiple columns of numbers respectively, while the square brackets are used to represent the matrix form of the parameters, and where

$$\left[\chi^{\theta}\right]^{-1}_{ij} = A^{\theta}_{ij}, \quad (3.24)$$

$$\vec{U} = \frac{\left[\chi^{L}\right]}{|\Delta\vec{c}_{eq}|}\left(\vec{\mu} - \vec{\mu}_{eq}\right), \quad (3.25)$$

$$\Delta\vec{c}_{eq} = \vec{c}^{L}_{eq} - \vec{c}^{S}_{eq}, \quad (3.26)$$

$$\hat{n}_c = \frac{\Delta\vec{c}_{eq}}{|\Delta\vec{c}_{eq}|}, \tag{3.27}$$

$$[K] = \left[\chi^L\right]^{-1}\left[\chi^S\right], \tag{3.28}$$

$$[\lambda] = \lambda_o \frac{|\Delta\vec{c}_{eq}|^2}{|\Delta\vec{c}_{eq,i}|^2}[\chi^L]^{-1}\chi^L_{ii}, \tag{3.29}$$

$$d_{0,i} = \frac{2\sigma_{SL}}{|\Delta\vec{c}_{eq,i}|^2}\chi_{ii} \tag{3.30}$$

$$[\chi] = \left[\chi^L\right]\{I - (I - [K])\, h(\phi)\}, \tag{3.31}$$

and

$$[M] = q(\phi)\left[D^S\right]\left[\chi^S\right] + (1 - q(\phi))\left[D^L\right]\left[\chi^L\right]. \tag{3.32}$$

In this set of equations, σ_{SL} is the solid/liquid interface energy, $h(\phi)$ and $q(\phi)$ are interpolation equations commonly used in PF models, $\left[D^\theta\right]$ is the diffusion coefficient matrix that is related to the physical properties of the alloy system, and matrices $[K]$ and $\left[\chi^\theta\right]$ are related to the free energy surface given in Eq. 2.1.

It should also be noted that the capillary length d_0 is calculated by a different method in Multi-component PF models. As each solute element has its own diffusion field, several capillary lengths are possible. In this MC model, we first calculate the capillary length for each component via Eq. 3.30. Then, the component with smallest capillary length is identified and used as the reference component. Its capillary length is chosen as the capillary length for the simulation.

Note that in both BM II and MC, the terms $\vec{\mu}_{eq}$, $\vec{c}^{L}_{eq}$ and $\vec{c}^{S}_{eq}$ vary as a function of local temperature T. Please refer to our previous study, [17] for the calculation methodology. Note also that the calculation of surface anisotropy $a_s(\vec{n})$, interface width $W_(\phi)(\vec{n})$ and relaxation time $\tau(\vec{n})$ in BM II and MC are the same as in BM I.

3.3 Numerical Implementation

The three PF models will be applied to study the solidification of a quaternary Ti-1Al-8V-5Fe (wt.%) alloy. As the present paper focuses on the benchmark of different models, the implementation and algorithms of the three models are kept the same. For the three models, the equations were solved using a bespoke C++ code via the finite volume method on an adaptive mesh. To improve the computational efficiency, a next generation dynamic adaptive mesh refinement algorithm developed by Greenwood et al. [16] was adopted. The thermodynamic free energy data of the Ti-alloy was extracted from the Thermo-Calc$^{\text{TM}}$ TCTI 2 database. The temperature-dependent phase equilibrium for the Ti-185 alloy was calculated using a convex hull -based tool introduced in our previous study [17]. A bespoke Python code utilizing the Least Square fittings was developed to fit the extracted free energy data to Eq. 3.8 and Eq. 2.1. Please refer to [17] for additional details.

Utilizing BM I and BM II to simulate solidification of the Ti-185 alloy requires implementation of a pseudo-binary approach to translate the multi-component alloy into a binary equivalent. For BM I, the pseudo-binary equivalent is expressed by simply replacing the terms c, m_l and k in Eq.2.2 and 3.2 with their average equivalent, i.e. $\bar{c}$, $\bar{m}_l$, and $\bar{k}$ as shown below,

$$\bar{c} = \sum_{i=1}^{N} c_i, \tag{3.33}$$

$$\bar{m}_l = \frac{\sum_{i=1}^{N} m_{l,i} c_i}{\bar{c}}, \text{and} \tag{3.34}$$

$$\bar{k} = \frac{\sum_{i=1}^{N} m_{l,i} c_i k_i}{\bar{m}_l \bar{c}}. \tag{3.35}$$

The required liquidus and solidus temperatures were extracted from Thermo-Calc for the quaternary Ti-185 alloy. Further, the pseudo-binary single concentration field variable, c_{all} was expressed as

$$c_{Al} = \frac{1}{8} c_V = \frac{1}{5} c_{Fe} = \frac{1}{14} c_{all}. \tag{3.36}$$

For BM II, the average equivalents $\bar{c}$, $\bar{m}_l$, and $\bar{k}$ cannot be used to create the pseudo-binary system because Provatas' grand potential model uses directly the free energy curves of the liquid and solid phases in the form of Eq. 3.8. Further complicating matters, the two free energy curves of a binary alloy system become hyper-surfaces in a quaternary alloy system.

The approach taken to create the pseudo-binary equivalent is to assume that the free energy hyper-surfaces of the quaternary alloy can be represented by two free energy curves having the same tie lie, i.e. a tie-line that maintains the bulk Ti-185 composition. This approach is implemented in a four-step process prior to carrying out the PF simulation. First, the CALPHAD method is applied to determine the equilibrium concentrations of each component ($c^L_{Al,eq}$, $c^L_{V,eq}$, $c^L_{Fe,eq}$, $c^S_{Al,eq}$, $c^S_{V,eq}$ and $c^S_{V,eq}$)

in the liquid and solid phases at a temperature interest. Second, in the parameter space surrounding the equilibrium concentrations, the corresponding $\{F^S, F^L\}$ values are extracted from Thermo-Calc for a massive set of composition value: $\{c_{Al}, c_V, c_{Fe}\}$. The values of c_{Al}, c_V, and c_{Fe} are not arbitrary but instead chosen given the constraint that the tie-line passes through the bulk Ti-185 composition. This can be expressed as a linear relationship between the concentration of the three components,

$$\frac{c_V - c^L_{V,eq}}{c_{Al} - c^L_{Al,eq}} = \frac{c^S_{V,eq} - c^L_{V,eq}}{c^S_{Al,eq} - c^L_{Al,eq}} \tag{3.37}$$

$$\frac{c_{Fe} - c^L_{Fe,eq}}{c_{Al} - c^L_{Al,eq}} = \frac{c^S_{Fe,eq} - c^L_{Fe,eq}}{c^S_{Al,eq} - c^L_{Al,eq}} \tag{3.38}$$

Third, the pseudo-binary equivalent composition, c_{all} is determined as the sum of the three solute element compositions for each set of $\{c_{Al}, c_V, c_{Fe}\}$. Fourth, the least square methods is applied to the dataset $\{c_{all}, F^S, F^L\}$ to fit the free energy of liquid and solid phases to the form of Eq.3.8 that is needed to carry out the BM II PF simulation. Note the four-step approach approach calculates the phase equilibrium at a single temperature. Please refer to [17] for the details of the calculation methodology used to incorporate temperature dependence.

The relevant PF simulation parameters and thermo-physical properties are listed in Table 3.1. Note that the domain size and interface widths for all three models were set to the same values in order to enable direct comparisons. It need to be noted that the W/d_0 ratio in the present is about 15, and in the model by echebarria et al. [1], they found that the tip radius, tip undercooling and tip solute concentration value are all converged for W/d_0 ratio up to 50.

Table 3.1: Simulation parameters and thermo-physical properties of Ti-185 alloy [7][13]

Thermo-physical data	Value
k	0.4132
T_L (K)	1848
T_S (K)	1705
Γ (K·m)	2.0E-7
σ_{SL} (J/m^2)	0.046
ϵ_4	0.05
D_L (m^{2}s^{-1})	9.5E-9
D_S (m^{2}s^{-1})	5.0E-13
Model Inputs	**Value**
$W_0(\times 10^{-9}$ m)	15
Mesh spacing (dx)	0.8
Time spacing ($\times 10^{-9}$ s)	2.85
grid points (Section 4.1)	2048×2048
grid points (Section 4.2)	2048×8192
domain size(μm)(Section 4.1)	24.6×24.6
domain size(μm)(Section 4.2)	24.6×98.3

3.4 Results and Discussions

The benchmark problems of the three different models are evaluated under two scenarios: isothermal solidification and directional solidification. Under the isothermal solidification case, we choose for comparison as qualitative metric the microstructural snapshots, and as quantitative metric the dendrite tip traveling distance, solute distribution and computational efficiency. Under the directional solidification condition, the microstructural snapshots, dendrite tip velocity, dendrite tip temperature and the volume fraction of the solid phase were chosen as the metrics. The choice of metric was based on the theory presented in Refs. [22], i.e. qualities that were relatively easy to compare and yet highly sensitive to model choice.

3.4.1 Isothermal solidification of a multi-component alloy

The isothermal solidification of the Ti-185 alloy at $1805K$ is simulated utilizing the three PF models.

Fig. 3.1 shows a snapshot of the grain morphology simulated by the three PF simulations at the same solidification time. Considering the morphological symmetry of the equiaxed grains, Fig. 3.1 is fabricated by combining half of the grain from MC simulation and quarter of the grains from BM I and BM II. As can be seen, the microstructure simulated from the three PF models shows good similarity, while the main difference is the grain size. The grain simulated from the BM I model is larger, while the grain size of BM II and MC simulations is smaller. There may be multiple explanations about the grain size difference, and a further analysis is made in Fig. 3.2 to explore it.

Fig. 3.2 shows a comparison of tip traveling distance as a function of time between the three PF models: solid line (for MC), dashed line (for BM I) and dotted line(for BM II). The tip traveling distances are calculated by subtracting the initial tip position at time $t = 0$ from the tip position at time t. As can be seen, for all three models, after a short transient, there is clear linear relationship between the tip traveling distance and the solidification time for all three simulations. This means that the dendrite tips very quickly reach the steady-state growth stage, as expected. Green functions calculations and other PF simulations [4, 6, 27] have also shown that the dendrite growth tip velocity is a constant at steady state, and the dimensionless tip velocity is only a function of bulk undercooling and the anisotropy strength $\epsilon 4$.

Fig. 3.2 also shows that, as the slopes for each curve are different, each model has a different tip velocity. Specifically, the steady-state tip velocity for the BM I model is

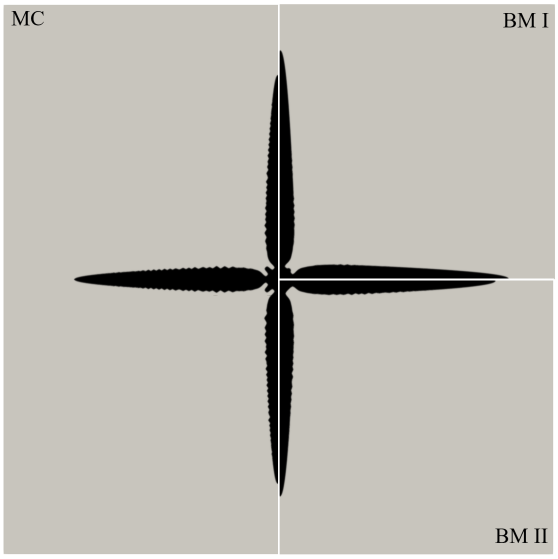

Figure 3.1: A comparison of grain morphology of isothermal solidification of Ti-185 alloy at $T = 1805$ K from three different phase field models at the same time $t = 0.15$ ms. Where, MC means Multi-component model, BM I represents a pseudo-binary model based on the model by Karma et al, BM II is the binary model based on the model by Provatas et al

about 20% greater than than the MC model for the same simulation conditions, with the BM II model falling in between. Initially we had expected all three models to show a very similar tip velocity. However, this benchmarking analysis makes it clear that the free energy least square fitting process, which influences the calculation of the equilibrium concentrations and thus affects the calculation of the bulk undercooling, thus has an important effect on dendrite growth. In the case of BM I, using the effective partition coefficient shows an accelerated dendrite growth as compared the grand potential approach. Furthermore, as was seen in Fig. 3.1 the dendrite growth simulated by the MC model contains more side branches as compared to the BM II model. The trend to form more side branches in the MC model may result from the additional degrees of freedom available for phase equilibrium or tie line selection in multi-component systems. This would also slow down dendrite growth.

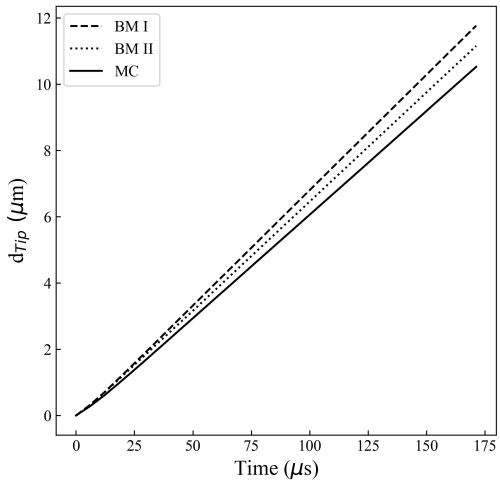

Figure 3.2: Variation of tip traveling distance with time from three phase field models for the isothermal solidification of Ti-185 alloy

One main advantage of the MC PF model is the ability to individually simulate the

diffusion of each components, while the two binary PF models take the components as a combined ensemble to diffuse. Fig. 3.3 shows a detailed comparison of solute distribution along two specific lines across the solid/liquid interface from the three PF models. Fig. 3.3 (a) shows the positions of the two selected lines (Labeled as L1 and L2). The solute distributions of Al, V and Fe along the two lines are shown in Fig. 3.3 (b), (c), and (d). There is only one concentration field in the BM I and BM II simulations, thus the concentration of each solute components is calculated using linear translations of the results from BM PF simulations. Eq. 3.36 is used to calculate the solute content in BM I, while the individual solute content in BM II is calculated by Eqs. 3.37 and 3.38.

As can be seen from Fig. 3.3 (b), a negative segregation of Al is predicted by BM II and MC models, which agrees with the Thermo-Calc single equilibrium calculations and our previous 1-D PF simulation [17]. However, a positive segregation of Al is predicted by BM I, as a fixed partition coefficient k is defined in this model for all solute components. Owing to the same k in BM I for all solute components, BM I tends to overestimate the solute segregation of V when compared with other two models as illustrated in Fig. 3.3 (c), while the solute segregation of Fe is underestimated as shown in Fig. 3.3 (d). An excellent agreement of solute segregation is observed between BM II and MC simulations, as these two model are derived from the same grand potential ensemble. Additionally, the tie line pass through the bulk composition of the Ti-185 alloy is maintained in the BM II models, while the free energy minimization of MC PF model also falls on the same tie line, thus an excellent agreement is obtained. However, some minor differences are also observed in interface regions, which result from the linear simplification in the BM II model. There

is a similar solute segregation trend along the lines L1 and L2, while the difference is a higher content of Fe and V, a lower content of Al is distributed in the front of solid/liquid interface along L2. The differences in solute content along L1 and L2 may be caused by two reasons. First, the solid/liquid interface perpendicular to L2 is nearly a plane, which means there is only one direction for solute to diffuse. As for the L1, which is along the parabolic dendrite tips, there are more directions for solutes diffusion. Second, the different curvatures of solid/liquid interfaces along L1 and L2 also influence the equilibrium calculations.

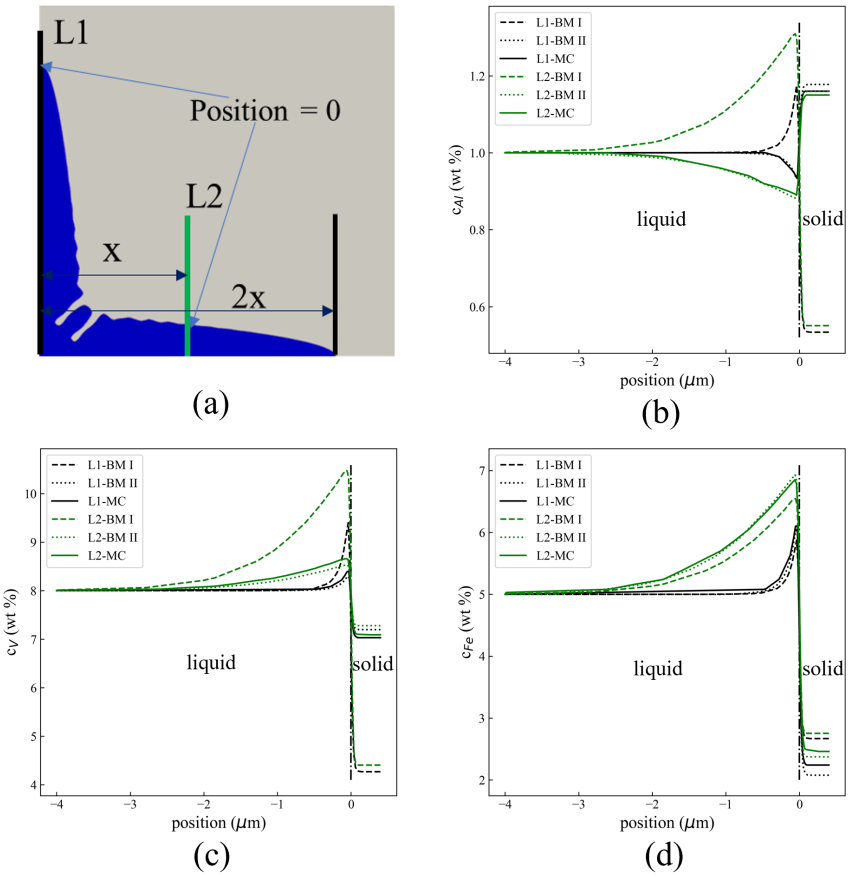

Figure 3.3: Distribution of solute components (b) Al, (c) V and (d) Fe across the solid/liquid interface along lines L1 and L2 indicated in (a), during isothermal solidification of Ti185 alloy at 1805 K, where *position* = 0 is the solid/liquid interface

Fig. 3.4 shows the ratio of computational CPU time between the MC model and the two BM models, as well as the ratio between BM I and BM II, as a function of iterations to compare the computational efficiency between the three models for the isothermal solidification simulation. These simulations were performed under the condition defined in Table 2.1. As can be seen, initially the two BM models run much faster (up to 8x) than the MC model. After this initial transient of about

9000 iterations the ratio gradually decreases to final values of 3.5x and 5.9x faster computation time for the BM I and BM II model, respectively. As for the two BM models, it it seen that BM II runs about 2x faster than the BM I model, using the same numerical methodology. The MC model required 275 minutes to complete 50,000 iterations, while the runtime for the BM I and BM II models was 79 and 47 minutes respectively. It is logical that it takes longer to run the MC models since two more concentration fields need to be evolved, as well as the extra time-consuming multi-component phase equilibrium calculations. It is less clear why it takes longer to run the BM I model as compared to the BM II model. One possible explanation is the difference in tip velocity between BM I and BM II. It well known that phase field models run slower with faster dendrite growth [16]. However, this does not fully explain the 2x increase in speed.

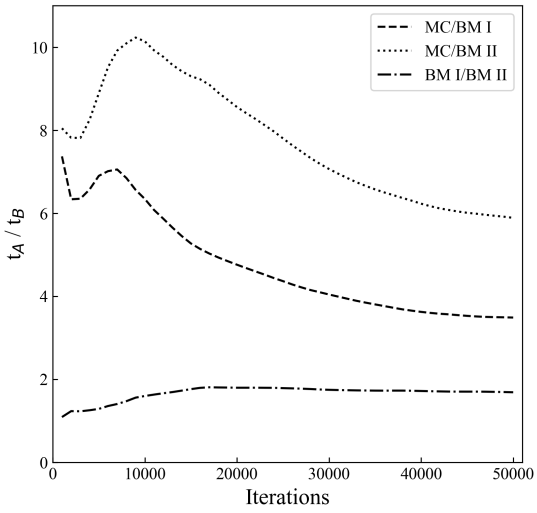

Figure 3.4: The ratio of computational CPU time between the multi-component model and the pseudo-binary models as a function of iterations

3.4.2 Directional solidification of a multi-component alloy

In this section, directional solidification of the Ti-185 alloy is simulated using the three PF models. In this simulation, a frozen temperature approximation is adopted to update the temperature field. This approximation is reasonable because heat conduction is much faster than mass transfer [1, 5]. A one-dimensional temperature gradient of magnitude G is defined along the z-axis. The local temperature T is then calculated based on the solidification speed v_p, simulation time t, initial temperature T_0 and coordinate z [1]:

$$T(z) = T_0 + G(z - v_p t) \tag{3.39}$$

3.4.2.1 Comparison between the three models under the same thermal conditions

Fig. 3.5 shows a snapshot of the concentration profile of Fe from the three 2-D PF models at the same solidification time, under the same processing conditions. In this simulation, the temperature gradient G is 2×10^6 K/m, while the solidification speed v_p is 0.05 m/s. A small nuclei is placed at the center of the bottom where $T_0 = 1820$ K at the beginning, thus the solidification proceeds from the bottom to the top.

In Fig. 3.5, the solute contents of Fe in the two binary models are calculated by the same approach as discussed in Section.3.4.1. The segregation of Fe in the liquid phase is predicted by the three models, while the extent of this segregation is different in the three models. The segregation of Fe from the BM I model tends to be weaker, which corresponds to a lighter red in liquid phase and lighter blue in solid phase. The trend of underestimating the segregation of Fe in BM I agrees with

the isothermal solidification, as illustrated in Fig. 3.3 (d). As for dendrite geometry, a similar dendritic growth is simulated by the three models, where multiple parallel primary dendrites with abundant side branches form during the simulations. Further, the dendrite tip is almost at the same height at the same solidification time, and a further analysis of the tip velocity is given in Fig. 3.6.

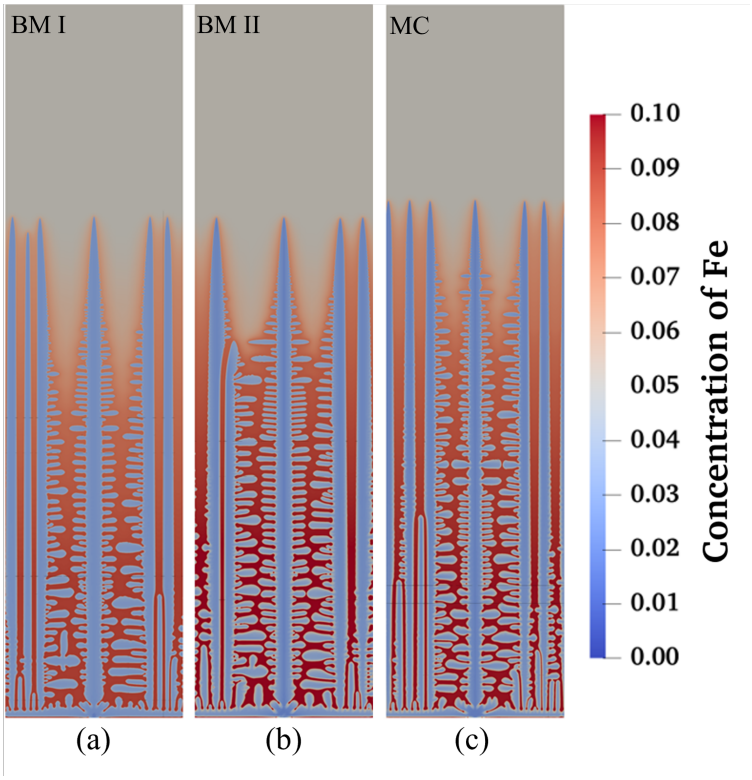

Figure 3.5: A comparison of concentration profiles of Fe during directional solidification of Ti-185 alloy from (a) BM I, (b) BM II and (c) MC, at the same time t =1.56 ms

Fig. 3.6 shows a variation in dendrite tip velocity as a function of solidification time. As can be seen, there is an excellent agreement between the three models. During the simulations, the tip velocity starts from a small value and continuously increases to a value which is larger than the pulling velocity v_p, then it drops to

the v_p and oscillates around it. The variation in tip velocity v_{tip} is related to the tip temperatures or tip undercoolings. The nuclei is initially placed on a low undercooled region, and the dendrite grows slowly compared to the pulling velocity v_p. Thus, the tip temperature will decrease and the tip will grow faster and faster. Finally, the dendrite tip finds a temperature where it can grow at the preset pulling velocity v_p, and steady-state dendrite growth is reached.

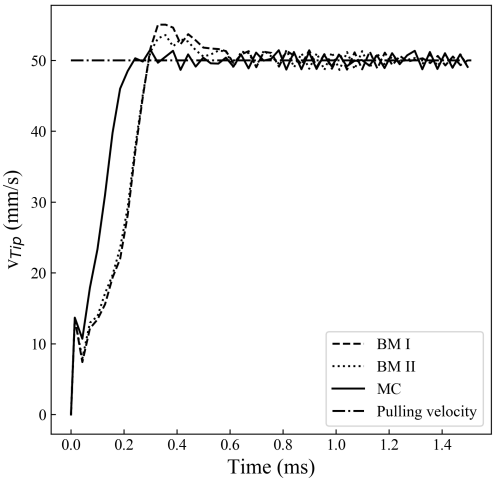

Figure 3.6: Variations of dendritic tip velocity as a function of time from three PF models

Fig. 3.7 shows a comprehensive comparison between the PF simulations and other analytical analysis. In Fig. 3.7, the variation in solid volume fraction simulated by PF models with height is shown. The three black lines in Fig. 3.7 represent the results from the BM I(dashed line), BM II (dotted line) and MC (solid line). These plots were made following a two-step procedure. First, a line average method which applies only on the width of the simulation domains is adopted on the volume of the solid phase, and the resulted plots can be interpreted as the 1-D distribution of

solid fraction along the height direction. Then, the three black lines in Fig. 3.7 are obtained by applying a centered moving average to the former plots. As can be seen, there is a non-monotonic decrease in solid fraction from the bottom of the domain to the dendrite tip. The phase field results are not smooth lines, because abundant side branches form during the simulation as shown in Fig. 3.5. While the three PF models show a good agreement in the whole domain, there are still minor differences. The MC model predicts a higher dendrite tip positions when compared to the two binary models, which may result from different capillary lengths adopted. Another explanation could be the additional degrees of freedom available in multi-component system, which results from multiple possible tie lines at one single temperature. The BM I model tends to predict a smaller solid fraction near the bottom part of the domain, while the BM II and MC model show an excellent agreement. Considering the same grand potential derivation approach in BM II and MC, and nearly the same thermodynamic phase equilibrium is utilized in the PF simulations, it is reasonable to reach such an agreement.

Also shown in Fig. 3.7 is the analytical calculated solid fraction given by equilibrium solidification and Scheil calculations. The equilibrium solidification curve is drawn based on a series of single equilibrium calculations using the commercial software Thermo-Calc. The Scheil simulation is also completed on Thermo-Calc using the classic Scheil model. Because of the infinity solute diffusion assumption ($D_L = D_S = \infty$) in the equilibrium solidification scenario, it is reasonable that the equilibrium solidification predicts the highest solid fraction in the whole domain. The Scheil simulation predicts a similar curve shapes as the PF simulations, but the Scheil simulations predict a higher position of the mushy zone-liquid boundary. There are

several reasons for the different mushy-liquid boundary. First, the Scheil simulation is designed for 1-D solidification, and thus curvature effects are not considered [1]. To include the curvature effect in the Scheil simulation, a green line is added to Fig. 3.7, where the tip radius in MC model is used for the curvature modification. Second, in the Scheil simulation, an assumption of infinity fast solute diffusion in liquid phase ($D_L = \infty$) is assumed, which cannot account for the diffusion-controlled solidification kinetics [28]. Third, the solute composition in the PF models may exceed the bulk composition, as the solute is continuously transported by diffusion through mushy zone towards the dendrite tip, which also delays the solidification [28]. Finally, some extent of undercooling is needed to maintain a preset solidification velocity in a steady-state directional solidification simulation.

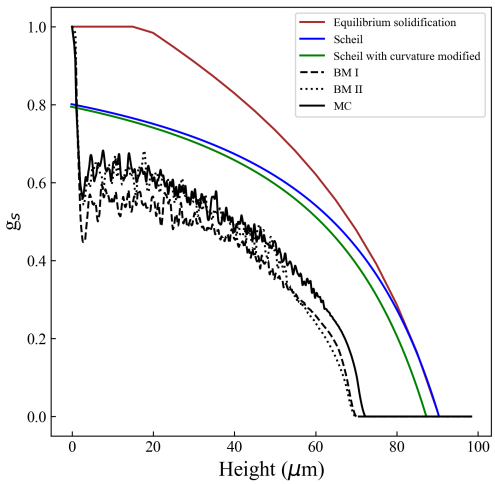

Figure 3.7: A comparison of solid fraction simulated by the three PF models and Scheil simulation as a function of height, or temperature (Considering the fixed temperature gradient in height direction)

3.4.2.2 Influence of thermal conditions on microstructure

The PF models are widely used to predict the influence of process parameters on microstructure in directional solidification or additive manufacturing processes [7, 20]. The influence of solidification rate on microstructure is explored in this section. Fig. 3.8 shows a snapshot of the 2-D PF simulations of Ti-185 directional solidification under different solidification rates. In these simulations, four different pulling velocities v_p, are applied (25, 50, 75 and 100 mm/s), all under the same temperature gradient $G = 2 \times 10^6$ K/m, for BM I, BM II, and MC. The results from BM I are shown in Fig. 3.8 for all four values of v_p. By making these plots at different solidification times (3.40, 1.70, 1.13 and 0.85 ms) the images all show the microstructure at the same temperature profile. As can be seen, as the pulling velocity increases from the Fig. 3.8 (a) to (d), the dendrite tip height decreases. Additionally, there also tends to be more primary and secondary dendrites with increasing pulling velocity.

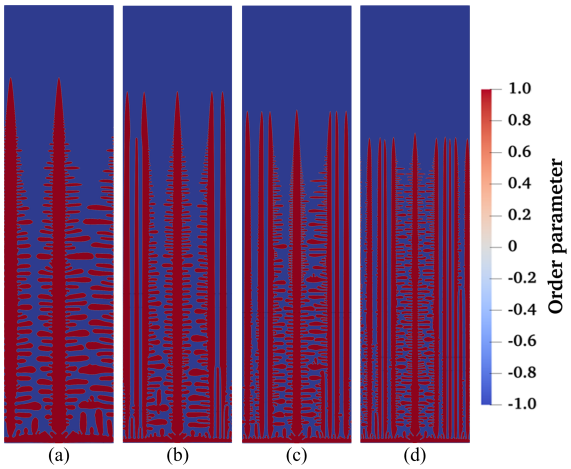

Figure 3.8: Columnar grain structure simulated from the BM I for pulling velocity is (a) 25 mm/s, (b) 50 mm/s,(c) 75 mm/s and (d) 100 mm/s (Same temperature profile)

The decreasing of dendrite tip height in Fig. 3.8 can also be interpreted as decreasing in tip temperature or increasing in tip undercooling, considering the same temperature profile. As was shown in Fig. 3.6, the dendrite tip velocity will be the same as the preset solidification rate at steady state, which means the tip temperature will become a constant. The tip temperature as a function of pulling velocity is shown in Fig. 3.9. As can be seen, the MC model predicts a higher tip temperature especially at lower pulling velocities. A good agreement in tip temperature is seen between the two binary PF models, BM I and BM II. The tip temperatures decreased from about 1820K to about 1787K as the pulling velocity increased from 10 mm/s to 100 mm/s. The Green functions and former PF models found that the dendrite tip velocity is only a function of undercooling at steady-state [4, 6, 27]. The differing tip temperature in the MC model simulations may result from two reasons. First, the deviation of phase equilibrium prediction between the three models, which results from the application of linear equations to introduce the temperature dependence on phase equilibrium calculation. In section 2.4.2.2, it has been shown that there are some deviations of equilibrium solute concentration predictions between the MC model and Thermo-Calc, and there are also deviations between BM models and Thermo-Calc as a pseudo-binary simplification is used. Second, the availability of multiple tie lines in MC model, which means that the solid/liquid interface near the dendrite tips region may have more than one phase equilibrium status options, which also decreases the steady-state tip undercooling for the MC model. However, note that there is no more evidence to show which reason is the dominant one; a further quantifying analysis would be needed to give more supporting evidence.

In this research, we found that the tip temperature or tip undercooling will also

become a constant at a fixed preset pulling velocity, and the dendrite tip temperature will decrease as the pulling velocity increases. In other words, a higher undercooling is needed to maintain a high pulling velocity in the dendrite tip. The results also provide a further explanation of the dendrite tip height difference in Fig. 3.7 between Scheil and PF simulations, as the pulling velocity is not considered in Scheil models. It is reasonable to deduce that the height difference of liquid-mushy zone boundary in Fig. 3.7 will become smaller and smaller as the pulling velocity decreases.

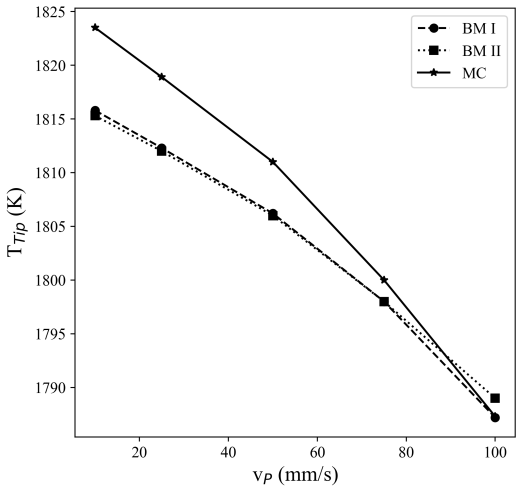

Figure 3.9: Variation of dendrite tip temperature at steady state with pulling velocity

The Secondary Dendrite Arming Spacing (SDAS) is a important parameter that characterize the microstructure of alloys, which largely influence the solute segregation and mechanical properties of alloys. The prediction of SDAS has also been used as a common approach to validate numerical solidification models [7, 20, 29]. There have also been analytical models that aim to predict the SDAS based on the thermal condition and other material properties[29, 30, 31, 32]), and they all predict that the

SDAS decreases as the solidification rate increase. We also run several simulations via the three PF modles to explore the influence of solidification rate on microstructure.

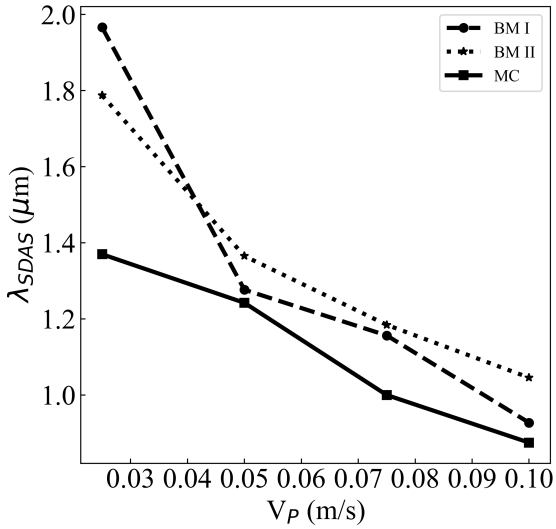

Figure 3.10: Variation of Secondary Dendrite Arming Spacing with cooling rate from the three PF models

Fig. 3.10 examines the influence of cooling rate on SDAS. The cooling rate C_r can be calculated by $C_r = G \times v_p$. As can be seen, both SDAS is predicted to decrease as the cooling rate increases from the three PF models, which agrees with the analytical predictions. It could also be found in Fig. 3.10 that the SDAS predicted by the MC model is smaller when compared with the binary models, which means more secondary arms are forming in the MC model. This could also result from the extra freedom in phase equilibrium or tie line selection provided by the multi-component systems that cannot be accounted for in binary models.

3.5 Conclusion

Benchmarking analysis has attracted the interest of the phase field community. To date, a benchmark analysis of different models with respect to the solidification of multi-component alloys has not yet been carried out. Pseudo-binary models and multi-component models are the two common approaches to simulate the solidification of multi-component alloys. In this study, two binary phase field models and one multi-component phase field model were implemented to simulate the same process, the isothermal and directional solidification of a quaternary Ti-alloy. The findings are as follows:

1. In the isothermal solidification, the three models show a good agreement on dendrite morphology simulations. However, the BM I models cannot predict the differing solute segregation extent of each components, while the BM II and MC models show an excellent agreement on solute redistribution predictions.

2. As for the directional solidification, a steady-state dendrite growth can be simulated by all three models, with the calculated dendrite tip growth velocity shows an excellent agreement.

3. The simulated solid fraction from all three PF models show a lagging growth phenomenon when compared with Scheil simulation, which is a result of the applied high solid-liquid interface pulling velocity.

4. The secondary dendrite arming spacing shows decreasing values with increasing cooling rate. This agrees with the analytical predictions. More side branches and secondary dendrite arms tended to form in MC models.

5. More side branches and secondary arms tend to form in the MC models when compared with the two pseudo-binary models, which may highlight the importance of MC model in providing more potential tie-lines. A quantifying analysis will be proceeded on this in our future work.

Funding: ZL and AP acknowledge the funding provided by the Natural Sciences and Engineering Council of Canada, the Ontario Centre for Innovation, and Collins Aerospace in support of this research. MG acknowledges funding provided the Natural Resources Canada's Office of Energy Research and Development (OERD).

References

[1] B. Echebarria, R. Folch, A. Karma, and M. Plapp, "Quantitative phase-field model of alloy solidification," *Physical review E*, vol. 70, no. 6, p. 061604, 2004.

[2] K. Shampur, "A grand potential based multi-phase field model for alloy solidification," Master's thesis, McGill University, 2017.

[3] J. A. Warren and W. J. Boettinger, "Prediction of dendritic growth and microsegregation patterns in a binary alloy using the phase-field method," *Acta Metallurgica et Materialia*, vol. 43, no. 2, pp. 689–703, 1995.

[4] A. Karma and W.-J. Rappel, "Quantitative phase-field modeling of dendritic growth in two and three dimensions," *Physical review E*, vol. 57, no. 4, p. 4323, 1998.

[5] N. Provatas and K. Elder, *Phase-field methods in materials science and engineering*. John Wiley & Sons, 2011.

[6] J. Kundin, L. Mushongera, and H. Emmerich, "Phase-field modeling of microstructure formation during rapid solidification in inconel 718 superalloy," *Acta Materialia*, vol. 95, pp. 343–356, 2015.

[7] S. Sahoo and K. Chou, "Phase-field simulation of microstructure evolution of ti–6al–4v in electron beam additive manufacturing process," *Additive manufacturing*, vol. 9, pp. 14–24, 2016.

[8] A. A. Wheeler, W. J. Boettinger, and G. B. McFadden, "Phase-field model for isothermal phase transitions in binary alloys," *Physical Review A*, vol. 45, no. 10, p. 7424, 1992.

[9] A. Kermanpur, M. Rappaz, N. Varahram, and P. Davami, "Thermal and grain-structure simulation in a land-based turbine blade directionally solidified with the liquid metal cooling process," *Metallurgical and Materials Transactions B*, vol. 31, no. 6, pp. 1293–1304, 2000.

[10] L. Nastac, "Solute redistribution, liquid/solid interface instability, and initial transient regions during the unidirectional solidification of ti-6-4 and ti-17 alloys," *CFD Modeling and Simulation in Materials Processing*, pp. 123–130, 2012.

[11] B. Böttger, J. Eiken, and M. Apel, "Multi-ternary extrapolation scheme for efficient coupling of thermodynamic data to a multi-phase-field model," *Computational Materials Science*, vol. 108, pp. 283–292, 2015.

[12] H. Azizi, H. Zurob, B. Bose, S. R. Ghiaasiaan, X. Wang, S. Coulson, V. Duz, and A. Phillion, "Additive manufacturing of a novel ti-al-v-fe alloy using selective laser melting," *Additive Manufacturing*, vol. 21, pp. 529–535, 2018.

[13] W. Sun, R. Yan, Y. Zhang, H. Dong, and T. Jing, "Gpu-accelerated three-dimensional large-scale simulation of dendrite growth for ti6al4v alloy based on multi-component phase-field model," *Computational Materials Science*, vol. 160, pp. 149–158, 2019.

[14] J. Eiken, M. Apel, S.-M. Liang, and R. Schmid-Fetzer, "Impact of p and sr on solidification sequence and morphology of hypoeutectic al–si alloys: Combined thermodynamic computation and phase-field simulation," *Acta Materialia*, vol. 98, pp. 152–163, 2015.

[15] J. Eiken, B. Böttger, and I. Steinbach, "Multiphase-field approach for multicomponent alloys with extrapolation scheme for numerical application," *Physical review E*, vol. 73, no. 6, p. 066122, 2006.

[16] M. Greenwood, K. Shampur, N. Ofori-Opoku, T. Pinomaa, L. Wang, S. Gurevich, and N. Provatas, "Quantitative 3d phase field modelling of solidification using next-generation adaptive mesh refinement," *Computational Materials Science*, vol. 142, pp. 153–171, 2018.

[17] Z. Li, M. Greenwood, and A. Phillion, "Fast prediction of phase equilibrium at varying temperatures for use in multi-component phase field models," *Computational Materials Science*, vol. 206, p. 111251, 2022.

[18] H. Azizi, A. Ebrahimi, N. Ofori-Opoku, M. Greenwood, N. Provatas, and M. Mohammadi, "Characterizing the microstructural effect of build direction during solidification of laser-powder bed fusion of al-si alloys in the dilute limit: a phase-field study," *Acta Materialia*, vol. 214, p. 116983, 2021.

[19] J. Kundin, J. L. L. Rezende, and H. Emmerich, "Phase-field modeling of the coarsening in multi-component systems," *Metallurgical and Materials Transactions A*, vol. 45, no. 2, pp. 1068–1084, 2014.

[20] R. Lenart and M. Eshraghi, "Modeling columnar to equiaxed transition in directional solidification of inconel 718 alloy," *Computational Materials Science*, vol. 172, p. 109374, 2020.

[21] A. M. Jokisaari, P. Voorhees, J. E. Guyer, J. Warren, and O. Heinonen, "Benchmark problems for numerical implementations of phase field models," *Computational Materials Science*, vol. 126, pp. 139–151, 2017.

[22] A. M. Jokisaari, P. W. Voorhees, J. E. Guyer, J. A. Warren, and O. G. Heinonen, "Phase field benchmark problems for dendritic growth and linear elasticity," *Computational Materials Science*, vol. 149, pp. 336–347, 2018.

[23] V. Fallah, M. Amoorezaei, N. Provatas, S. Corbin, and A. Khajepour, "Phase-field simulation of solidification morphology in laser powder deposition of ti–nb alloys," *Acta Materialia*, vol. 60, no. 4, pp. 1633–1646, 2012.

[24] J. Heulens, B. Blanpain, and N. Moelans, "A phase field model for isothermal crystallization of oxide melts," *Acta Materialia*, vol. 59, no. 5, pp. 2156–2165, 2011.

[25] N. Moelans, "A quantitative and thermodynamically consistent phase-field interpolation function for multi-phase systems," *Acta Materialia*, vol. 59, no. 3, pp. 1077–1086, 2011.

[26] J. Kundin, E. Pogorelov, and H. Emmerich, "Phase-field modeling of the microstructure evolution and heterogeneous nucleation in solidifying ternary al–cu–ni alloys," *Acta Materialia*, vol. 83, pp. 448–459, 2015.

[27] D. A. Kessler, J. Koplik, and H. Levine, "Geometrical models of interface evolution. iii. theory of dendritic growth," *Physical Review A*, vol. 31, no. 3, p. 1712, 1985.

[28] A. Phillion, M. Založnik, I. Spindler, N. Pinter, C.-A. Aledo, G. Salloum-Abou-Jaoude, H. N. Thi, G. Reinhart, G. Boussinot, M. Apel, *et al.*, "Evolution of a mushy zone in a static temperature gradient using a volume average approach," *Acta Materialia*, vol. 141, pp. 206–216, 2017.

[29] M. M. Franke, R. M. Hilbinger, C. Konrad, U. Glatzel, and R. Singer, "Numerical determination of secondary dendrite arm spacing for in738lc investment castings," *Metallurgical and Materials Transactions A*, vol. 42, no. 7, pp. 1847–1853, 2011.

[30] L. Nastac, J. Valencia, M. Tims, and F. Dax, "Advances in the solidification of in718 and rs5 alloys," *Superalloys*, vol. 718, pp. 625–706, 2001.

[31] H. Weidong, G. Xingguo, and Z. Yaohe, "Primary spacing selection of constrained dendritic growth," *Journal of crystal growth*, vol. 134, no. 1-2, pp. 105–115, 1993.

[32] C. Cicutti and R. Boeri, "On the relationship between primary and secondary dendrite arm spacing in continuous casting products," *Scripta materialia*, vol. 45, no. 12, pp. 1455–1460, 2001.

Chapter 4

A phase field methodology for simulating the microstructure evolution during laser powder bed fusion in-situ alloying process

Complete Citation:

Li, Z., M. Greenwood, and A. Phillion. "A phase field methodology for simulating the microstructure evolution during laser powder bed fusion in-situ alloying process." *IOP Conference Series: Materials Science and Engineering.* Vol. 1281. No. 1. IOP Publishing, 2023.

A phase field methodology for simulating the microstructure evolution during laser powder bed fusion in-situ alloying process

Z. Li[1], M. Greenwood[1,2], A.B. Phillion[1]

[1]*Department of Materials Science and Engineering, McMaster University, Hamilton, Canada*

[2]*Canmet MATERIALS, Natural Resources Canada, 183 Longwood Road south, Hamilton, ON, Canada*

Abstract:

A recently-developed [1] multi-component phase field model has been utilized to investigate microstructure evolution during in-situ alloying of a blended elemental Ti-1Al-8V-5Fe alloy powder via the Laser Powder Bed Fusion process. The process of in-situ alloying, where elemental powder is used instead of pre-alloyed powder, was studied by performing two simulations having: (1) a uniform initial composition, and (2) a spatially varying initial composition to represent different powder particles. Specifically, the grain morphology, solute distribution, competitive growth and nucleation under the two different scenarios were simulated and compared. To assist the microstructure simulations, a macro-scale finite element model was developed to simulate the heat transfer during LPBF process. The thermal history data calculated by the finite element model was provided to the phase field model in order to simulate transient dendritic growth behaviour. The results show that a set of evenly-spaced columnar dendrites form in the uniform initial composition case, whereas when the initial composition is spatially varying, non-uniform dendrites having elongated shape can develop. It is also shown that competitive growth between dendrites is influenced by nucleation. For the spatially varying initial composition case, the results indicate

that full alloying is difficult to achieve during the LPBF printing process; this incomplete alloying greatly influences the dendrite morphology and solute distribution.

4.1 Introduction

Additive Manufacturing (AM), which directly fabricates parts via layer-by-layer printing methods, has become a popular alternative to conventional subtractive manufacturing processes over the last 30 years [2, 3]. The major advantage of AM is that, after the AM process, only minimal post-processing machining is needed. This opens up significant possibilities in non-traditional markets for materials with poor machinability, e.g. β-Ti alloys [4].

β-Ti alloys are a class of Ti alloys where the predominant phase is β. This microstructure results in higher specific strength while still offering acceptable toughness and good fatigue resistance as compared to other Ti alloys [5]. However, β alloy possesses a number of significant limitations. First, due to the addition of Mo and Cr as β stabilizers, they are expensive. Second, because of their poor machinability, β alloys can be difficult to fabricate via conventional machining processes. To resolve these issues, Azizi et al. [3] proposed to utilize a low cost Fe-containing β alloy, Ti-1Al-8V-5Fe (wt %) alloy, and a Laser Powder Bed Fusion (LPBF) in-situ alloying process, to make β-Ti components. Although the Ti-185 alloy was patented more than fifty years ago, the strong segregation tendency of Fe, and the resulting formation of brittle phases during casting [3] made this alloy not commercially feasible via conventionally processing. However, with the advancement of AM technologies, the utility of this alloy is being reassessed.

Laser Powder Bed Fusion (LPBF) is one of the most common metal AM processes as it offers high dimensional accuracy on small and medium size components. During LPBF, the molten pool undergoes rapid cooling whereby the cooling rates reaches

values on the order of $10^5 - 10^6$ K/s, resulting in the formation of novel microstructures [6]. Traditionally, pre-alloyed powders have been used in LPBF, however, these can be costly especially for alloy development purposes.

Blended elemental powder are an alternative to pre-alloyed powders. This technique utilizes pure elemental powders as a substitute for prealloyed powders (e.g. Ti, Al and V powders instead of Ti-6Al-4V powders when building Ti-64 parts), and thus the alloying process occurs during the melting and subsequent reheating phase. Azizi et al. [3] built a Ti-1Al-8V-5Fe sample via LPBF of blended elemental powder of Ti, Al-V, and Fe, achieving in-situ alloying. Their Ti-185 sample showed the development of a fine microstructure, a remarkable combination of strength and plasticity, as well as homogeneity in alloy concentration. Ahmed et al. [7] performed a further investigation on the in-situ alloying process of Ti-185 using synchrotron X-ray diffraction. They found that the laser melting resulted in only partial alloying (i.e. alloyed and unmixed regions coexist), with the full alloying being achieved only during subsequent reheating cycles. However, it remains unclear how the alloying process proceeds and how the microstructure evolves during LPBF of blended elemental powders.

Over the last 30 years, the Phase Field (PF) method has become a popular approach to study the solidification process during conventional casting and emerging AM processes. In PF, a phase field ϕ is used to represent the liquid ($\phi = -1$) and solid ($\phi = 1$) phases, while a continuous function between $-1 < \phi < 1$ represents the mushy zone. The phase field will evolve along the direction of local free energy minimization, and thus the computational expense of interface tracking is not needed. Owing to the advantages of the PF method, it would seem perfectly suited to studying in-situ alloying during LPBF of blended elemental powders. Sahoo et

al. [8] simulated microstructure evolution during electron beam AM processing of pre-alloyed Ti-64 powder in order to establish a relation between process parameters and grain size. However, nucleation was not considered in their model, and the multi-component system was simplified to a pseudo-binary alloy. Lenart et al. [9] simulated the Columnar to Equiaxed Transition (CET) of a pre-alloyed Ni-based superalloy during Directional Solidification, in order to study the influence of temperature gradient and solidification rate on the CET. Once again, a pseudo-binary assumption was applied.

While PF modelling using the pseudo binary approach improves the computational efficiency, and has been shown to simulate closely experimentally-produced microstructures, a homogeneous solute distribution is a necessary initial condition. Thus, it cannot be used to simulate in-situ alloying during LPBF of blended elemental powders. Multi-component PF models are highly accurate but computationally inefficient because they need to calculate the phase equilibrium of the multi-component system. Sun et al. [10] solved this problem for the case of dendritic growth of the Ti-64 alloy by considering multiple binary systems, specifically Ti-Al and Ti-V, each with their own partition coefficient k. However, the interaction between solutes was not considered and thus a true interfacial equilibrium was not achieved. Kundin et al. [11] adopted another multi-component PF model to simulate the rapid solidification processes. In their work the phase equilibrium was calculated at one concentration point, however the co-existence of multiple tie lines was ignored. Eiken et al. [12] improved the phase equilibrium prediction accuracy utilizing the quasi-equlibrium approach but at the cost of low computational efficiency since the quasi-equilibrium calculation was carried out at every node point and for each time step of the model [13]. Recently,

Li et al.[1] proposed a new convex-hull based method to calculate the phase equilibrium of multi-component systems, and combined this with the grand potential PF model developed by Provatas [14] as well as a a dynamic adaptive mesh refinement method by Greenwood [15]. This combination of methods was shown to achieve a great combination of prediction accuracy and computational efficiency.

The other challenge when modelling microstructure development during LPBF via the PF method is the need to obtain the thermal history. While it is possible to simulate heat and mass transfer simultaneously within PF models, this is computationally expensive. Moreover, it is unnecessary since heat transfers much faster than mass [16, 17]. Simulating the thermal problem via finite element analysis (FEA) and then imposing the temperature history on the PF domain is a well-utilized substitution that provides computational efficiencies while still maintaining high accuracy in temperature evolution predictions [8, 14, 18]. Sahoo et al. [8] explored the relation between electron beam scanning speed and primary dendrite arming spacing during a Ti-64 alloy electron beam AM using this approach. However, the thermal conditions in the AM process were simplified to a directional solidification case where a single solidification rate was defined in their model. Thus, the complex transient thermal gradients and solidification rates that are known to occur during AM processing were ignored. Xiao et al. [18] overcome this issue by dividing the domain into different simulations to represent different regions within the molten pool. While more detailed knowledge of thermal gradients and solidification rates were obtained for the PF simulations, a Directional Solidification condition was still defined in each region and thus a panoramic picture of the whole molten pool was not obtained.

In the present study, a multi-component PF model is used to simulate microstructure development and in-situ alloying during LPBF of the Ti-185 alloy in blended elemental form. In-situ alloying is simulated by designing spatially varying initial composition fields to represent the elemental powders. Solidification of the same alloy but within a uniform initial concentration field, to represent pre-alloyed powder, is also simulated as a reference state. Finally, as input to the PF models, a finite element model is developed to simulate the transient heat transfer occurring during LPBF. These simulations are used to investigate grain morphology, solute distribution, and nucleation, and well as dendrite growth competition.

4.2 Numerical Methods

4.2.1 Phase Field Simulations

The multi-component PF model implemented in the present study was proposed by Provatas et al. [1, 14, 15, 19]. The formulation of this model begins with a quadratic description of the free energy of the solid and liquid phases,

$$F^{\theta}\left(c_1, c_2, ...c_n - 1\right) = \frac{1}{2}\sum_{i=1}^{n-1}\sum_{j=1}^{n-1} A_{ij}^{\theta}\left(c_i - \bar{c}_i^{\theta}\right)\left(c_j - \bar{c}_j^{\theta}\right) + \sum_{j=1}^{n-1} B_j^{\theta}\left(c_j - \bar{c}_j^{\theta}\right) + D^{\theta}, \quad (4.1)$$

where F^{θ} represents the free energy of phase θ, c_i and c_j are the concentration of component i and j, A_{ij}^{θ}, $\bar{c}_i^{\theta}$, B_j^{θ} and D^{θ} are fitting parameters. To get the fitting parameters, a data set $\{c_1, c_2, ..., c_{j-1}, F\}$ that contains a massive number of concentration-free energy data points is extracted from a thermodynamic database

(e.g. Thermo-Calc), and then fit via a least square method. The fitting parameters will also be used in the phase field equations.

The evolution of the order parameter ϕ and chemical potential μ are expressed based on the free energy relaxation principle,

$$\tau(\vec{n})\frac{\partial\phi}{\partial t} = W_\phi(\vec{n})^2\nabla^2\phi + \phi - \phi^3 - (1-\phi^2)^2\left(\frac{(I-[K])^T}{2}\vec{U} + \hat{n}_c\right)^T[\lambda]\vec{U}, \quad (4.2)$$

and

$$[\chi]\frac{\partial\vec{\mu}}{\partial t} = \nabla\left[[M]\nabla\vec{\mu} + Wa(\phi)|\Delta\vec{c}_{eq}|\{\hat{n}_c + (I-[K])^T\vec{U}\}\frac{\partial\phi}{\partial t}\frac{\nabla\phi}{|\nabla\phi|}\right] + \frac{1}{2}|\Delta\vec{c}_{eq}|\{\hat{n}_c + (I-[K])^T\vec{U}\}\frac{\partial\phi}{\partial t}, \quad (4.3)$$

where $\vec{\mu}$ is a vector representing the chemical potentials of each solute component μ_i, I is the identity matrix, $\vec{n} \equiv \frac{\vec{\nabla}\phi}{|\vec{\nabla}\phi|}$ is the normal direction to the interface, $a_s(\vec{n})$ represents the 2D four-fold anisotropy, $W_\phi(\vec{n}) = W_0 a_s(\vec{n})$ sets the interface width [16], and

$$\left[\chi^\theta\right]^{-1}_{ij} = A^\theta_{ij}, \quad (4.4)$$

$$\vec{U} = \frac{\left[\chi^L\right]}{|\Delta\vec{c}_{eq}|}\left(\vec{\mu} - \vec{\mu}_{eq}\right), \quad (4.5)$$

$$\Delta\vec{c}_{eq} = \vec{c}^L_{eq} - \vec{c}^S_{eq}, \quad (4.6)$$

$$\hat{n}_c = \frac{\Delta\vec{c}_{eq}}{|\Delta\vec{c}_{eq}|}, \tag{4.7}$$

$$[K] = \left[\chi^L\right]^{-1}\left[\chi^S\right], \tag{4.8}$$

$$[\lambda] = \lambda_o \frac{|\Delta\vec{c}_{eq}|^2}{|\Delta\vec{c}_{eq,i}|^2}[\chi^L]^{-1}\chi^L_{ii}, \tag{4.9}$$

$$d_{0,i} = \frac{2\sigma_{SL}}{|\Delta\vec{c}_{eq,i}|^2}\chi_{ii} \tag{4.10}$$

$$\lambda_o = \frac{a_1 W_0}{d_{0,i}} \tag{4.11}$$

$$[\chi] = \left[\chi^L\right]\{I - (I - [K])\, h(\phi)\}, \tag{4.12}$$

$$[M] = q(\phi)\left[D^S\right]\left[\chi^S\right] + (1 - q(\phi))\left[D^L\right]\left[\chi^L\right]. \tag{4.13}$$

Note that in this set of equations, $h(\phi)$ and $q(\phi)$ are the interpolation equations commonly used in PF models, $d_{0,i}$ is the capillary length of the ith component, λ_o is the coupling coefficient [20], $a_1 = 0.8839$ is a constant, σ_{SL} is the solid-liquid interface energy, $\left[D^\theta\right]$ is the diffusion coefficient matrix that is related to the physical properties of the alloy system, matrices $[K]$ and $\left[\chi^\theta\right]$ are related to the free energy surface given in Eq. 4.1, and $\mu_{eq,i}$, $c^L_{eq,i}$ and $\vec{c}^S_{eq,i}$ represent the equilibrium chemical potential and the equilibrium concentration of the ith component in the liquid and solid phases.

The last three terms, $\vec{\mu}_{eq}$, $\vec{c}^{L}_{eq}$ and c^{S}_{eq} all vary as a function of local temperature T; please refer [1] for the calculation methodology. Finally, the term $a_s(\vec{n})$ is calculated as

$$a_s(\vec{n}) = 1 + \epsilon_4 cos4(\theta + \theta_0), \tag{4.14}$$

where ϵ_4 is a material parameter characterizing the anisotropy strength, θ is the angle between the interface normal and pulling direction, and θ_0 is the misorientation angle between the preferred crystalline orientation and the global coordinate system [21].

In addition to the model described in [1], the model used in this study uses a nucleation module to take into account the formation of equiaxed grains. Assuming no solid grain movement, the nucleation probability P_n within an area $\Delta S = \Delta x \Delta y$ at a given time range Δt is calculated by [9, 22, 23]

$$P_n = -2\mu_N(\Delta T)\frac{\partial T}{\partial t}(1 - f_s)\Delta S \Delta t \tag{4.15}$$

where $\mu_N = 5 \times 10^5$ $\mathrm{m^{-2}K^{-2}}$ [23] is the nucleation possibility parameter, ΔT is the local undercooling, $\partial T/\partial t$ is the cooling rate and (1-f_s) is the local liquid fraction.

Eq. 4.15 is an empirical equation first developed in late 1990s by Nastac et al. [23, 24] for simulating nucleation phenomena within a stochastic model. More recently, this approach was applied to PF models to simulate the columnar to equiaxed transition [9, 22]. During the simulation, the nucleation module is applied is follows. First, Eq. 4.15 is applied at each nodal point, after every 100 time steps assuming that $f_s = (1 + \phi)/2$, and that the value of Δx is the local grid spacing, and that the value of Δt is the actual time between two consecutive nucleation check stages. During this "nucleation check stage", a random number between 0 and 1 is generated

at each nodal point, and compared with the value of P_n calculated at that point. Nucleation occurs if P_n is larger than that of the random number.

4.2.2 Finite Element Thermal Analysis

The temperature evolution during LPBF of the Ti-185 alloy is simulated via the commercial ABAQUS software package. The model geometry includes one layer of deposited blended elemental powder on top of a substrate of uniform Ti-185. This approach was taken for computational efficient to approximate the steady-state printing of Ti-185. The dimensions of the substrate and deposited layer are: 3 mm × 1 mm × 1.06 mm and 3 mm × 1 mm × 0.06 mm, respectively. Heat transfer is assumed to be conduction-only, i.e.

$$\rho c_p \frac{\partial T(X,Y,Z,t)}{\partial t} = -\nabla \cdot \vec{q}(X,Y,Z,t) + Q(X,Y,Z,t) \tag{4.16}$$

where ρ is the density, c_p represents the specific heat capacity under constant pressure and T is the local temperature. Additionally, $\vec{q} = -k(T)\nabla T$ is the heat flux that results from the temperature gradient, which reprensents the heat conduction, $k(T)$ is the temperature dependent heat conductivity of the material, and Q represents other heat sources, which includes heat input from lasers and release of latent heat in this model.

In the present FEA model, the heat input from the laser beam is simulated by a Gaussian distributed moving heat source, written as [25]

$$Q(x,y) = \frac{2\lambda P}{\pi r_0^2} exp\{\frac{-2[(x-x_0)^2 + (y-y_0)^2]}{r_0^2}\} \tag{4.17}$$

where λ is the absorptivity of the material, P is the laser power, r_0 is the laser radius and (x_0, y_0) is the position of the laser center that varies with time according to the laser scanning speed, v. Convection and radiation are not considered. The preheat temperature, T_0 is used as the initial condition. Finally, the FEA domain is meshed with cuboid elements, 20×20×100 µm and 20×20×15 µm respectively in the substrate and the deposited layer.

4.2.3 Numerical Implementation of the PF, FEA, and Nucleation Modules

Fig. 4.1 shows a flowchart of the integration of the PF, FEA, and Nucleation modules. First, the FEA simulation is run to acquire the thermal history during LPBF processing. Second, the model parameters for the PF simulation are determined. Specifically, (1) the multi-component phase equilibrium is predicted using the method presented in [1] and (2) the capillary length of the material d_0 is calculated by calculating the $d_{0,i}$ for each component via Eq. 4.10 (Note - the reference component is chosen to be the one with the smallest capillary length). Third, the PF model is advanced from one time-step to the next. At each time-step the temperature values from the FEA simulation are linearly interpolated to the nodal points on the PF mesh.

The relevant PF simulation parameters are listed in Table 4.1, while the relevant processing parameters for the thermal simulation are listed in Table 4.2. Given the high thermal gradient found in LPBF, the PF simulation contains a large number of nodes in order to reveal the fine microstructure details; the domain size, 280 μm × 70 μm was determined from the thermal simulation as discussed in Section 3. Note that the domain size and interface widths for the prealloyed powders and elemental

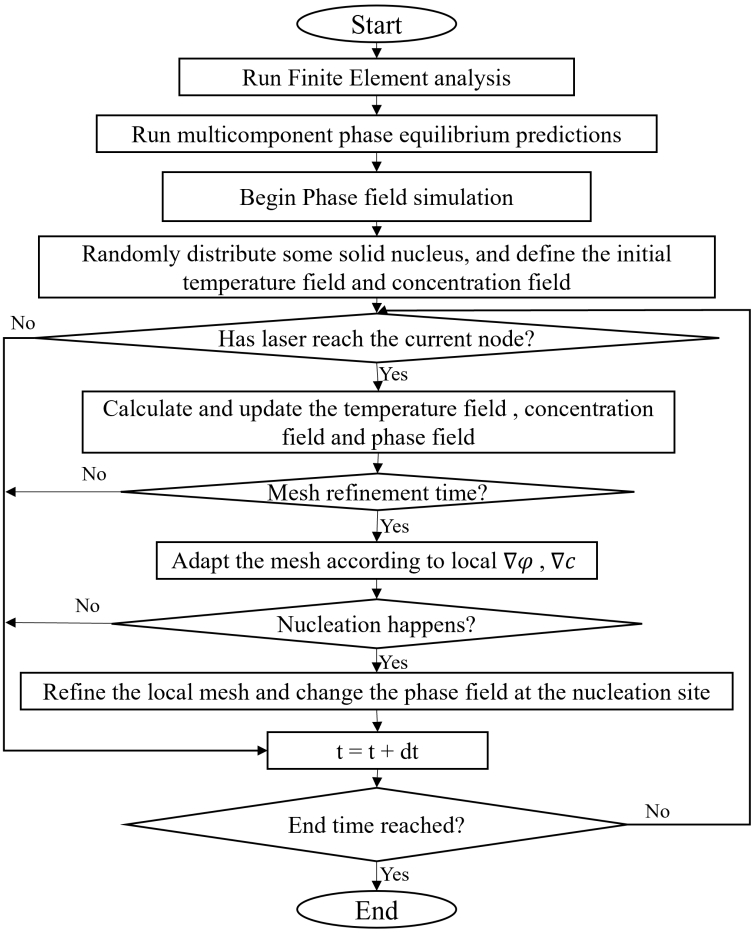

Figure 4.1: Flowchart showing the numerical implementation of the PF, FEA, and Nucleation Modules to simulate the LPBF process.

powders were assumed to be the same. The thermodynamic free energy data of the Ti-alloy was extracted from the Thermo-Calc^{TM} TCTI 2 database. It should be noted that there are several assumptions with this model that must be acknowledged. Specifically, these assumptions include: (1) the local composition was only affected by diffusion without the consideration of convection in the melt pool; (2) the movement of the elemental powders and the new nucleated equiaxed grains were not considered; (3) only two stable phases exist throughout the simulation temperature range.

Table 4.1: Simulation parameters used in the phase field simulations [8][10]

PF parameters	Value
σ_{SL} (J/m^2)	0.046
ϵ_4	0.05
D_L (m^2/s)	9.5E-9
D_S (m^2/s)	5.0E-13
W ($\times 10^{-9}$m)	14.2
λ_o	11.76
grid points	6144×24576
domain size(µm)	70×280
Mesh spacing (dx)	0.8

Table 4.2: Process parameters of LPBF-Ti185 alloy used in the finite element analysis [3]

Laser power P	370 W
Scanning speed v	1035 mm/s
Laser spot size r_0	0.06 mm
Preheat temperature T_0	80 °C
Absorptivity λ	0.5

4.3 Results and discussions

4.3.1 Finite Element Analysis

The simulated temperature profile and molten pool geometry in XoY (top surface) and XoZ (side surface) planes are depicted in Fig. 4.2. These results show that the molten pool depth reaches about 70 µm, which exceeds the powder layer thickness and means that the substrate is also partially melted, thus a great connection between the newly deposited layer and prior layer (the substrate in this case) is expected.

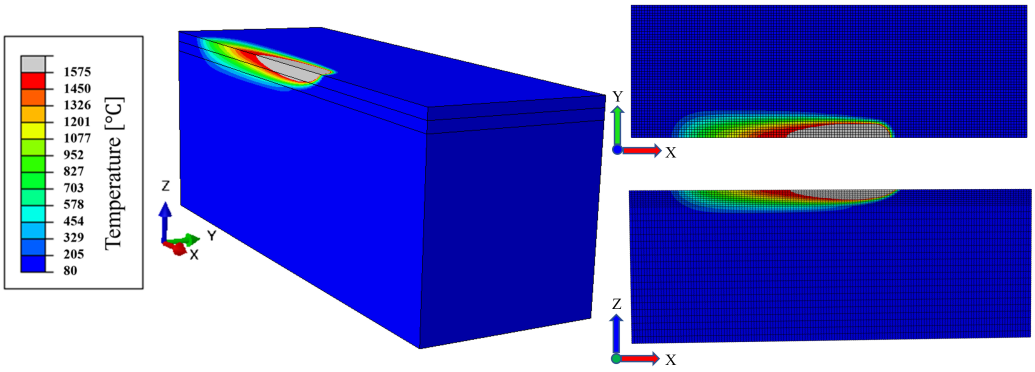

Figure 4.2: Contour plot and XoY and XoZ views of the temperature profile and molten pool geometry from the heat transfer finite element analysis

4.3.2 Initial condition for the Phase field models

Using the FEA results shown in Fig. 4.2 as a guide, a domain of 70 µm × 280 µm was utilized for the PF simulation. This was chosen to match the depth of the melt pool, while being four time larger in the direction of laser travel in order to simulate relevant phenomena. Fig. 4.3 provides (a) a schematic of the FEA temperature field applied to the PF domain, as well as (b) the corresponding uniform concentration

map for the Ti-185 alloy to simulate the pre-alloyed condition, and (c) the spatially varying concentration map with particles of Ti (dark green), Al-V (light green), and Fe (yellow) to simulate the blended-alloy condition within a background of Ti-185 uniform composition. The number and radius of the Ti, Al-V and Fe powders were calculated based on their volume fraction.

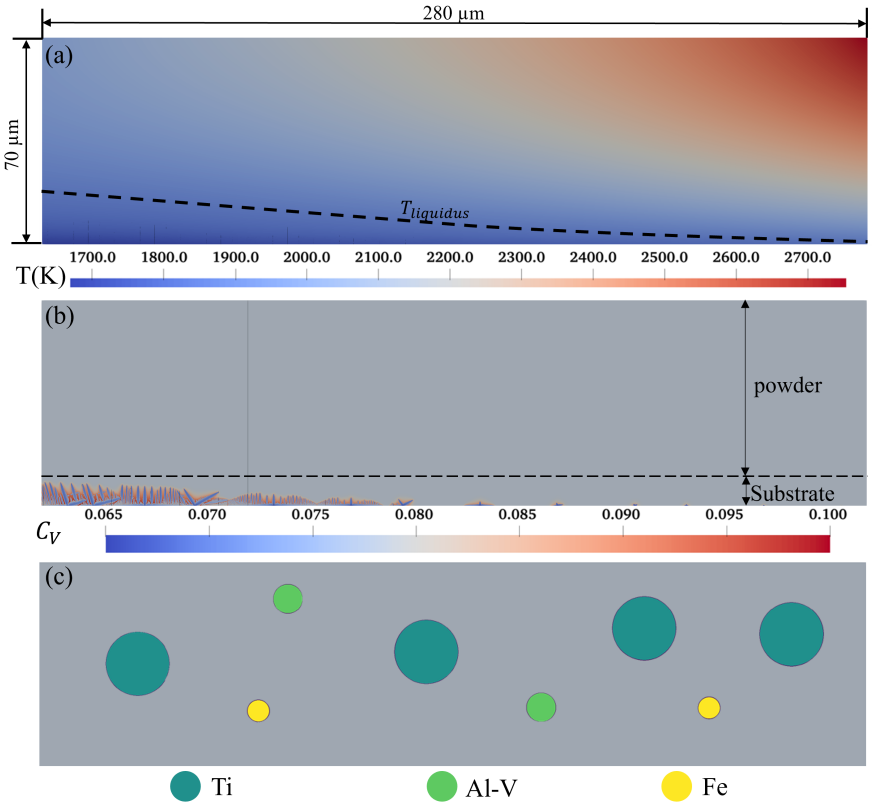

Figure 4.3: The initial condition for the phase field simulations, including (a) a snapshot of the temperature profile and domain geometries, (b) the uniform concentration map with initial microstructure, and (c) the spatially varying concentration map with a background of Ti-185.

As can be see in Fig. 4.3(a), the liquidus line at $T = 1848$ K is nearly parallel to the direction of laser beam travel with some incline angles with decreasing temperature. Analysis of the thermal data showed a temperature gradient along the Z direction G_z

of about 1.4×10^7 K/m, and a temperature gradient along the X direction G_x of about 4.2×10^6 K/m. Referring now to Fig. 4.3(b), the initial microstructure is shown, with random crystal orientations placed at the bottom of the domain in the region of lowest temperature given by Fig. 4.3(a). Specifically, three different crystal orientations were imposed, $\phi_1 = 0$, $\phi_2 = \pi/12$ and $\phi_3 = \pi/6$, with respect to [001] direction. Fig. 4.3(c) shows the initial locations of the Ti, Al-V and Fe powders; the number and radius of the Ti, Al-V and Fe powders seen in the image were calculated based on their volume fraction. Note that the background phase was assumed to be Ti-185 and not pure Ti. This was done as a result of numerical limitations and real mass transfer condition. As the laser begins to scan over the blended elemental powders, the melting and alloying of different elemental powders has been initiated, thus a Ti-185 background at the beginning of solidification is a reasonable assumption. Additionally, the mesh spacing and time scale of the PF model is determined according to the thermodynamic data of Ti-185 alloy; carrying out the simulation with a background of pure Ti would result in significant numerical instabilities.

4.3.3 Phase field simulation during LPBF using pre-alloyed powders

The evolution of microstructure during LPBF in the pre-alloyed Ti-185 case is shown in Fig. 4.4. A differing solute redistribution phenomena is predicted by the PF model for the different solute components. Al (Fig. 4.4a) is enriched in the solid phase, while Fe (Fig. 4.4b)and V (Fig. 4.4c) are segregated in the liquid phase with a more evident segregation is predicted for Fe, which is consistent with thermodynamic predictions [1]. Furthermore, a fine columnar dendrite structure is seen, with competitive growth

between dendrites of different orientation.

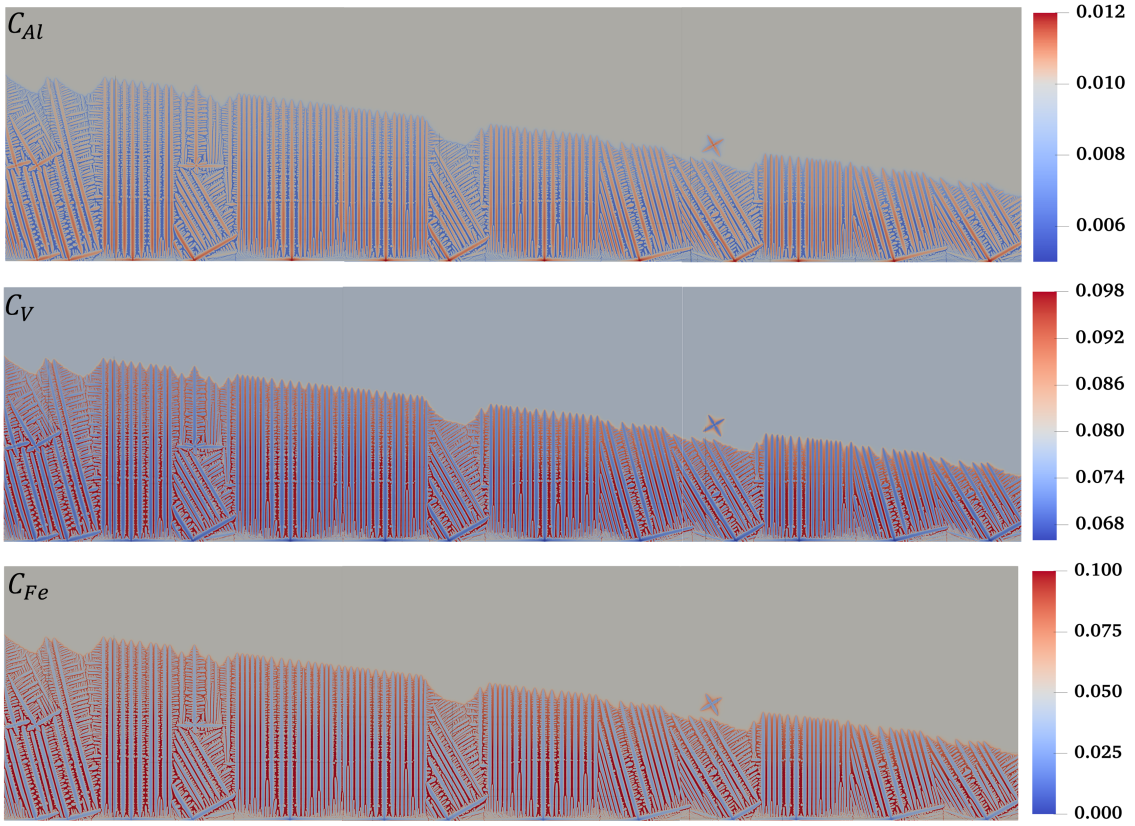

Figure 4.4: A snapshot at t = 0.65 ms of the concentration profile of Al, V and Fe during using pre-alloyed powder in laser powder bed fusion process

The simulation showed a strong [001] direction solidification texture, which is consistent with previous observations reported in the literature [2]. As shown in Fig. 4.4, the grains with their preferred grain growth direction aligned with the build (vertical) direction have a growth advantage, and are able to block growth of the adjacent grains. This growth advantage is well known, and is a result of the fact that for "inclined grains", a higher dendrite tip velocity and tip undercooling is needed when compared with the "vertical grains" to catch up to the pulling velocity [26]. This ultimately results in blockage by primary or even secondary dendrite arms of

grains oriented in the build direction.

The PF simulation also shows several nucleation phenomena that may also influence the competitive growth process. Specifically, nucleation only occurred on the top of "inclined grains", and not the "vertical grains". This difference results from the difference in local undercooling between the two. As a high undercooling is needed to initiate the nucleation during the LPBF process, undercooling on the top of "inclined grains" tips is greater as compared with the "vertical grains". The new nucleated grains also block the growth of the "inclined grains", resulting in a further growth advantage of the "vertical grains".

4.3.4 Phase field simulation during LPBF using elemental powders

The evolution of microstructure during LPBF in the blended elemental Ti-185 case is shown in Fig. 4.5.

When using blended elemental powders, a significantly different microstructure evolution process is observed as compared to the case with pre-alloyed powders. First, the solute distribution is significantly altered due to the presence of elemental powders. Due to diffusion, these regions are centered at the initial locations of the elemental powders but are much larger in size. The highest solute concentrations are 8%, 65% and 50% for Al, V and Fe, respectively and reduce the further away from the powder centers. Dendrite growth begins far away from these solute rich regions and initially, the growth behavior is similar to that seen in the pre-alloyed powder case. However, once the dendrite tip reaches the regions of high solute concentration, further growth is inhibited. Dendrite growth is completely impeded by the local

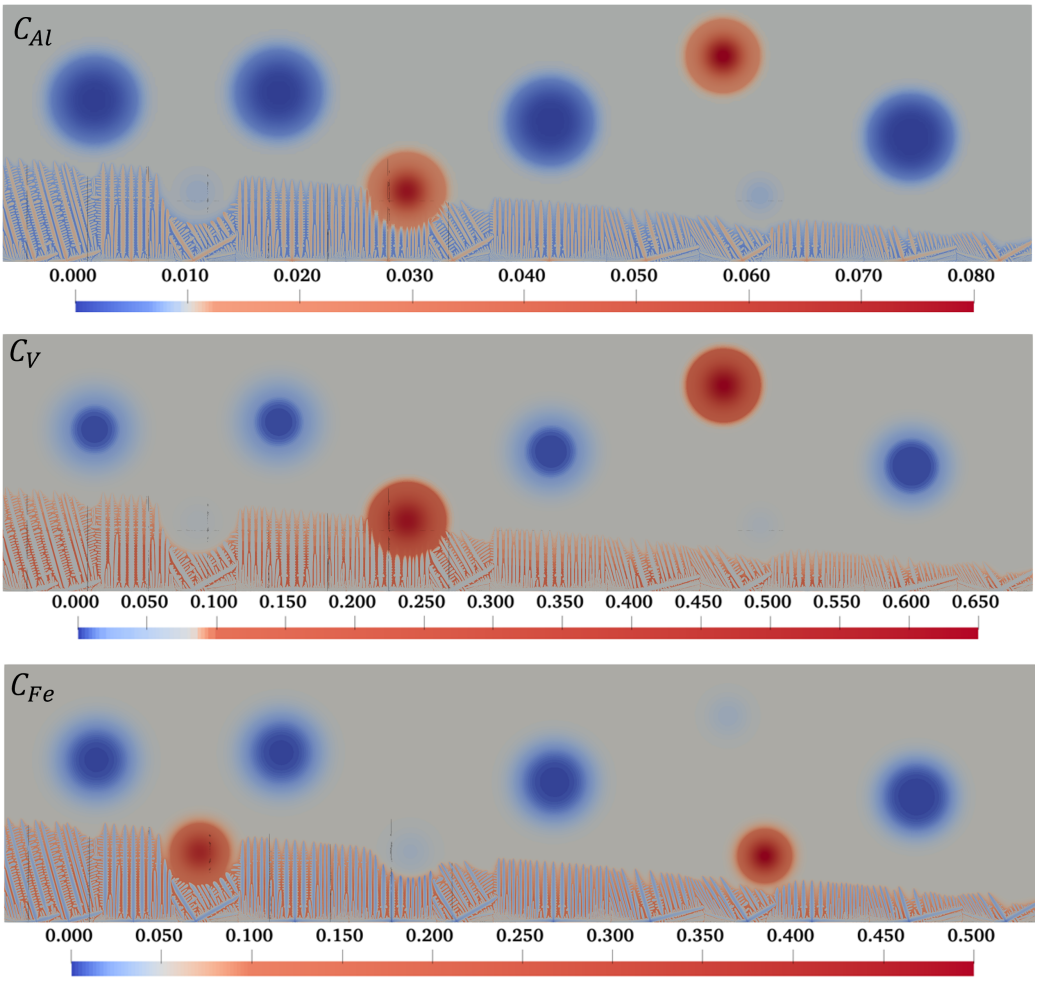

Figure 4.5: A snapshot at t = 0.45 ms of the concentration profile of Al, V and Fe during LPBF using pre-alloyed powders.

enrichment of Fe, and significantly slowed by local enrichment of Al and V.

The influence of solute enrichment on columnar dendrite growth can be explained from both thermodynamic and kinetic aspects. First, the enrichment of Fe and V would cause a decrease to the local liquidus and solidus according to the phase diagram. For a given temperature, this effectively decreases the undercooling and thereby reduces the driving force for dendrite growth. Second, Fe and V segregate into the liquid during solidification. However, local enrichment of Fe and V decreases the concentration gradient of these solutes, decreasing the diffusion rate of these elements. This increases the time taken for solute diffusion at the solid/liquid interface.

4.4 Conclusions

This study has examined how microstructure develops during LPBF of Ti-185 β titanium alloy. Using a multi-component PF model integrated with finite element thermal analysis and a model for grain nucleation, a comparison between pre-alloyed powder and a blended elemental powder has been made. The findings are as follows:

1. The PF simulation during LPBF of Ti-185 using pre-alloyed powders shows a columnar dendrite growth: Fe and V segregate to the liquid phase while Al segregates to the solid. The grain with crystal orientation aligned to the build direction shows a considerable growth advantage. Nucleation is observed to occur above the "inclined grains", which blocks their growth of inclined dendrites.

2. The PF simulation during LPBF of Ti-185 using elemental powders shows that

regions enriched in Fe significantly impede dendrite growth, while regions enriched in Al and V also slow the dendrite growth. This results in complete alloying not being achieved during a single layer deposition process, but, as shown experimentally by [7], requiring subsequent reheating cycles.

4.5 Acknowledgement

ZL and AP acknowledge the funding provided by the Natural Sciences and Engineering Council of Canada in support of this research. MG acknowledges funding provided the Natural Resources Canada's Office of Energy Research and Development (OERD).

References

[1] Z. Li, M. Greenwood, and A. Phillion, "Fast prediction of phase equilibrium at varying temperatures for use in multi-component phase field models," *Computational Materials Science*, vol. 206, p. 111251, 2022.

[2] J. Li, X. Zhou, M. Brochu, N. Provatas, and Y. F. Zhao, "Solidification microstructure simulation of ti-6al-4v in metal additive manufacturing: A review," *Additive Manufacturing*, vol. 31, p. 100989, 2020.

[3] H. Azizi, H. Zurob, B. Bose, S. R. Ghiaasiaan, X. Wang, S. Coulson, V. Duz, and A. Phillion, "Additive manufacturing of a novel ti-al-v-fe alloy using selective laser melting," *Additive Manufacturing*, vol. 21, pp. 529–535, 2018.

[4] A. Machado and J. Wallbank, "Machining of titanium and its alloys—a review,"

Proceedings of the Institution of Mechanical Engineers, Part B: Journal of Engineering Manufacture, vol. 204, no. 1, pp. 53–60, 1990.

[5] C. Ng, M. Bermingham, and M. Dargusch, "Controlling grain size, morphology and texture in additively manufactured β-titanium alloy with super transus hot isostatic pressing," *Additive Manufacturing*, vol. 59, p. 103176, 2022.

[6] Y. Liu, L. Xu, and C. Qiu, "Development of an additively manufactured metastable beta titanium alloy with a fully equiaxed grain structure and ultrahigh yield strength," *Additive Manufacturing*, vol. 60, p. 103208, 2022.

[7] F. F. Ahmed, S. J. Clark, C. L. A. Leung, L. Stanger, J. Willmott, S. Marussi, V. Honkimaki, N. Haynes, H. S. Zurob, P. D. Lee, *et al.*, "Achieving homogeneity in a high-fe β-ti alloy laser-printed from blended elemental powders," *Materials & Design*, vol. 210, p. 110072, 2021.

[8] S. Sahoo and K. Chou, "Phase-field simulation of microstructure evolution of ti–6al–4v in electron beam additive manufacturing process," *Additive manufacturing*, vol. 9, pp. 14–24, 2016.

[9] R. Lenart and M. Eshraghi, "Modeling columnar to equiaxed transition in directional solidification of inconel 718 alloy," *Computational Materials Science*, vol. 172, p. 109374, 2020.

[10] W. Sun, R. Yan, Y. Zhang, H. Dong, and T. Jing, "Gpu-accelerated three-dimensional large-scale simulation of dendrite growth for ti6al4v alloy based on multi-component phase-field model," *Computational Materials Science*, vol. 160, pp. 149–158, 2019.

[11] J. Kundin, L. Mushongera, and H. Emmerich, "Phase-field modeling of microstructure formation during rapid solidification in inconel 718 superalloy," *Acta Materialia*, vol. 95, pp. 343–356, 2015.

[12] J. Eiken, M. Apel, S.-M. Liang, and R. Schmid-Fetzer, "Impact of p and sr on solidification sequence and morphology of hypoeutectic al–si alloys: Combined thermodynamic computation and phase-field simulation," *Acta Materialia*, vol. 98, pp. 152–163, 2015.

[13] J. Eiken, B. Böttger, and I. Steinbach, "Multiphase-field approach for multicomponent alloys with extrapolation scheme for numerical application," *Physical review E*, vol. 73, no. 6, p. 066122, 2006.

[14] H. Azizi, A. Ebrahimi, N. Ofori-Opoku, M. Greenwood, N. Provatas, and M. Mohammadi, "Characterizing the microstructural effect of build direction during solidification of laser-powder bed fusion of al-si alloys in the dilute limit: a phase-field study," *Acta Materialia*, vol. 214, p. 116983, 2021.

[15] M. Greenwood, K. Shampur, N. Ofori-Opoku, T. Pinomaa, L. Wang, S. Gurevich, and N. Provatas, "Quantitative 3d phase field modelling of solidification using next-generation adaptive mesh refinement," *Computational Materials Science*, vol. 142, pp. 153–171, 2018.

[16] N. Provatas and K. Elder, *Phase-field methods in materials science and engineering*. John Wiley & Sons, 2011.

[17] B. Echebarria, R. Folch, A. Karma, and M. Plapp, "Quantitative phase-field model of alloy solidification," *Physical review E*, vol. 70, no. 6, p. 061604, 2004.

[18] W. Xiao, S. Li, C. Wang, Y. Shi, J. Mazumder, H. Xing, and L. Song, "Multi-scale simulation of dendrite growth for direct energy deposition of nickel-based superalloys," *Materials & Design*, vol. 164, p. 107553, 2019.

[19] K. Shampur, "A grand potential based multi-phase field model for alloy solidification," Master's thesis, McGill University, 2017.

[20] V. Fallah, M. Amoorezaei, N. Provatas, S. Corbin, and A. Khajepour, "Phase-field simulation of solidification morphology in laser powder deposition of ti–nb alloys," *Acta Materialia*, vol. 60, no. 4, pp. 1633–1646, 2012.

[21] M. Gaoyang, X. Lingda, W. Chunming, J. Ping, and Z. Guoli, "Two-dimensional phase-field simulations of competitive dendritic growth during laser welding," *Materials & Design*, vol. 181, p. 107980, 2019.

[22] P. Nie, O. Ojo, and Z. Li, "Numerical modeling of microstructure evolution during laser additive manufacturing of a nickel-based superalloy," *Acta Materialia*, vol. 77, pp. 85–95, 2014.

[23] L. Nastac, "Numerical modeling of solidification morphologies and segregation patterns in cast dendritic alloys," *Acta Materialia*, vol. 47, no. 17, pp. 4253–4262, 1999.

[24] L. Nastac and D. M. Stefanescu, "Stochastic modelling of microstructure formation in solidification processes," *Modelling and Simulation in Materials Science and Engineering*, vol. 5, no. 4, p. 391, 1997.

[25] P. Promoppatum, S.-C. Yao, P. C. Pistorius, and A. D. Rollett, "A comprehensive comparison of the analytical and numerical prediction of the thermal

history and solidification microstructure of inconel 718 products made by laser powder-bed fusion," *Engineering*, vol. 3, no. 5, pp. 685–694, 2017.

[26] J. A. Dantzig and M. Rappaz, *Solidification: -Revised & Expanded*. EPFL press, 2016.

Chapter 5

Solidification process map of a Ti-Al-V-Fe alloy and its application to a wire arc additive manufacturing process: A phase field study

Complete Citation: Z. Li, M. Greenwood,J. Miranda, and A. Phillion. "Solidification process map of a Ti-Al-V-Fe alloy and its application to a wire arc additive manufacturing process: A phase field study". *to be Submitted to Acta Materiala*.

Solidification process map of a Ti-Al-V-Fe alloy and its application to a wire arc additive manufacturing process: A phase field study

Z. Li[1], M. Greenwood[1,2], J. Miranda[1],A.B. Phillion[1]

[1]*Department of Materials Science and Engineering, McMaster University, Hamilton, Canada*

[2]*Canmet MATERIALS, Natural Resources Canada, 183 Longwood Road south, Hamilton, ON, Canada*

Abstract:

Wire arc additive manufacturing (WAAM) exhibits significant potential for fabricating β-Ti alloys; however, the control of grain morphology poses a major challenge. In this study, we address this gap by employing a recently developed multi-component phase field model to study process-microstructure relations. We utilize this model to construct a solidification process map for a Ti-1Al-8V-5Fe (wt%) alloy and specifically to identify the conditions whereby columnar and equiaxed grain morphologies develop i.e. the Columnar-to-Equiaxed Transition. The solidification process map is established through a series of PF simulations conducted under constant temperature gradient and solidification rate conditions. Then, we use the map to understand the WAAM processing conditions under which columnar and equiaxed grains will form, and, crucially how different microstructure form as a function of build height. The model results from one set of processing conditions are validated against the results from a 10-layer Ti-185 thin wall built using WAAM. The model predicts that the CET occurred at the top of the Ti-185 thin wall, which agrees well with the experimental results, where the dominated microstructure transitions from an elongated columnar grains at the bottom to the equiaxed grains at the top as the solidification

proceed during the last layer deposition. The solidification process map, together with its validation via WAAM processing, demonstrate the use of multi-component phase field models to help improve microstructure during additive manufacturing of complex alloys.

Keyword: Wire arc additive manufacturing, Solidification process map, Columnar to equiaxed transition, Phase field model, Beta-Ti alloy

5.1 Introduction

Wire Arc Additive Manufacturing (WAAM) is an emerging technology that shows great potential for use in the aerospace industry. In the WAAM process, an electric arc serves as the heat source, while the metal wire acts as the feedstock [1, 2, 3]. This technique boasts a higher deposition rate and lower cost than other metal additive manufacturing technologies, making it well-suited for the production of large-scale metallic components [2, 3]. With its potential to significantly reduce production time and costs, WAAM presents an attractive alternative to conventional manufacturing methods [2].

The WAAM process has been successfully employed in the fabrication of a variety of structural alloys, with titanium alloys emerging as a particularly suitable candidate for this technique [2, 3]. Titanium alloys are highly sought after in industries such as aerospace and biomedical, owing to their excellent combination of properties, including high specific strength, low modulus, high service temperature, and exceptional corrosion resistance [2]. Despite these benefits, the use of titanium alloys has remained limited due to the high cost associated with conventional fabrication methods [2]. In particular, their low thermal conductivity, high chemical reactivity, and high deformation resistance make traditional machining or casting of these alloys prohibitively expensive [2]. By contrast, WAAM offers a cost-effective alternative, with lower equipment costs and reduced post-processing machining requirements, making it an attractive option for the cost-effective fabrication of titanium alloys.

Over the past two decades, the use of Additive Manufacturing (AM) for the fabrication of titanium components has increased significantly [2]. However, controlling grain morphology and achieving grain refinement remains significant challenges [1].

While WAAM allows for high deposition rates, it also results in a larger molten pool size, lower solidification rates, and high temperature gradients along the building direction. As a consequence, coarser β grains with a strong [001] direction texture form during the WAAM process, leading to anisotropic mechanical properties where the average yield and ultimate tensile strengths are higher along the longitudinal direction than in the transverse direction [1]. Given that most applications require uniform mechanical properties, achieving finer equiaxed grains is desirable.

The Columnar to Equiaxed Transition (CET) represents an important quantity in alloy systems, describing the processing conditions (temperature gradient G and solidification rate V) under which a largely equiaxed and refined grain morphology will form, instead of the problematic columnar one. In recent years, researchers have made significant efforts to quantify the CET in WAAM processing of Ti alloys. Martina [4] et al. achieved completely equiaxed Ti-64 grain structure by using a WAAM process that included a high pressure interpass rolling between printed layers. Wang et al. [5] found that the addition of a small amount of Ti–25V–15Cr–2Al–0.2C(wt%) powder during the WAAM fabrication process enabled the CET of Ti-64 components. When building a thin wall, they also found that the CET occurred at the wall's top where the temperature of the molten pool was higher. Tan et al. [6] studied the graded microstructure of a Ti-6Al-4V(wt%) alloy manufactured using another process, electron beam melting, and determined an optimal set of G and V to achieve CET. These examples of experiment-based studies provide numerous insights about CET during additive manufacturing of Ti alloys, but were also costly and confined to only a few basic alloy compositions and thermal conditions.

Modeling approaches provide a cheaper and more flexible alternative to experiments for studying CET [7]. CET models found within the literature can be classified as either deterministic or stochastic. The deterministic models directly give a prediction based on the calculations of analytical equations using averaged material quantities, while the stochastic models rely on numerical methods to provide a direct representation of the microstructure. A well-accepted deterministic CET model is the one developed by Hunt [8], where he defined a criterion that CET would occur if the fraction of equiaxed grains exceeded 0.66. Based on Hunt's criterion, a two-axis solidification process map diagram can be drawn with G on the vertical axis and V on the horizontal axis to show the regions where columnar grains dominate and conversely where equiaxed grains dominate the microstructure. This kind of deterministic model is helpful to identify the important parameters governing CET, but can only be applied on very restrictive conditions, i.e. simple domain geometry and boundary conditions, and constant material properties.

Stochastic models are able to overcome the shortcomings of deterministic models, by directly giving a picture of the expected microstructure. In the late 1980's, Brown et al. [9] performed a Monte Carlo simulation to study CET, and found that it occurred while the volume fraction of equiaxed grains ahead of the columnar interface was above 0.5. However, this method lacked a physical basis. At the same time, Rappaz et al. [10] developed the Cellular Automation (CA) technique to include the mechanisms of heterogeneous nucleation and dendrite tip growth kinetics. Recently, the CA technique has been applied to simulate microstructure development during the additive manufacturing processes. For example, Teferra et al. [11] simulated the laser powder bed fusion process of a 316L stainless steel via a optimized large 3-dimensional

cellular automata finite element model. However, the CA technique uses a coarse, discrete solid-fraction field to represent the solid-liquid interface. This method may lead to deviations in interface shape and growth behaviour [12] when simulating the fine microstructures. Thus, its predictions of CET during additive manufacturing - with high cooling rates and high solidification velocity - may be less accurate than desired.

Over the last 30 years, the Phase Field model has become a popular approach to study the solidification process during conventional casting and emerging AM processes as a result of its detailed description of the solid/liquid interface. In PF models, a field variable ϕ is used to represent the liquid phase ($\phi = -1$), the solid phase ($\phi = 1$) and the in-between state ($-1 < \phi < 1$), which will evolve itself along the direction of local free energy minimization. The PF models are widely used in free boundary problems [3] since they provide high detail of the interface shape without actually tracking the interface. Azizi et al. [13] performed a PF simulation to explore the influence of build direction on the microstructure evolution of dilute Al-Si alloy fabricated by laser powder bed fusion, and found that the nucleation rate and equiaxed to columnar grain ratio was higher in the horizontally built samples as compared to vertically build ones. This agreed with their experimental observations. Lenart et al. [7] simulated microstructure evolution of a Ni-based superalloy during directional solidification. They developed a solidification process map by performing a series of simulations over a range of G and V. However, the multi-component alloy was simplified to be a binary one using the pseudo binary approach [14].

In the present study, a multi-component phase field model [14, 15] has been utilized

to create a solidification process map for a high strength, low cost β-Ti alloy, Ti-1Al-8V-5Fe (wt%), and then coupled with FEA simulations of temperature evolution during the WAAM process in order to determine the constant G and V parameters within the WAAM processing space under which columnar and equiaxed grains will form.

5.2 Methods

The overall workflow of the research is as follows. First, the solidification process map for the Ti-185 alloy is created by performing a series of nineteen multi-component PF simulations under constant G and V. A multi-component PF model is needed since some elements (V, Fe) are positively segregating during solidification while others (Al) are negatively segregating. Second, a thermal FEA model simulating the WAAM of a ten-layer thin wall is created to determine the temperature evolution during the build process. Six different simulations were conducted considering different arc power and arc moving speed. G and V values for each layer during solidification are then extracted from the thermal FEA model, and compared to the solidification process map, in order to identify the position within the build that CET occurs. Third, the model results from one simulation are validated against experimental results from a thin-wall Ti-185 sample build via WAAM.

5.2.1 Phase Field Simulations

The multi-component PF model implemented in the present study was proposed by Provatas et al. [13, 15, 16, 17, 18]. The formulation of this model begins with a

quadratic description of the free energy of the solid and liquid phases,

$$F^{\theta}\left(c_1, c_2, ...c_n - 1\right) = \frac{1}{2}\sum_{i=1}^{n-1}\sum_{j=1}^{n-1} A_{ij}^{\theta}\left(c_i - \bar{c}_i^{\theta}\right)\left(c_j - \bar{c}_j^{\theta}\right) + \sum_{j=1}^{n-1} B_j^{\theta}\left(c_j - \bar{c}_j^{\theta}\right) + D^{\theta}, \quad (5.1)$$

where F^{θ} represents the free energy of phase θ, c_i and c_j are the concentration of component i and j, A_{ij}^{θ}, $\bar{c}_i^{\theta}$, B_j^{θ} and D^{θ} are fitting parameters. To get the fitting parameters, a data set $\{c_1, c_2, ..., c_{j-1}, F\}$ that contains a massive number of concentration/free energy data points was extracted from a thermodynamic database (e.g. Thermo-Calc), and then fit via a least square method. The fitting parameters are also used in the phase field equations.

Simulation of solidification via PF involves concurrently solving the diffusion of the solute elements within the model domain, as well as the evolution of the liquid and solid phases. These are expressed below, based on the free energy relaxation principle,

$$\tau(\vec{n})\frac{\partial\phi}{\partial t} = W_{\phi}(\vec{n})^2\nabla^2\phi + \phi - \phi^3 - (1-\phi^2)^2\left(\frac{(I-[K])^T}{2}\vec{U} + \hat{n}_c\right)^T [\lambda]\vec{U}, \quad (5.2)$$

and

$$[\chi]\frac{\partial\vec{\mu}}{\partial t} = \nabla\left[[M]\nabla\vec{\mu} + Wa(\phi)\,|\Delta\vec{c}_{eq}|\{\hat{n}_c + (I-[K])^T\vec{U}\}\frac{\partial\phi}{\partial t}\frac{\nabla\phi}{|\nabla\phi|}\right] + \frac{1}{2}|\Delta\vec{c}_{eq}|\{\hat{n}_c + (I-[K])^T\vec{U}\}\frac{\partial\phi}{\partial t}, \quad (5.3)$$

where ϕ is the order parameter, $\vec{\mu}$ is a vector representing the chemical potentials of each solute component μ_i, I is the identity matrix, and $[\chi^{\theta}]$ is the inverse matrix of

$[A^\theta]$ which composed of the free energy fitting parameters A^θ_{ij}. Please note that vector and matrix notation are used in the present paper to represent within the numerical algorithm a vertical column and multiple columns of numbers respectively, while the square brackets are used to represent the matrix form of the parameters, $\vec{n} \equiv \frac{\vec{\nabla}\phi}{|\vec{\nabla}\phi|}$ is the normal direction to the interface, $a_s(\vec{n})$ represents the 2D four-fold anisotropy, $W_\phi(\vec{n}) = W_0 a_s(\vec{n})$ sets the interface width [19], and

$$\left[\chi^\theta\right]^{-1}_{ij} = A^\theta_{ij}, \tag{5.4}$$

$$\vec{U} = \frac{\left[\chi^L\right]}{|\Delta\vec{c}_{eq}|}\left(\vec{\mu} - \vec{\mu}_{eq}\right), \tag{5.5}$$

$$\Delta\vec{c}_{eq} = \vec{c}^L_{eq} - \vec{c}^S_{eq}, \tag{5.6}$$

$$\hat{n}_c = \frac{\Delta\vec{c}_{eq}}{|\Delta\vec{c}_{eq}|}, \tag{5.7}$$

$$[K] = \left[\chi^L\right]^{-1}\left[\chi^S\right], \tag{5.8}$$

$$[\lambda] = \lambda_o \frac{|\Delta\vec{c}_{eq}|^2}{|\Delta\vec{c}_{eq,i}|^2}[\chi^L]^{-1}\chi^L_{ii}, \tag{5.9}$$

$$d_{0,i} = \frac{2\sigma_{SL}}{|\Delta\vec{c}_{eq,i}|^2}\chi_{ii} \tag{5.10}$$

$$\lambda_o = \frac{a_1 W_0}{d_{0,i}} \tag{5.11}$$

$$[\chi] = \left[\chi^L\right] \{I - (I - [K])\, h(\phi)\}, \tag{5.12}$$

$$[M] = q(\phi) \left[D^S\right] \left[\chi^S\right] + (1 - q(\phi)) \left[D^L\right] \left[\chi^L\right]. \tag{5.13}$$

Note that in this set of equations, $h(\phi)$ and $q(\phi)$ are the interpolation equations commonly used in PF models, $d_{0,i}$ is the capillary length of the ith component, λ_o is the coupling coefficient [20], $a_1 = 0.8839$ is a constant, σ_{SL} is the solid-liquid interface energy, $\left[D^\theta\right]$ is the diffusion coefficient matrix that is related to the physical properties of the alloy system, matrices $[K]$ and $\left[\chi^\theta\right]$ are related to the free energy surface given in Eq. 5.1, and $\mu_{eq,i}$, $c^L_{eq,i}$ and $c^S_{eq,i}$ represent the equilibrium chemical potential and the equilibrium concentration of the ith component in the liquid and solid phases. The last three terms, $\vec{\mu}_{eq}$, $\vec{c}^L_{eq}$ and c^S_{eq} all vary as a function of local temperature T; please refer [15] for the calculation methodology. Finally, the term $a_s(\vec{n})$ is calculated as

$$a_s(\vec{n}) = 1 + \epsilon_4 cos4(\theta + \theta_0), \tag{5.14}$$

where ϵ_4 is a material parameter characterizing the anisotropy strength, θ is the angle between the interface normal and pulling direction, and θ_0 is the misorientation angle between the preferred crystalline orientation and the global coordinate system [21].

In addition to the model described in [15], the model used in this study uses a nucleation module to take into account the formation of equiaxed grains. Assuming no solid grain movement, the nucleation probability P_n within an area $\Delta S = \Delta x^2$ at

a given time range Δt is calculated by [7, 22, 23]

$$P_n = -2\mu_N(\Delta T)\frac{\partial T}{\partial t}(1 - f_s)\Delta S\Delta t \tag{5.15}$$

where $\mu_N = 5 \times 10^5$ m^{-2}K^{-2} [23] is the nucleation possibility parameter, ΔT is the local undercooling i.e. the local temperature in comparison to the liquidus temperature, $\partial T/\partial t$ is the cooling rate, (1-f_s) is the local liquid fraction.

The PF model is numerically solved in 2D on a rectangular domain using the Finite Volume method using a bespoke c++ code. The adaptive mesh refinement algorithm developed by Greenwood et al. [16] was implemented to improve computational efficiency. The nucleation model, Eq. 5.15 is applied at each nodal point, at each 100 time steps, with the value of f_s being obtained from ϕ, and the value of Δx is assumed to be the local grid spacing. During this "nucleation check stage", a random number between 0 and 1 is generated at each nodal point, and compared with the value of P_n calculated at that point. Nucleation will occur if P_n is larger than that random number. Further details on the numerical implementation are given below.

5.2.2 Thermal FEA Simulations

The temperature evolution during the WAAM process is simulated using the commercial ABAQUS FEA code. The transient heat transfer analysis in the FEA model is governed by:

$$\rho c_p \frac{\partial T(x, y, z, t)}{\partial t} = -\nabla \cdot \vec{q}(x, y, z, t) + Q(x, y, z, t) \tag{5.16}$$

where ρ is the density, c_p represents the specific heat capacity under constant pressure, T is the local temperature, $\vec{q} = -k(T)\nabla T$ is the heat flux that results from the temperature gradient i.e. the heat conduction, $k(T)$ is the temperature dependent heat conductivity of the material, and $Q = Q_I - Q_R - Q_C - dH/dt$ where Q_I represents heat input from the wire arc, Q_R is the surface heat radiation, Q_C is the surface heat convection and dH/dt the latent heat.

The heat input from the wire arc, Q_I is simulated by a Gaussian distributed moving heat source, that is expressed as [24]

$$Q_I(x,y) = \frac{2\lambda P}{\pi r_0^2} exp\{\frac{-2[(x-x_0)^2 + (y-y_0)^2]}{r_0^2}\} \tag{5.17}$$

where λ is the absorptivity of the material, P is the arc power, r_0 is the arc radius and (x_0, y_0) is the position of the arc center that varies with time as a function of the laser scanning speed, v. The surface heat radiation Q_R and convection Q_C are given by

$$Q_R = \sigma\epsilon(T^4 - T_0^4), \tag{5.18}$$

and

$$Q_C = h(T - T_0), \tag{5.19}$$

where σ is the Stefan-Boltzmann constant, ϵ is the emissivity, T_0 is the ambient temperature, and h represents the heat convection coefficient.

5.2.3 Numerical Implementation

5.2.3.1 Phase Field Simulations

The solidification process map for the Ti-185 alloy was made by performing a series of nineteen uni-directional solidification scenarios via PF with different constant G and V values. For the initial condition, a 1-D temperature gradient of magnitude G is defined along the z-axis, with the temperature at the domain base set to $T_{bottom} = 1835$ K, and temperatures above the based determined via $T = T_{bottom} + Gz$. Note that for Ti-185, $T_L = 1848$ K and $T_S = 1703$ K thus the initial temperature is within the semi-solid region. Three nuclei, each with a different misorientation angle ($\theta_0 = 0°, 15°$ and 30°), were also placed at the domain base and with the same undercooling. For the boundary conditions, a periodic boundary condition was applied to the left and right sides while a zero Neumann boundary condition was applied to the top and bottom sides. During the simulation, the local temperature T evolves according to $T = T_{bottom} + G(z - Vt)$, where V is the solidification rate and t is the physical solidification time, i.e. the iteration number multiplied by the PF timestep multiplied by the relaxation time τ. The domain size for the solidification process map was set as 4096 $\times$ 4096 grid points, with a mesh spacing of $\Delta x = 0.8W_0$. The physical properties needed for the PF simulations are given in Table 5.1. Additional details for the nineteen simulations are listed in Table 5.2. Please note that different simulations have different mesh spacing, as a result of the length and time scales related to each of the G, V pair. It also should be noted that the chosen of the interface width W need to consider both accuracy and computational efficiency, based on the limit of microstructure tip radius and curvature.

Table 5.1: Simulation parameters used in the PF simulations [25][26]

PF parameters	Value
σ_{SL} (J/m^2)	0.0475
ϵ_4	0.05
D_L (m^2/s)	9.5E-9
D_S (m^2/s)	5.0E-13

Table 5.2: G, V, and the corresponding interface witdh W_0 for each of the nineteen simulations used to generate the solidification process map

case	G (K/m)	V_p (m/s)	W_0 (nm)
1,2	1000000	0.1,0.05	15,20
3,4	500000	0.1,0.05	20
5,6	100000	0.1,0.50	30
7,8	50000	0.1,0.05	50
9,10	10000	0.1,0.05	100,200
11,12	5000	0.1,0.05	100,200
13,14,15	2000	0.1,0.05,0.01	300
16,17,18,19	1000	0.1,0.05,0.01,0.001	400

The PF simulations were performed using 32 CPUs on the Digital Research Alliance of Canada, with each simulation requiring approximately seven days for completion. The thermodynamic free energy data for the Ti-alloy was extracted from the Thermo-Calc^{TM} TCTI 2 database, providing the necessary thermodynamic information for the simulation. To determine the temperature-dependent phase equilibrium of the Ti-185 alloy, a convex hull-based tool, which was previously introduced in our study [15], was utilized for calculation and analysis.

5.2.3.2 Thermal FEA Simulations

The thermal FEA simulation models the WAAM printing of a 10 layer Ti-185 thin wall, 72 mm in length, 6 mm in thickness and 12.8 mm in height built on top of a

Ti-185 substrate 96 mm in length, 30 mm in thickness and 88 mm in height. Fig 5.1 shows a schematic of the model domain, along with the boundary conditions and the mesh. The FEA domain is meshed with cuboid elements. In the thin wall, the mesh size is 1×1×0.64 mm; each printed layer consists of two layers of FEA elements. As for the substrate, two different mesh sizes are defined. A finer mesh 1× 1 × 0.8 mm is defined for the top 8 mm in contact with the printed layers, while a coarser mesh 1×1×8 mm is used for the bottom 80 mm. A fixed temperature $T = T_0 = 20\ ^{\circ}C$ is defined for the bottom of the substrate, while a zero flux boundary condition is defined for its four sides. A Gaussian distributed moving heat source in the form of Eq. 5.17 is used to simulate the heat input from the electric arc to the top of the printed layer during the WAAM process. Surface radiation ($\epsilon = 0.1$) and convection boundary conditions ($h = 10\ \mathrm{W/(m^2 \cdot K)}$ and $T_\infty = T_0$) are applied to the top and four side surfaces of the deposited layers. The temperature-dependent material properties (heat capacity, thermal conductivity, density, and latent heat) needed for the thermal FEA simulation are taken from Refs. [27, 28]. To simulate the multi-layers printing process during the WAAM process, a element death and birth method is applied, i.e. the elements of the deposited layers are deactivated before the deposition process begins, and the elements of the deposited wall are activated as the electric arc scans past them.

Table 5.3 shows the process parameters used for the six thermal FEA simulations. Cases 1, 2, and 3 consist of different arc powers P and travel speeds V_{arc} but keeping the heat density constant. Cases 2, 4, and 5 consist of the same V_{arc} but different P. These were chosen to explore the effect of heat density and travel speed on CET. Finally, case 6 represents the process conditions used in the model validation

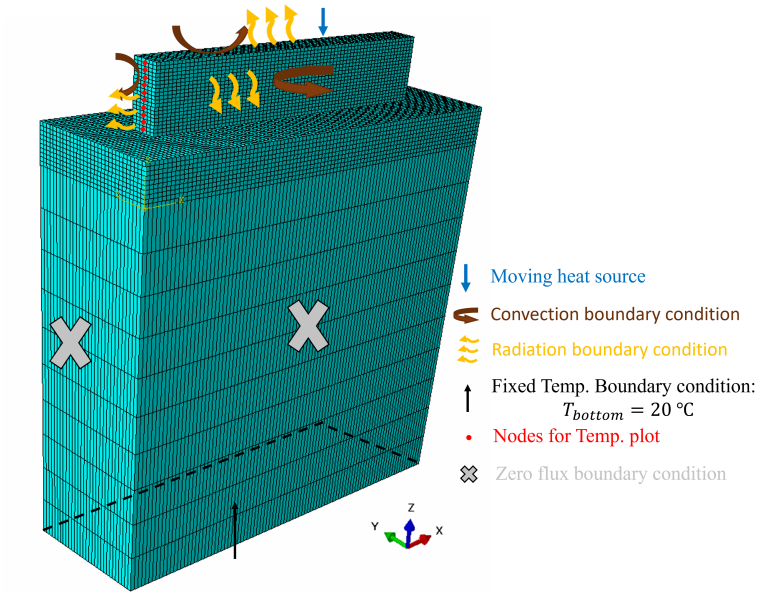

Figure 5.1: Mesh and boundary conditions for the thermal FEA simulation of the WAAM process. Please note that the convection and radiation boundary conditions are defined for all the four side surfaces of the printed layers, and the zero flux boundary conditions are defined for all the four side surfaces of the substrate

experiment. The process conditions varied from one layer to the next, and are not shown due to confidentiality reasons.

Table 5.3: Process parameters of WAAM-Ti185 alloy used in the finite element analysis

Case	P (W)	V_{arc} (mm/s)	P/V$_{Arc}(J/mm)$
1.	4800	6	800
2.	2400	3	800
3.	1200	1.5	800
4.	1200	3	400
5.	3000	3	1000
6.	Actual Experimental case		

5.3 Experimental Methods

In order to validate the PF and thermal FEA simulations, a 10-layers Ti-185 thin wall, 72 mm in length, 6 mm in thickness and 12.8 mm in height, was built on the top of a Ti-6Al-4V substrate, 96 mm in length, 30 mm in thickness and 88 mm in height, via WAAM. The thin wall was then removed from the substrate, and prepared for metallographic characterization using standard procedures.

5.4 Results and discussions

5.4.1 Phase Field Simulations and Creation of the Solidification Process Map

Figures 5.2 and 5.3 show two typical solute maps and the resulting grain morphologies obtained from the PF uni-directional solidification simulations, for Cases 1 and 16.

Fig. 5.2 shows a columnar dendrite structure, which formed under a thermal condition $G = 10^6$ K/m and $V = 0.1$ m/s. As can be seen, a columnar grain structure has formed - with primary, secondary, and tertiary arms - originating from the three initial seeds placed at the bottom of the domain. Nucleation has not occurred anywhere in the domain. Fig. 5.3 shows an equiaxed structure developed under a thermal condition $G = 10^3$ K/m and $V = 0.1$ m/s. As can be seen, a totally different microstructure with numerous equiaxed grains has developed. These equiaxed grains have nucleated in front of the columnar dendrite tips, blocking its growth. Comparing the images (a) and (b) in both figures, the occurrence of positive segregation of Fe to the liquid phase, and negative segregation of Al to the solid phase are evident. Such individual segregation maps are only possible using a multi-component PF model.

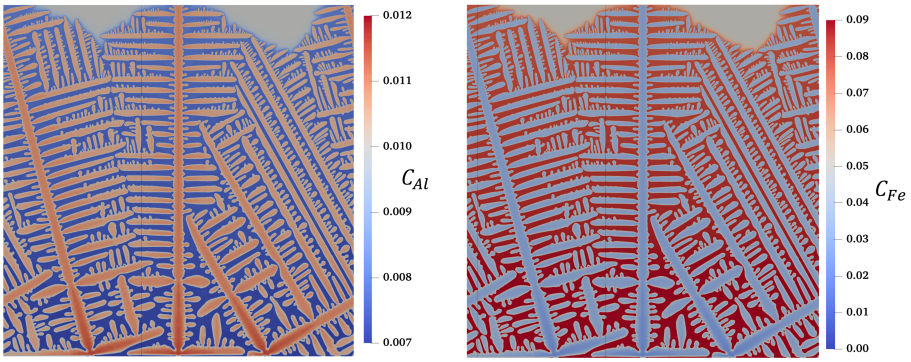

Figure 5.2: Solute distribution of (a) Al and (b) Fe, and the resulting grain morphology as predicted by the PF model for Case 1.

Fig. 5.4 shows a summary of all nineteen PF simulations for the Ti-185 alloy, plotted in V vs G space. In this chart, each blue triangle represents one PF simulation where the final/dominant structure was columnar, i.e. where nucleation did not happen or occurred only a few times but did not block the columnar dendrite growth. Further, each orange cross a PF simulation where the final structure was equiaxed.

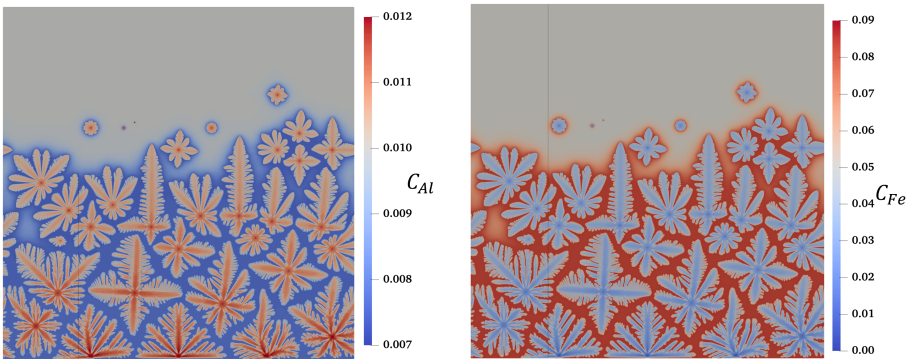

Figure 5.3: Solute distribution of (a) Al and (b) Fe, and the resulting grain morphology as predicted by the PF model for Case 16.

As can be seen, equiaxed microstructures tend to form at the top left section of the image, i.e. where G is smaller while V is larger, whereas columnar microstructure dominate other regions. Thus, a clear demarkation between the two microstrutures, i.e. the Columnar-to Equiaxed Transition, is visible.

Besides the numerical PF models, Hunt et al. also developed a well-accepted analytical approach to predict the CET during directional solidification processes. Hunt's approach can be expressed using as [7, 8]:

$$\frac{G^n}{V} = a[\frac{1}{n+1}(\frac{-4\pi N_0}{9ln(1-g_{equ})})^{1/3}]^n \tag{5.20}$$

where N_0 is the nuclei density, a, n are material dependent parameters calculated from an empirical relationship $\Delta T = (aV)^{1/n}$, ΔT is the undercooling of the columnar dendrite tip, g_{equ} is the volume fraction of equiaxed grains. Hunt considered that $g_{equ} < 0.0066$ represented a fully columnar state and $g_{equ} > 0.66$ a fully equiaxed state.

Figure 5.4 also plots the CET transition using Hunt's analytical approach. Ideally

it would have been beneficial to predict the CET transition for the Ti-185 alloy, however, there is a lack of essential parameters such as N_0 for applying Hunt's model for the Ti systems. Consequently, the plot shows Hunt's analytical predictions (orange and blue lines) as a reference for the Inconel 718 alloy system. For this Inconel 718 alloy, $a = 4.5$ K^{2}s/m, $n = 2$, and $N_0 = 2.65 \times 10^{14}$ m^{-3} [7, 8], while for Ti-185 alloy the material properties we can get is $n = 1.82$ from our previous work, as calculated from the results in Fig. 3.9. As can be seen, the PF simulation and the analytical model predict the same trends of CET, i.e. equiaxed microstructures tend to form at the top left section of the image where G is smaller while V is larger. Further, nearly the same slope of the boundary between columnar and equiaxed region is observed, but the analytical model is shifted to one order of magnitude larger in G for a given V. The similar slope of the boundary between columnar and equiaxed region results from the similar material parameter n for Inconel 718 alloy and Ti-185 alloy in the log-scale plot, while the differences may result from other different materials dependent parameters. Nucleation is a highly random event that is strongly influenced by local undercooling, the availability of nucleation sites, and nucleation time. For a steady-state directional solidification scenario, equiaxed grain nucleation occurs between the liquidus isotherm and the columnar dendrite tips – the length of which is inversely proportional to G. So, a low G means a large area in front of the columnar dendrite tips where the nucleation can occur. V has a positive correlation with the dendrite tip undercooling under steady state growth, which means that a larger V requires the columnar dendrite tips to remain in a higher under-cooled region [8, 29, 30, 31]. Further, at larger V, the available liquid between the dendrite tips and the liquidus isotherm will be larger, and the local thermal undercooling will also be larger, both

accelerating equiaxed grain nucleation.

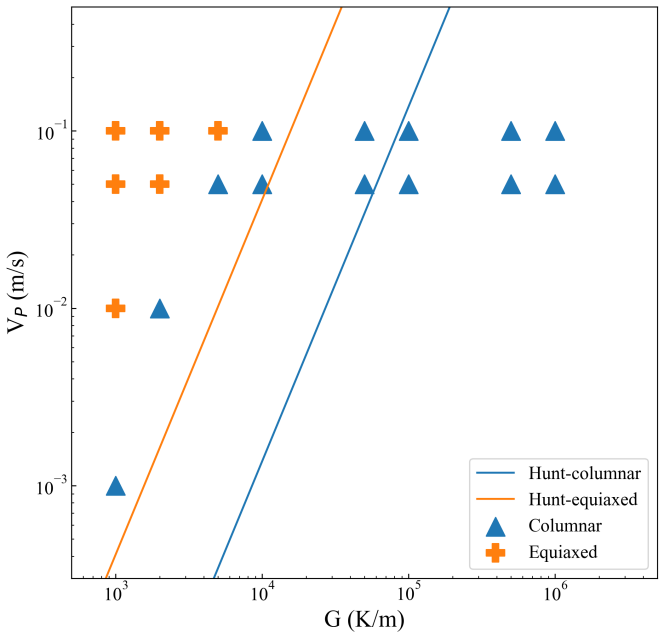

Figure 5.4: Solidification process map for the 19 PF simulation results, showing the Columnar to Equiaxed Transition. Hunt's analytical model for the CET is also plotted for a Ni-based superalloy [7, 8]

5.4.2 Thermal FEA Simulations

Fig. 5.5 shows the predicted temperature distribution and the melt pool geometry when depositing Layer 10 of the Ti-185 thin wall for Case 6, as an example result from the thermal FEA simulation. The contour lines are given such that grey indicates temperatures greater than $T_L = 1575\ ^\circ C$, while red indicates the mushy zone, $T_L(1575^\circ C) > T > T_S(1430^\circ C)$. As can be seen, when printing this layer the WAAM process has influence the temperature of the entire part: the previously deposited

layers as well as the substrate. The melt pool consists on not only Layer 10 but in fact five layers from Layer 6 to Layer 10. Layer 5 is in the mushy zone. The temperature of the substrate has risen to over 100 °C from the initial ambient temperature $T_0 = 20°\text{C}$.

Fig. 5.6(a) shows the thermal history of all ten layers during printing and cooling of Layer 10, with Fig. 5.6(b) showing an inset view near the mushy zone. The data was taken from the front of the build, as shown by the red dots in Fig. 5.1 As can be seen, temperatures within all the layers experienced a first rapidly increase and then a slow decrease as the wire arc move further away. Layers 6 - 10 indeed exceed T_L, Layer 5 reaches a temperature within the mushy zone, while Layers 1-4 do not experience remelting. The effect of the latent heat can be seen by the change in slope of the temperature evolution during the cooling process, i.e. the cooling rate decreases as for temperatures between the liquidus and solidus. Please note that the initial temperature of Layer 10 is 20 $°C$ since this element is activated at $t = 0$. The initial temperatures of the other layers begin at $\approx 270°C$ as a results of the heat accumulation from the prior layer deposition.

5.4.3 Assessing the Influence of WAAM process parameters on the Columnar to Equiaxed Transition

From Section 5.4.1, the research has produced a solidification process map showing CET for a range of G and V values representative of additive manufacturing. From Section 5.4.2, the research has produced a thermal model that can provide the relevant G and V values for the WAAM process. In this section, the two are combined to

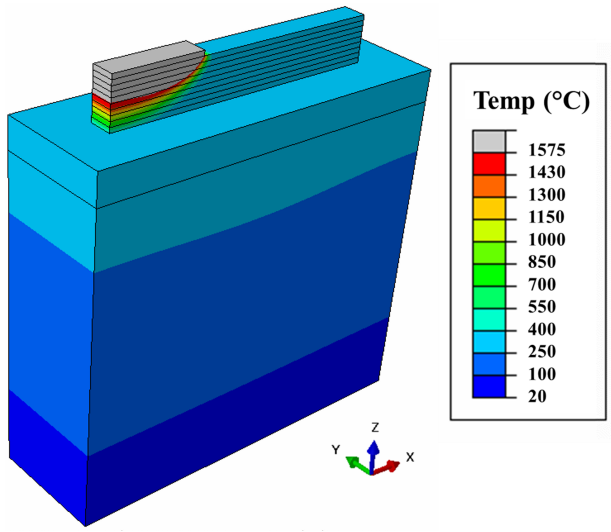

Figure 5.5: A snapshot of the temperature distribution when printing the 10^{th} layer of the thin wall during WAAM process

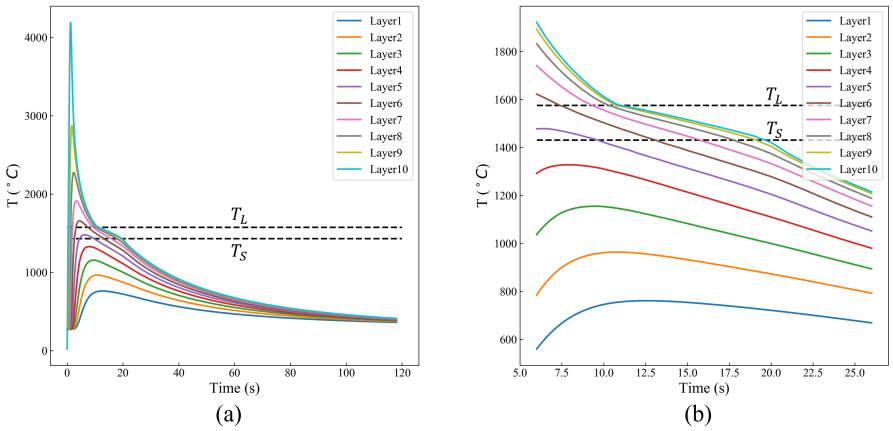

Figure 5.6: Simulated thermal history of all ten layers during deposition and cooling of Layer 10 of the Ti-185 thin wall. Figures (a,b) shows an over-all view and mushy zone inset view, respectively. The data for these curves was taken from the front of the built, as shown by the red dots in Fig. 5.1.

predict CET during WAAM processing. The challenge is that during additive manufacturing, G and V evolve with time layer-by-layer as the local thermal conditions change.

To extract G and V from the thermal FEA simulations, a method is adopted to calculate the local and transient G and V within the semi-solid region during the deposition of Layer 10. Only Layer 10, i.e. the last layer built, is used since the repeated layer by layer deposition process destroys the previous microstructure. In this method, which builds on and extends a method proposed by [13], G in the mushy zone is simplified to $G(z)$, a reasonable assumption according to Fig. 5.5, and is calculated as:

$$G_z(z,t) = \frac{T(z+\Delta z,t) - T(z-\Delta z,t)}{2\Delta z} \tag{5.21}$$

where $G_z(z,t)$ is the temperature gradient along the z direction, t is time, and $\Delta z =$ 0.64 mm is the meshing spacing along the z direction. The values for G_z are only calculated at nodal locations of the thermal FEA simulation. Further, they are only calculated when the temperatures are within the mushy zone, i.e. $(T_S < T(z + \Delta z,t), T(z-\Delta z,t) < T_L$. Similarly, V is calculated as:

$$V = C_R/G_z \tag{5.22}$$

where C_R is the cooling rate that is given by:

$$C_R(z,t) = \frac{T(z,t+\Delta t) - T(z,t-\Delta t)}{2\Delta t} \tag{5.23}$$

where Δt is the time step in the thermal FEA simulation, $T(z,t+\Delta t)$ and $T(z,t-\Delta t)$ are the temperatures at the coordinate z at the prior and next time step. Once again,

these values are only taken if the temperatures fall within the mushy zone. The application of Eqs. 5.21 - 5.23 results in the generation of ≈700 G and V pairs for each of the 6 thermal FEA simulations.

Fig. 5.7 shows the calculated G and V pairs for for one simulation, Case 6, along with the data from the solidification process map. As can be seen, most of the WAAM thermal conditions are located near a straight line start beginning near $G, V = (10^5, 10^{-4})$ at the base of the melt pool (Layers 6 and 7), and ending at $(10^3, 10^{-2})$ at the top of the melt pool (Layer 10). As expected, the temperature gradient gradually decrease during the WAAM process and the solidification rate gradually increase as the solidification proceed from the bottom to the top of the molten pool. However, it is not perfectly linear, with some deviations owing to the complex cooling condition inherent to the WAAM process. In terms of the CET transition, the combination of the solidification process map and the (G, V) pairs show that the microstructure is predicted to be columnar in Layers 6 to 9, and transformed to equiaxed in Layer 10.

Table 5.4 shows a summary for the other five WAAM process conditions. In Table 5.4, the molten pool depth, and the layer where CET occurs under each WAAM process parameters are indicated. In comparing Cases 1, 2 and 3, having equal heat density, a similar molten pool depth of ≈ 8.8 mm and a similar CET occurrance position, in Layer 10, were predicted. In comparing Cases 2, 4 and 5, having the the same arc traveling speed but with different arc power, the molten pool depth shows a clear increasing trend with increasing heat input density. For Case 4, with the lowest heat input density, the melt pool depth was only 4.3 mm, and no CET. For Case 5, with the highest heat input density, the melt pool depth was 10.3 mm, and CET

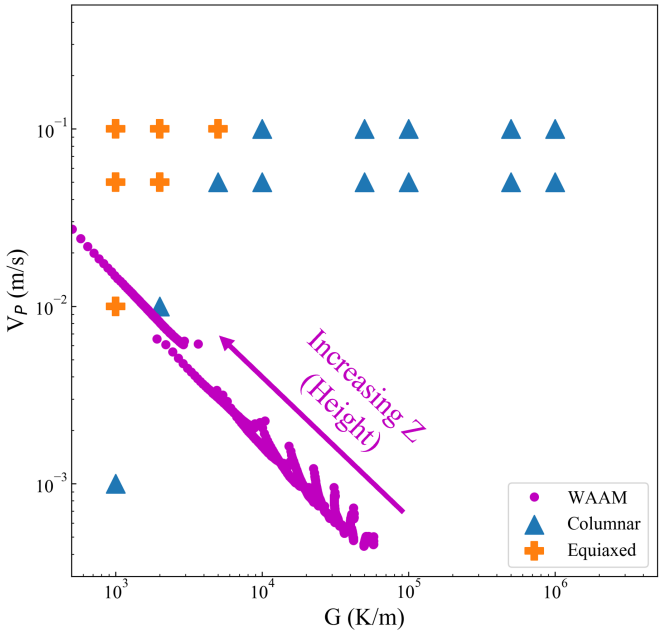

Figure 5.7: Solidification process map to show PF simulation results, and the position of the WAAM thermal conditions in the solidification process map

occurred at a position corresponding to Layer 9 and not Layer 10.

A detailed analysis of all the (G, V) pairs showed that the maximum G was similar for all cases when printing Layer 10, at $\approx$ 100 000 K/m, near the base of the melt pool. However as a result of the differing molten pool depths, the G values at the top of the melt pool were totally different. For example, $G_{min} \approx$ -1200 K/m in Case 5 while $G_{min} \approx$ 5000 K/m in Case 4. Thus, different CET conditions are predicted to occur for these different WAAM processing conditions.

Table 5.4: Thermal conditions and CET transition in different WAAM process

Case	Molten pool depth (mm)	CET
1.	8.8	Layer 10
2.	9.0	Layer 10
3.	8.6	Layer 10
4.	4.3	None
5.	10.3	Layer 9

5.4.4 Model Validation

Both the PF model of solidification of Ti-185 and the corresponding CET Solidification Process Map, as well as the thermal FEA simulation require validation. The melt pool depth is one metric that has been widely used to validate the accuracy of FEA models for additive manufacturing, e.g. [24]. The thermal FEA simulation of the WAAM process for Case 6, matching the experiment, shows that Layers 6 to 9 undergo remelting and re-solidification during the printing of Layer 10. In Fig. 5.8, a comparison is made of the maximum size of the predicted melt pool depth, against a low-resolution side-view micrograph of the experimentally-built WAAM thin wall sample containing all ten layers. Beginning with the micrograph on the right hand

side, two different regions can be seen–a top part that is light grey, and a bottom part that is dark grey/brown–with a clear boundary between the two. This boundary represents the boundary between the melt pool and the heat affected zone during the printing of Layer 10. SEM/EBSD identified the the top part to be purely the β phase, while the bottom part to be combination of the β and α phases. The depth of the melt pool was measured to be 7.36 mm. Turning to the model predictions on the left hand side, the liquidus isotherm was found to be at 6.07 mm, while the solidus isotherm to be at 7.09 mm. Thus, an excellent agreement between the experimentally-identified melt pool depth and the predicted location of the solidus isotherm can be seen, deviating by only about 0.27 mm or 3.7%. The minor deviation may result for a few reasons: the material properties used in the model, the use of a cuboid geometry for the simulation, and the model boundary conditions.

The microstructure itself obtained from the experiment is one metric that can be used to validate the CET solidification process map. Fig. 5.9 shows a micrograph of the side surface of the WAAM fabricated sample, showing in (a) the grain boundaries and grain morphologies, and in (b) and (c) higher-resolution images from a location near the top and base of the melt pool. As can be seen in (a), the micrograph exhibits a heterogeneous microstructure with a diverse distribution of grains. The absence of a dendritic structure is notable, with irregularly shaped grains scattered throughout the melt pool. Some grains appear elongated and large in size, while others exhibit a smaller circular morphology. At higher resolution, the micrograph for the top of the melt pool and shown in Fig. 5.9(b) reveals a predominance of small grains characterized by circular, hexagonal, rectangular, or some irregular shapes. These grains are numerous, indicating a high local grain density. In contrast, the micrograph

for the bottom of the melt pool and shown in Fig. 5.9(c) displays a distinct pattern of elongated grains, beginning on the lower right and moving to the upper left. Small grains are less prevalent compared to Fig. 5.9(b) suggesting a lower grain density and a different growth behavior in this specific area. These observed variations are a result of variations in the thermal conditions during the WAAM processing. Specifically, the decrease in G along with the increase in V from the bottom of the melt pool to its top lead to greater undercooling thus accelerating grain nucleation and the formation of a fine grain structure. Turning to the model predictions, in Fig. 5.7, the solidification process map shows that CET for the conditions seen in Case 6 would occur somewhere towards the base of the Layer 10. Although the micrographs are not conclusive, they do provide some evidence that a columnar to equiaxed transition is likely to have occurred in the upper one-third of the melt pool i.e. in Layer 9 or Layer 10. The main difference between the experimental observations and the model is that, in the experiments, there is a gradual transition from the large elongated grain dominated structure seen in Fig. 5.9(c) to the smaller rectangular and circular grain dominated structure in Fig. 5.9(b). The difference may be the result of the fact that, in the WAAM process, the thermal conditions continually change whereas in the PF model to create the solidification process map a constant G and a constant V are utilized.

5.5 Conclusions

Wire Arc Additive Manufacturing shows great potential for the application of AM to fabricating large metallic components, but the control of grain morphology remains a challenge. To fill this gap, a multi-component PF model has been used in this study

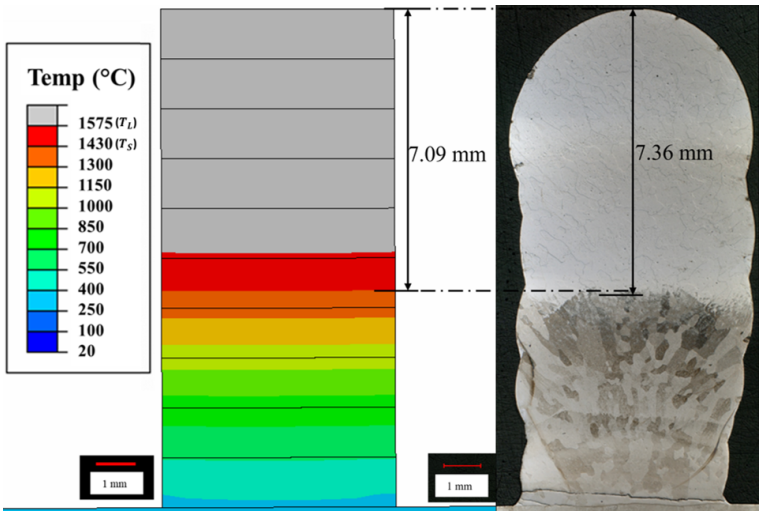

Figure 5.8: LHS: A cross-section view of the temperature distribution predicted by the thermal FEA model when printing Layer 10. RHS: A low-resolution side-view micrograph of the experimentally-built, via WAAM, thin wall sample

to create a solidification process map for the Ti-185 Fe-containing β-Ti alloy. This new solidification process map was then applied to examine columnar-to-equiaxed transition when fabricating Layer 10 of a 10-layer Ti-185 thin wall via WAAM. Five different processing conditions, simulated via FEA, were investigated. The PF and thermal FEA models were validated against experimental data, the melt pool depth as well as the CET.

The main findings are as follows:

1. The phase-field-developed Solidification Process Map shows that equiaxed grain tends to nucleate in regions of low G but at high V, as expected. Although Hunt's analytical model provides a good qualitative prediction, it is off by about one order of magnitude. The developed map also compares well, qualitatively, to experiments.

2. The thermal FEA simulations of the building of a Ti-185 thin wall via WAAM

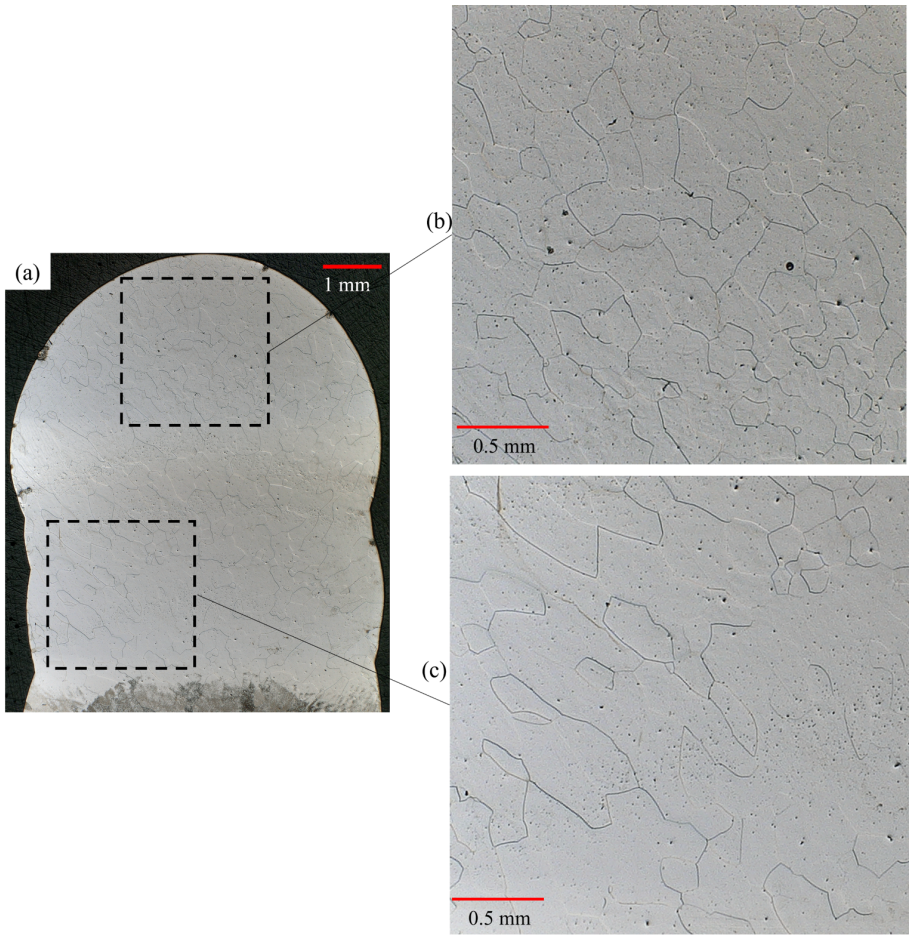

Figure 5.9: (a) A low-resolution micrograph shring the overall grain structure of the WAAM fabricated Ti-185 sample, (b,c) higher-resolution micrographs showing the top and bottom zones within the melt pool. Please note that the arc travel direction is into the page

show that G gradually decreases, while V gradually increases, from the bottom of the melt pool to the top. These simulations also show that the melt pool depth increases with increased heat input density (Cases 2,4,5), but does not change significantly for a constant heat input density but with different arc power and arc traveling speed (Cases 1,2,3).

3. The application of the solidification process map to the WAAM process predicts that the CET tends to occur at the top section of the molten pool irrespective of the applied process parameters. Additionally, the heat input density largely influence the occurrence of CET, i.e. a low heat input density may result the disappearance of CET while a high energy density cause the occurrence of CET at a lower position.

4. An excellent quantitative agreement is found between the melt pool depth predicted by the thermal FEA simulation and the experimental data, with a deviation less than 4%. Although it was not possible to conclusively validate the CET via the experimental data, qualitative agreement was shown in that the model predicted that CET would occur towards the base of Layer 10, while the experimental data shows the a transition in the upper one-third region from larger elongated grains to a smaller circular and hexagonal dominated structures.

5.6 Acknowledgement

ZL and AP acknowledge the funding provided by the Natural Sciences and Engineering Council of Canada, the Ontario Centre for Innovation, and Collins Aerospace in support of this research. MG acknowledges funding provided the Natural Resources

Canada's Office of Energy Research and Development (OERD).

References

[1] J. Wang, X. Lin, J. Wang, H. Yang, Y. Zhou, C. Wang, Q. Li, and W. Huang, "Grain morphology evolution and texture characterization of wire and arc additive manufactured ti-6al-4v," *Journal of Alloys and Compounds*, vol. 768, pp. 97–113, 2018.

[2] Z. Lin, K. Song, and X. Yu, "A review on wire and arc additive manufacturing of titanium alloy," *Journal of Manufacturing Processes*, vol. 70, pp. 24–45, 2021.

[3] J. Li, X. Zhou, M. Brochu, N. Provatas, and Y. F. Zhao, "Solidification microstructure simulation of ti-6al-4v in metal additive manufacturing: A review," *Additive Manufacturing*, vol. 31, p. 100989, 2020.

[4] F. Martina, S. W. Williams, and P. Colegrove, "Improved microstructure and increased mechanical properties of additive manufacture produced ti-6al-4v by interpass cold rolling," in *2013 International Solid Freeform Fabrication Symposium*, University of Texas at Austin, 2013.

[5] F. Wang, J. Mei, and X. Wu, "Microstructure study of direct laser fabricated ti alloys using powder and wire," *Applied Surface Science*, vol. 253, no. 3, pp. 1424–1430, 2006.

[6] T. Hua, C. Jing, Z. Fengying, L. Xin, and H. Weidong, "Microstructure and mechanical properties of laser solid formed ti-6al-4v from blended elemental powders," *Rare Metal Materials and Engineering*, vol. 38, no. 4, pp. 574–578, 2009.

[7] R. Lenart and M. Eshraghi, "Modeling columnar to equiaxed transition in directional solidification of inconel 718 alloy," *Computational Materials Science*, vol. 172, p. 109374, 2020.

[8] J. D. Hunt, "Steady state columnar and equiaxed growth of dendrites and eutectic," *Materials science and engineering*, vol. 65, no. 1, pp. 75–83, 1984.

[9] S. Brown and J. Spittle, "Computer simulation of grain growth and macrostructure development during solidification," *Materials science and technology*, vol. 5, no. 4, pp. 362–368, 1989.

[10] M. Rappaz and C.-A. Gandin, "Probabilistic modelling of microstructure formation in solidification processes," *Acta metallurgica et materialia*, vol. 41, no. 2, pp. 345–360, 1993.

[11] K. Teferra and D. J. Rowenhorst, "Optimizing the cellular automata finite element model for additive manufacturing to simulate large microstructures," *Acta Materialia*, vol. 213, p. 116930, 2021.

[12] A. Choudhury, K. Reuther, E. Wesner, A. August, B. Nestler, and M. Rettenmayr, "Comparison of phase-field and cellular automaton models for dendritic solidification in al–cu alloy," *Computational Materials Science*, vol. 55, pp. 263–268, 2012.

[13] H. Azizi, A. Ebrahimi, N. Ofori-Opoku, M. Greenwood, N. Provatas, and M. Mohammadi, "Characterizing the microstructural effect of build direction during solidification of laser-powder bed fusion of al-si alloys in the dilute limit: a phase-field study," *Acta Materialia*, vol. 214, p. 116983, 2021.

[14] Z. Li, M. Greenwood, and A. Phillion, "A phase field methodology for simulating the microstructure evolution during laser powder bed fusion in-situ alloying process," in *IOP Conference Series: Materials Science and Engineering*, vol. 1281, p. 012017, IOP Publishing, 2023.

[15] Z. Li, M. Greenwood, and A. Phillion, "Fast prediction of phase equilibrium at varying temperatures for use in multi-component phase field models," *Computational Materials Science*, vol. 206, p. 111251, 2022.

[16] M. Greenwood, K. Shampur, N. Ofori-Opoku, T. Pinomaa, L. Wang, S. Gurevich, and N. Provatas, "Quantitative 3d phase field modelling of solidification using next-generation adaptive mesh refinement," *Computational Materials Science*, vol. 142, pp. 153–171, 2018.

[17] K. Shampur, "A grand potential based multi-phase field model for alloy solidification," Master's thesis, McGill University, 2017.

[18] Z. Li, M. Greenwood, and A. Phillion, "A quantitative comparison between pseudo-binary and multi-component phase field models," *Computational Materials Science*, vol. 222, p. 112101, 2023.

[19] N. Provatas and K. Elder, *Phase-field methods in materials science and engineering*. John Wiley & Sons, 2011.

[20] V. Fallah, M. Amoorezaei, N. Provatas, S. Corbin, and A. Khajepour, "Phase-field simulation of solidification morphology in laser powder deposition of ti–nb alloys," *Acta Materialia*, vol. 60, no. 4, pp. 1633–1646, 2012.

[21] M. Gaoyang, X. Lingda, W. Chunming, J. Ping, and Z. Guoli, "Two-dimensional phase-field simulations of competitive dendritic growth during laser welding," *Materials & Design*, vol. 181, p. 107980, 2019.

[22] P. Nie, O. Ojo, and Z. Li, "Numerical modeling of microstructure evolution during laser additive manufacturing of a nickel-based superalloy," *Acta Materialia*, vol. 77, pp. 85–95, 2014.

[23] L. Nastac, "Numerical modeling of solidification morphologies and segregation patterns in cast dendritic alloys," *Acta Materialia*, vol. 47, no. 17, pp. 4253–4262, 1999.

[24] P. Promoppatum, S.-C. Yao, P. C. Pistorius, and A. D. Rollett, "A comprehensive comparison of the analytical and numerical prediction of the thermal history and solidification microstructure of inconel 718 products made by laser powder-bed fusion," *Engineering*, vol. 3, no. 5, pp. 685–694, 2017.

[25] S. Sahoo and K. Chou, "Phase-field simulation of microstructure evolution of ti–6al–4v in electron beam additive manufacturing process," *Additive manufacturing*, vol. 9, pp. 14–24, 2016.

[26] W. Sun, R. Yan, Y. Zhang, H. Dong, and T. Jing, "Gpu-accelerated three-dimensional large-scale simulation of dendrite growth for ti6al4v alloy based on multi-component phase-field model," *Computational Materials Science*, vol. 160, pp. 149–158, 2019.

[27] F. F. Ahmed, S. J. Clark, C. L. A. Leung, L. Stanger, J. Willmott, S. Marussi, V. Honkimaki, N. Haynes, H. S. Zurob, P. D. Lee, *et al.*, "Achieving homogeneity

in a high-fe β-ti alloy laser-printed from blended elemental powders," *Materials & Design*, vol. 210, p. 110072, 2021.

[28] H. Azizi, H. Zurob, B. Bose, S. R. Ghiaasiaan, X. Wang, S. Coulson, V. Duz, and A. Phillion, "Additive manufacturing of a novel ti-al-v-fe alloy using selective laser melting," *Additive Manufacturing*, vol. 21, pp. 529–535, 2018.

[29] J. Kundin, L. Mushongera, and H. Emmerich, "Phase-field modeling of microstructure formation during rapid solidification in inconel 718 superalloy," *Acta Materialia*, vol. 95, pp. 343–356, 2015.

[30] A. Karma and W.-J. Rappel, "Quantitative phase-field modeling of dendritic growth in two and three dimensions," *Physical review E*, vol. 57, no. 4, p. 4323, 1998.

[31] D. A. Kessler, J. Koplik, and H. Levine, "Geometrical models of interface evolution. iii. theory of dendritic growth," *Physical Review A*, vol. 31, no. 3, p. 1712, 1985.

Chapter 6

Conclusions and Summary

6.1 Summary and Conclusive remarks

Additive Manufacturing (AM) has witnessed remarkable growth and development over the past three decades, owing to its unique capability of fabricating intricate components directly and minimizing the materials waste that is inherent in conventional machining processes. This has led to the widespread application of AM in high-value-add industries including aerospace and biomedical where the production of customized products is highly desirable. However, ensuring precise control over product quality has emerged as a primary challenge, impeding the broader adoption of AM. Experimental investigations have revealed the formation of coarser columnar grains during the AM process, resulting in heterogeneous mechanical properties and the development of strong solidification textures. Furthermore, the utilization of diverse energy sources and powder feeding approaches further complicates the establishment of a robust process-microstructure-property relationship. To address these

challenges, phase field modeling has emerged as a valuable tool, enabling the exploration of microstructure evolution while reducing experimental time and costs. In this thesis, a multi-component phase field model has been developed to investigate the intricate microstructural evolution during laser powder bed fusion and wire arc additive manufacturing processes, with a specific focus on Ti-1Al-8V-5Fe (wt%), a cost-effective Beta-Ti alloy. Additionally, the accuracy of the multi-component phase field model has been systematically verified against Thermo-Calc calculations and other pseudo-binary models, with further validation achieved through comparison with experimental results.

This thesis begins with the introduction of a new phase equilibrium calculation method used in the multi-component phase field models. The calculation of phase equilibrium is a key section of a multi-component PF model as it influences both the accuracy and computational efficiency. In this thesis, a parabolic representation for the free energy is adopted, and the convex hull method is used to solve the phase equilibrium at single temperatures, while the temperature dependence of the phase equilibrium is calculated via a set of concise linear equations. The new phase equilibrium prediction method provides higher computational efficiency because the time-consuming phase equilibrium calculation is finished prior to the PF simulation, and concurrently higher computational accuracy, because the full local phase equilibrium is calculated. Then, a 1-D PF model is developed to simulate the solidification of the Ti-185 alloy using the new equilibrium calculation method under isothermal and continuous cooling conditions. The accuracy of the new approach is demonstrated by comparing calculation results with the commercial software Thermo-Calc. The results show that this new approach can achieve a high accuracy of equilibrium prediction

at single and multiple temperatures, and the 1-D PF model of the solidification is verified.

Then, the 2-D multi-component PF model is verified by performing a benchmark analysis to compare against two pseudo-binary phase-field models for multi-component alloy solidification. This is the first benchmark analysis among different models regarding to the solidification of multi-component alloys. In this benchmark analysis, the first pseudo-binary PF model is a common approach based on the model of Karma et al. [1], while the second pseudo-binary PF model and the multi-component model are implemented based on the grand potential model of Provatas et al. [2]. The three models were applied on the solidification of Ti-185 alloy under isothermal and directional solidification scenarios. The results show that a similar microstructure is predicted by the three models, and a further quantitative analysis shows that the dendrite tip velocity shows an excellent agreement. The highlight of the multi-component PF model is that it can predict both the positive segregation of V and Fe, and the negative segregation of Al during the solidification of Ti-185 alloy. Additionally, more side branches and secondary arms tend to form in the MC models when compared with the two pseudo-binary models, which may highlight the importance of MC model in providing more potential tie-lines.

The multi-component PF model is then applied to the laser powder bed fusion in situ alloying process. The use of elemental powder in LPBF provides more flexibility in materials design, but the in situ alloying process makes it even more difficult to construct the process-microstructure-property relationship. The multi-component PF model is applied to compare the use of pre-alloyed powder and elemental powder during LPBF processing. The PF simulation during LPBF of Ti-185 using pre-alloyed

powders shows that evenly distributed columnar dendrites form during the LPBF process. The results also show that nucleation influences the competitive growth, i.e. the grain with crystal orientation aligned to the build direction shows a considerable growth advantage, while nucleation is observed to occur above the "inclined grains", which block the growth of inclined dendrites. For the LPBF using elemental powder, the results show that the regions enriched in Fe significantly impede dendrite growth, while regions enriched in Al and V also slow dendrite growth though not as significantly. This results in complete alloying not being achieved during a single layer deposition process, but, as shown by prior experiment, requiring subsequent reheating cycles.

Finally, the multi-component PF model is applied to create a Solidification Process Map (SPM) for the Ti-185 alloy processed via Wire Arc Additive Manufacturing (WAAM). The Columnar to Equiaxed Transition (CET) is a major topic within the fields of AM, as the formation of coarser columnar grain during AM is unfavoured for most applications. A series of simulations using the multi-component PF model were performed under constant temperature gradient and solidification rate in order to determine the thermal conditions under which the columnar and/or equiaxed structures are favoured to form. The SPM was then applied on the WAAM process. The thermal history during the WAAM is simulated via a Finite Element thermal Analysis (FEA). The FEA results are validated by comparing the predicted molten pool depth with experiment. Then, the SPM predictions are compared with experimental observation for the validation. The SPM predicts a CET transition would occur at the top of the molten pool, which shows an excellent agreement with experiment results, where the elongated columnar grain at the bottom of the domain transit to small circular and

rectangular grain at the top.

6.2 Limitations and future work

The limitations of this study, along with some potential future works to the present findings can be listed as follows:

1. The phase equilibrium calculator: The limitation is the several simplifying assumptions for the use of the linear equations to calculate phase equilibrium at varying temperatures. For example, one assumptions is that the influence of temperature on the free energy curves is negligible when compared with concentration. This is true when the temperature difference between reference temperature and local temperature is small, but the prediction deviation may increase as the temperature deviate from the reference temperature. One possible approach to resolve that is using multiple reference temperatures. For the temperature point between the reference temperatures, linear shape function can be used to interpolate the equilibrium status. Another possible approach is to using a totally different approach, the machine learning method, to calculate the phase equilibrium.

2. The phase field model: The first limitation is that the fluid flow is not considered in the current model. The fluid flow may influence the concentration distribution and the undercooling for nucleation and dendrite growth. However, the challenge for the including of fluid flow includes high computational cost and availability of physical properties. Second, some other phenomenons related to the fluid flow are not considered in this model, such as solid grain

movement in the liquid phase, elemental powders movement in the liquid phase, and the fragmentation of the secondary dendrite arms. The third limitation is the availablity of thermodynamic data. As the Ti-185 alloy is not a popular alloy, some physical properties such as diffusion coefficient can not be got from literature. Fourth, this model can only be used on the two phase solidification now. Additionally, the integration of phase field model with the finite element analysis is a one way coupling, while the influence of microstructure evolution on thermal history is not considered.

3. Non-equilibrium effects: The non-equilibrium effects related to rapid solidification are not considered in this model. Instead, we made an assumption that local equilibrium is maintained during the solidification process. This is reasonable for both the WAAM and the LPBF processes simulated in this thesis since for both the solidification velocity is less than 0.1 m/s. According to Aziz' model [3], a calculation of the influence of this solidification velocity on partition coefficient is less than 1% when $V < 0.1$ m/s. However, as solidification velocities increase to beyond 0.1 m/s, some non-equilibrium effects such as solute trapping and kinetic attachment effects will become evident [4].

6.3 Contribution

This study provides a new phase equilibrium prediction method for the multi-component PF models, and the first benchmark analysis on the application of different models for multi-component alloy solidification. For the application aspect, this model provides a fundamental insight into the process-microstructure-property relations during

LPBF and WAAM of the Ti-185 alloy, which can help industries choose proper processing parameters. The overall contributions of this study to the literature can be concluded as follows:

1. Multi-component phase equilibrium calculation method: the multi-component phase equilibrium calculation is a main time-consuming section of a Multi-component PF model, and this new phase equilibrium calculation method realizes a great combination of computational accuracy and efficiency. It is the application of that method that makes it possible to perform large-scale simulations for the LPBF and WAAM using the multi-component PF model. This method can also be separately applied on other applications, such as constructing the phase diagram.

2. The benchmark analysis: This study presents the first benchmark analysis of various models for solidification in multi-component alloys. Although numerous phase field (PF) models have been developed and applied to the solidification of multi-component alloys, a direct comparison among these models to assess their capabilities and limitations is currently lacking. The primary objective of this benchmark analysis is to establish a reference framework that subsequent researchers can utilize to evaluate and validate their own models. By conducting a comprehensive comparison of the performance and predictive capabilities of different PF models, this study aims to advance the understanding and refinement of solidification modeling in multi-component alloys.

3. The solidification process map: In this study, a comprehensive solidification process map for Ti-185 alloys has been developed. This map encompasses the distinct thermal conditions encountered in both Laser Powder Bed Fusion (LPBF)

and Wire Arc Additive Manufacturing (WAAM) processes. The primary objective of this solidification process map is to facilitate the industrial understanding of the evolution of microstructural morphology under varying thermal conditions. Moreover, the map serves as a valuable tool for guiding the design of optimal AM process parameters to achieve desired microstructural characteristics. By leveraging this solidification process map, industry professionals can make informed decisions regarding the manipulation of thermal conditions and process parameters to attain the desired microstructural attributes in Ti-185 alloy components.

References

[1] B. Echebarria, R. Folch, A. Karma, and M. Plapp, "Quantitative phase-field model of alloy solidification," *Physical review E*, vol. 70, no. 6, p. 061604, 2004.

[2] M. Greenwood, K. Shampur, N. Ofori-Opoku, T. Pinomaa, L. Wang, S. Gurevich, and N. Provatas, "Quantitative 3d phase field modelling of solidification using next-generation adaptive mesh refinement," *Computational Materials Science*, vol. 142, pp. 153–171, 2018.

[3] J. A. Dantzig and M. Rappaz, *Solidification: -Revised & Expanded*. EPFL press, 2016.

[4] S. Kavousi and M. A. Zaeem, "Quantitative phase-field modeling of solute trapping in rapid solidification," *Acta Materialia*, vol. 205, p. 116562, 2021.